Title
Integrated Nanoplasmonic Optical Microfluidics for Label-free Bioassays

Author
Wu, Yir-shyuan

Publication Date
2009

Peer reviewed|Thesis/dissertation

Integrated Nanoplasmonic Optical Microfluidics for Label-free Bioassays

by

Yir-shyuan Wu

A dissertation submitted in partial satisfaction of the

requirements for the degree of

Doctor of Philosophy

in

Applied Science and Technology

in the

Graduate Division

of the

University of California, Berkeley

Committee in charge:

Professor Luke P. Lee, Chair
Professor Ming C. Wu
Professor Steve Conolly

Fall 2009

Integrated Nanoplasmonic Optical Microfluidics for Label-free Bioassays

by Yir-shyuan Wu

Abstract

Integrated Nanoplasmonic Optical Microfluidics for Label-free Bioassays

by

Yir-shyuan Wu

Doctor of Philosophy in Applied Science and Technology

University of California, Berkeley

Professor Luke P. Lee, Chair

Current cellular assays are limited to multi-well based cell culture samples, and the existing cellular protein detection methods are restricted to labeling the targeting molecules with fluorescent dyes or other reporters. Microfluidic cell culture technology can provide precise and physiologically relevant microenvironment control to improve the quality of cell based assays. Nanoplasmonic optical probes enable the label-free detection of cellular protein with high temporal and spatial resolution. The goal of this dissertation is to develop and integrate real-time label-free nanoplasmonic detection with high-throughput microfluidic cell culture platforms.

In this dissertation, several novel nanoplasmonic geometries, such as crescent-shaped nanoholes and nanocorals are developed to provide sensitive, robust and low-cost solutions for biomolecular detection. The sharp tips and large curvature features on the nanostructures are designed to maximize the sensitivity of both localized surface plasmon resonance (LSPR) peak shift and surface enhanced Raman spectroscopy (SERS) sensing applications. Two robust cell culture platforms - long-term single cell culture arrays and self-assembled tumor spheroid arrays - that facilitate monitoring arrayed cells with precise micro-environment control are also demonstrated.

The integration of nanoplasmonic biosensors and microfluidic cell culture platforms are demonstrated on both chip-size and at the whole 4” wafer scale. Such integrated systems provide high resolution dynamic information on large array of precisely controlled cell populations. We expect this new tool will have significant impact on both fundamental cellular research and new drug evaluation.

Dedicated to my parents:

Mr. Chin-shun Wu and Mrs. Kuo-pao Wu Lai

&

my loving family:

Linus, Mimi and Adrian

Table of Contents

Acknowledgements

I would like to express my deepest gratitude to my adviser, Dr. Luke P. Lee, for his invaluable advice and the greatest learning experience at the BioPOETS research group. His insistence in sound scientific methods has given me the best guideline for the research.

In addition, I would like to thank Prof. Ming C. Wu, Prof. Steve Conolly, Prof. Dorian Liepmann and Prof. Nathan Cheung being my dissertation, qualification exam, and preliminary exam committee. Their advice helped me pass each important step of my graduate student career. I also want to thank Ms. Patricia Berumen in AS&T department, for her kindest help and care.

I deeply appreciate my parents, who always love and support me, no matter how far I'm away from them. Moreover, many gracious thanks to my husband, Linus, for his supportive company and help with my work; and to my two lovely kids, Mimi and Adrian, for giving me the strength and energy to complete my doctoral research. To my brother Jeff and my sister Kelly, thank you for always being there and cheering me up when I am stressed out. To my best friend, Somin Eunice Lee, thank you for sharing this journey with me and your sincere help on my research. To my best research partner, Ben Ross, who is the smartest person I've ever met, and I really enjoy the time working with him. To Rick Henrikson, thank you for always giving me a hand whenever I most need help.

Thanks to all of the best labmates in BioPOETS: David Breslauer, Hansang Cho, Yolanda Zhang, Mimi Zhang, Yeonho Choi, SoonGweon Hong, Eric Lee, Megan Dueck, YoungGeun Park, Debkishore Mitra, Frankie Myers, John Waldeisen and Brendan Turner, it is so nice to work with so many brilliant researchers. To Dino Di Carlo, thank you for mentoring me when I first entered the lab. To Tanner Nevill and Michelle Khine, thank you for taking care of me and encouraging me as an elder brother and an elder sister, although both of you are younger than me. To Helen Wu, thanks for your help with my research and giving me the chance to learn how to be a mentor.

My deepest gratitude also goes to our family friends in Berkeley. Don, Mary, Shelly and Hsin, thank you for the warm friendship. The life in UC village becomes so colorful because of you.

Finally, I would like to gratefully acknowledge the financial support of the Taiwan Merit Scholarship, TMS-094-2-A-008. The four-year support allowed me to concentrate on my research and successfully finish my doctoral degree.

CHAPTER 1: INTRODUCTION

1.1 Introduction to microfluidic label-free cellular bioassays – moving toward better spatial and temporal resolution

The cell is the basic unit of life that makes up complex living organism systems. At the cellular level, the microenvironment plays an important role in determining a cell's behavior and growth patterns. On the other hand, a cell's behavior in response to input stimuli can reflect the basic response of the organism. Thus, the cell-based bioassay is an important analytical technique in fundamental biology research, disease diagnosis, and advanced drug and theraputic development.

The current methods for cellular assay rely on multi-well based cell culture samples. Since real physiological conditions of cell culture requires dynamic controls, it is critical to challenge traditional multi-well based static culturing methods, which cannot control physiologically relevant flow, cell-cell contacts, cellular packing density, 3D ECM,…etc. Microfluidic technology is a strong candidate for providing precise and physiologically relevant microenviroments for cell culture, thus improving the quality of cell based assays. The small scale allows proper positioning and manipulation of cells and the microfluidic components can be easily arrayed for development into a high-throughput assay.

Common cell assays include live/dead, adhesion, morphology, mobility, and DNA and protein analysis. While the first four assays assess the overall response of a cell to a drug or other stimulus, the last two focus on detailing the genomic and proteomic activities specific to various cell functions and signaling pathways. For proteins, the "work horses" that perform most of the intracellular tasks, it is very important to be able to detect and quantify specific proteins or further verify their sub-cellular distributions after specific inputs in order to understand the cell's working system. Resolving the proteomic system can help us to not only better understand living systems, but also to improve on the design and application of new drugs for these systems. To detect the presence of specific proteins within the living cells, the most direct method is to label them with "reporters", such as fluorescent molecules. The "labeling process" itself impedes the temporal resolution of the detection, since the measurement is usually "pinned" at the moment of labeling and the cell system is interrupted abruptly once the label is attached to the targeted protein. In most cases, cells must be fixed prior to permeabilizing the cell membrane in order to label intracellular proteins, thus limiting the possibility to trace single living cells and recording their time-lapsed proteomic information. Label-free protein detection methods are the key to improving the temporal resolution and will be discussed later in detail.

Quantification of one specific protein requires that the protein first be isolated or selected for from among the 10,000 different ones present in a cell. Electrophoresis and chromatography are techniques commonly used for separating proteins from a biological sample in conditioned cell culture media or after cell lysis.[1] A more efficient method to fish one protein from the mixture is by using highly specific antibody assays, such as ELISA[2] and Western blotting[3]. To report the presence of the antigen, the antibodies are usually conjugated with fluorescent markers or enzymes that work on chromogenic substrates. These technologies still have some drawbacks, however. Most importantly, they represent a bulk measurement, the average amount of protein

in millions of cells, so it is hard to go down to the single cell resolution. There is no possibility for real-time measurement, and only end-point detection is conducted, while the time-lapse information about dynamic protein level is valuable for understanding function and how those cellular proteins are involved in signal pathways.

There is always demand for improving the content and quality of cellular protein detection. From quantifying the protein content of a large number of cells, researchers have moved on to ask further questions: What is the amount of protein produced in each cell among the population? What are the sub-cellular locations of these proteins where they perform their tasks? How fast does the protein expression level change under certain stimuli and how does the change trigger series of activities in the cells, including cell death or other biochemical reactions? Techniques to improve spatial and temporal resolution are continually being developed to help to gain a deeper understanding of the cellular workings.

Figure 1.1 lists the technologies capable of protein detection and quantification with regard to their relative spatial and temporal resolutions. Immuno-fluorescence staining is a well-developed technology to visualize the sub-cellular distribution of biomolecules of interest. It provides fine spatial resolution but is limited to the end-point detection. When separating these immuno-fluorescently-labeled cells by flow cytometry, the distribution of the protein content in the cells can be plotted. Again this is an end-point assay and can only capture the protein composition distribution of the cells at one time point. To overcome the limitation of temporal resolution of immunoassays, several methods have been developed – for example, immunoassay methods based on homogenous time-resolved fluorescence (HTRF)[4] technology using Fluorescent Resonance Energy Transfer (FRET) to report protein level in the cell culture media. Recently, many research efforts have been made to realize a small spatial and temporal resolution for cellular protein detection. Analogs consist of auto-fluorescent proteins (green fluorescent protein (GFP) in most of the cases) that are produced genetically within the cells of interest is a powerful tool to capture temporal and spatial dynamics of protein expression[5], but the whole process including gene transfection is complicated and might bias the cell from its original behavior. The microelectrode[6] is another approach used to detect the change of biomolecular composition near the cell surface but the technology is limited in the electrostatic molecules and it is difficult to probe the events inside the cells.

The current research efforts are aimed at addressing the capability gap of cell assays with high spatial and temporal resolution at the bottom left corner of Figure 1.1. A cell assay platform with precise microenvironment control by microfluidics and label-free real-time protein detection is potential to realize the goal of dynamic protein quantification at sub-cellular resolution.

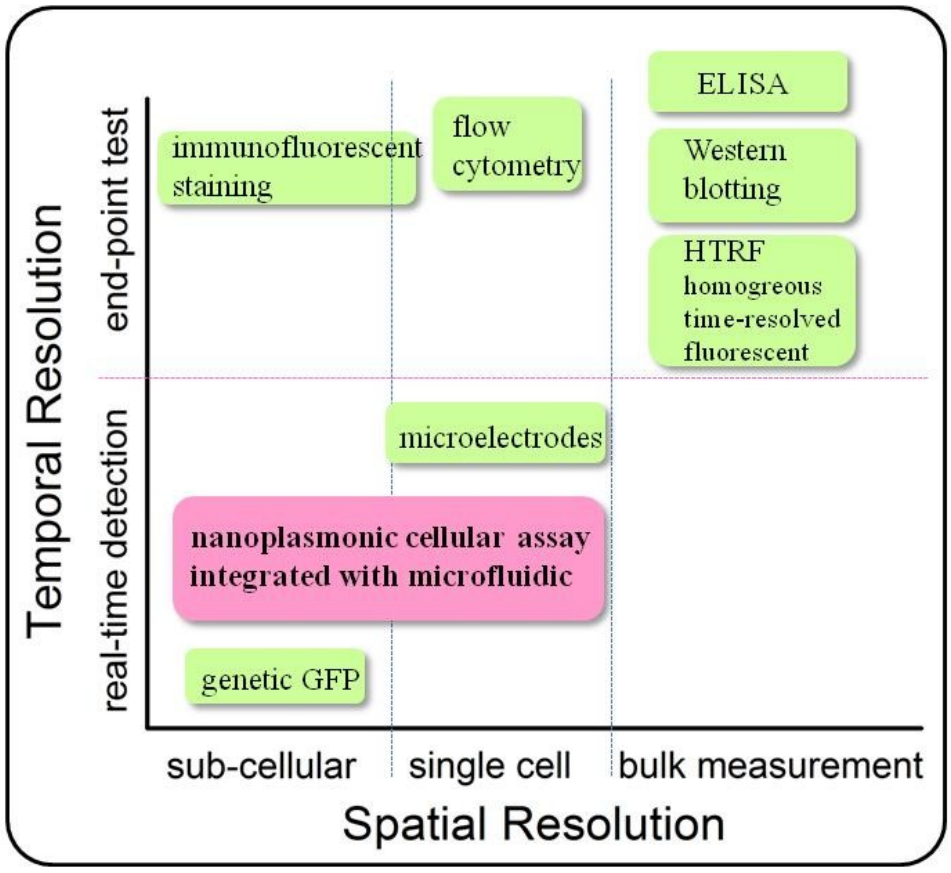

Figure 1.1: Different technologies for cellular protein detection with respect to their spatial and temporal resolution of data quality. A cell assay platform with precise microenvironment control by microfluidics and label-free protein detection by nanoplasmonic sensors can realize the goal of dynamic protein quantification at sub-cellular resolution.

There are several ways to realize the label-free detection of protein in a living cell. One is to read out the intrinsic signals from the protein of interest such as absorption spectrum or Raman scattering signal, but these optical measurements have limited spatial resolution and weak signal intensity. An approach by inserting fiber optic nanosensors into the living cell is reported to address the spatial resolution problem[7]. There is a new approach of sending the nanoparticles or other nanoprobes into the cells to help enhance the optical signal coming from the cellular proteins. The spatial resolution is also enhanced in this case since only the protein in proximity of the nanoprobes are detected, and therefore, the local biochemical composition within the effective length (or electric field decay length, around tens of nanometer, depends on geometry and material of nanoparticles) of the nanoprobes is reported. This is one example of how nanoplasmonic materials can help to realize the goal of label-free real-time protein detection within a living cell.[8-9]

Another strategy of label-free cellular detection is to record the signal change of the probes while the concentration of the protein surrounding the probes changes or when binding of the protein of interest to the surfaces of the probes happens. Microelectrodes can be used to probe

the composition change close to the cell surface, and the recently developed nanowire biosensor is designed to measure the protein binding event by looking at the current change resulting binding. However, these two methods are limited to molecular detection outside the cells. Nanoplasmonic LSPR sensor is a strong candidate for intracellular protein detection. After sending noble metal nanoparticles into a living cell, intracellular proteins are able to bind to the surface of the nanoparticle, and the scattering peak of the nanoparticle changes in proportional to the amount of binding events. The local protein concentration can be reported in real time by noninvasive optical measurement.

For these label-free protein detection systems such as nanoplasmonic based sensing, the time resolution is decided by the readout speed of the measurement. No further washing or renewing steps are needed in between adjacent measurement. And this, combined with the increased signal strength, could be a major advance towards the goal of the real-time monitoring of the living systems.

The goal of this dissertation is to develop the key elements for the label-free nanoplasmonic based protein detection in the well-controlled microfluidic cell culture system. Nanoplasmonic probes pave the way for protein detection at high spatial and temporal resolution, and microfluidic systems facilitates the precise control of physiological cell culture and dose conditions.

Technique	**Throughput**	**Dynamic Analysis**	**Spatial resolution**	**Invasive**	**Microfluidic integration**	**Reported sensitivity**
Fiber optics nanosensor	Low	Yes	Subcellular	Yes	Hard	
Microelectrodes	Low	Yes	Subcellular	No	Hard	
LSPR sensors	High	Yes	Subcellular	No	Easy	~10 pM[10]
SERS probes	High	Yes	Subcellular	No	Easy	~100 fM[11]

Table 1.1: List of label-free real-time detection methods for a living cell

1.2 Nanoplasmonics for real-time cellular protein detection

In this dissertation, two plasmonic spectroscopies from nanoplasmonic materials for real-time cellular protein detection are discussed: localized surface plasmon resonance (LSPR) peak shift and surface enhanced Raman spectroscopy (SERS) from noble metal nanostructures. Metal nanostructures are important building blocks of the next generation of biochemical sensing devices. Upon light incidence, non-propagating excitation of conduction electrons of a metallic nanostructure couple to the electromagnetic field, with the EM resonance occuring at a specific wavelength, called the localized surface plasmon resonance (LSPR). The peak position of LSPR depends on the surrounding dielectric environment of the nanostructures and thus will shift after molecules bind to the surface of the nanostructure. By measuring the LSPR peak change, the metal nanostructures serve as individual sensors. Upon the LSPR, the local electric field near the surface of each nanostructure is highly enhanced, and results in the surface-enhanced spectroscopic technologies such as SERS.

The size of cells is usually tens of micrometers. Nanoprobes ranging from tens to hundreds nanometers in diameter are suitable to be sent into the cells for detection of intracellular proteins or arrayed outsides the cells as high resolution pixels for secretory protein detection (see the illustration in Figure 1.2). These two measurement modes will be discussed separately with a summary of recent research efforts.

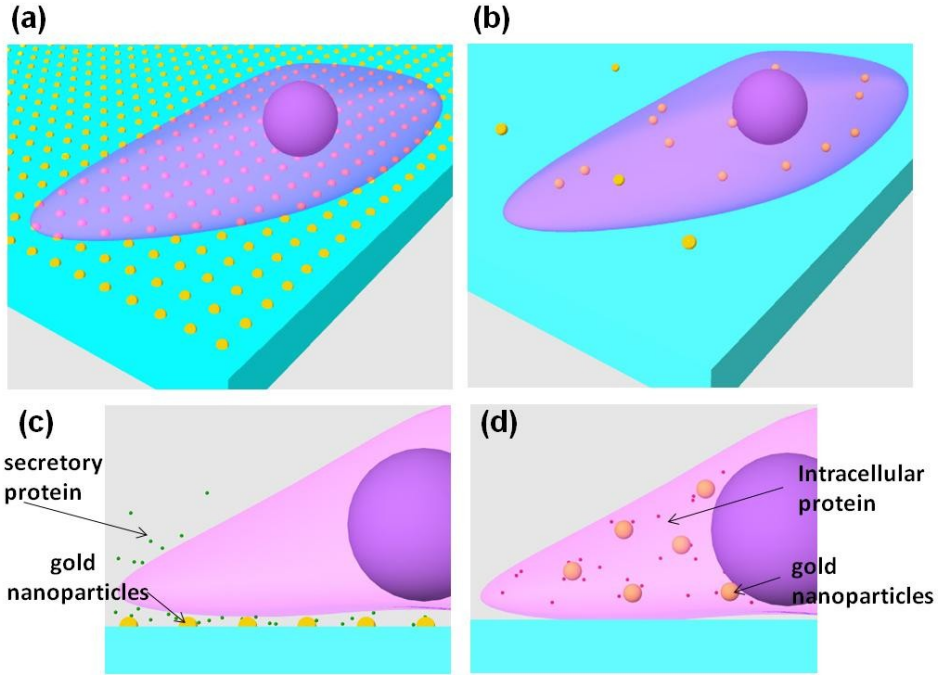

Figure 1.2: Nanoplamonic probes for protein detection (a) outside the cell by arrayed gold nanoparticles patterned on the substrates and (b) inside the cell with gold nanoparticles locating inside the cell.

1.2.1 Detection of secretory proteins outside the cell

Cellular secretions are a key method by which cells influence the regulation and control of its activities. Many cells secrete proteins into their surroundings for various purposes, such as enzymes for digestion, antibodies for defense and collagen for structure strengthening.[12] A large amount of important cell-cell communication occurs through the release of specific biochemical or chemical messengers by an emitting cell, generally coupled with a specific detection of these messengers by the receiving cell that triggers specific bioactivities.[13] Over- or under-expression of these secretory proteins usually causes a break-down in the system equilibrium and results in disease. Thus, the quantification or detection of proteins released from cells is a crucial step toward understanding the fundamental roles that cell secretion plays in certain pathways of physiological signaling systems.

Detection of cell secretion is also important in the clinical diagnostic and drug industries. Since the proteins are released from the cells and are thus able to be detected in the blood, urine, or saliva, they become important disease markers for medical diagnostics. The changes in concentration of some secretory proteins in human sera are correlated with the pathology: for example, prostasin with ovarian cancer, insulin with diabetes, and amyloid beta ($A\beta$) with Alzheimer's disease. Much effort is being placed on developing technologies that are focused on the sensitive and low-cost detection of these secretory proteins from patients' serum samples. On the other hand, for drug candidates that are designed to inhibit or increase cell secretion levels to treat secretion-related diseases, the quantity of the secretion after administering the dose is the standard indicator used to evaluate the performance of the drugs. Researchers have monitored vascular endothelia growth factor (VEGF)[14] and matrix metalloproteinases (MMPs)[15] to evaluate the efficacy of anticancer drugs, C1q proteins for anti-imflammatory drugs[16] and $A\beta$ for Alzheimer's disease treatments.[17]

If we zoom in on the cells being cultured, whatever the purpose for their secretions, an infinitesimal number of molecules are released during a short time (on the order of milliseconds) by a living cell into the extracellular region. Such an infinitely small amount of secretion molecules results in local concentrations high enough for the receptors to detect but that are soon diluted by the diffusion, thus the quantification of secretory proteins remains a challenge as it is unaddressed by the actual analytical standards. Petri dish or multi-well cell-based secretion assays usually are processed for a long time to wait until there are measurable amount of the proteins accumulated within the conditioned media. Only one data point is obtained during a 3-4 day assay, and a correlation between cell proliferation and deformation cannot be achieved. The strategy to overcome the problem of realizing real-time detection is to put the biosensors close to the cells to measure the local concentration resulting from the release events while recording the cell behavior at the same time. Moreover, for the real-time detection of the secretion activities, we need technologies that can be repeated continuously within the measurement duration with a minimal effect on cells' behavior.

Metal nanoplasmonic biosensors are capable of real-time and noninvasive protein secretion detection, but most of the technologies thar have been reported are focused on in-vitro testing with patients' urine or serum samples. Haes et al. have reported an LSPR biosensor from amyloid beta oligomer by using a nanosphere lithography fabricated silver prism array.[10] Beier et al. used a nanoshell array as the substrate for SERS detection of amyloid beta but in this report they apply congo red as the SERS label since SERS signals directly from $A\beta$ are too weak in this set up[18]. Many nanostructured substrates have demonstrated their biosensing potential by

measuring the performance upon biotin streptavidin binding. This is a developing field and as we know, there has been no research reported that directly measures the secretory protein by culturing the cells on top of the nanoplasmonic sensors The key elements developed in this thesis such as the new nanostructure array reported in Chapter 3 and the nanoplasmonic and microfluidic integration technology reported in Chapter 7 can help reach this goal.

1.2.2 Detection of intra-cellular proteins

The central dogma of the cell has long been an important research focus in cell biology. Information on how cells respond to environmental stimuli and produce functional proteins via gene expression is especially important for both fundamental research and pharmaceutical applications. There are a great number of research efforts that incorporate nanoplasmonic materials designed to enter the cells and perform different tasks, such as detection, drug releasing and localized heating. Uptake efficiency for different sizes and shapes of nanoparticles has also been well-investigated.[19] However, reports regarding dynamic intracellular protein sensing are very limited.

Intracellular SERS detection is relatively well-developed among the nanoplasmic technologies that demonstrate potential for dynamic protein detection. The intracellular SERS reported so far was demonstrated by the aggregated noble metal colloidal nanoparticles with unpredictable enhancement factors, thus limiting the quantification of cellular biomolecules in interest.[7-9] The stand-alone SERS nanoprobe with designed intraparticle hot-spots is a way for improving the signal repeatability,[20-21] but in-vivo sensing by these proposed tools hasn't been demonstrated. An interesting approach to nanoplasmonic-based in-vivo sensing, named plasmon resonance energy transfer (PRET), has been developed in our group, and in-vivo detection of cytochrom c in HepG2 cells has been reported.[22]

Despite recent advances, nanoplasmonic in-vivo sensing technology is still in its infancy, and many efforts have been put into the design and fabrication of multifunctional nanoprobes to perform multiple tasks after entering the cells. We have developed a multifunctional nanocoral probe to specifically target to the cancer receptor and can perform SERS once receptor mediated endocytosis, enhancing the process for the nanoprobe entery and quantification. The concept of decoupled targeting and sensing function on a stand-alone nanoprobe is important for future intracellular imaging. I will report the technology in Chapter 4.

1.3 Optimize the cell assay microenvironment by microfulidic

Mammalian cell culture is an important tool used in both the lab and the drug industry for many applications from screening novel drugs to industrial production of proteins such as vaccines. The progress of microfluidic technologies makes "cell culture on a chip" a thriving research field. Microfluidics breakthroughs have provided a number of advancements in analyzing living cells, including cell trapping and sorting, high-throughput assays, and micro-scale reagent and culture medium manipulation. The principles of microfluidics can be used to generate microscale physiological conditions for dynamic cell culture, the most important aspect for culturing stem cells, which requires precise controls of transcription factors, growth factors, sheer stress, etc. For cell-based protein detection, microfluidic technology is a strong candidate for generating a favorable infrastructure for the cell samples being monitored since the precise microenvironmental control and cell handling offered by a microfluidic system is ideal

Our lab has developed hydrodymanic cell trapping technology that allows controlled cell loading in arrayed locations, after which the cells are cultured under physiological perfusion.[23] The positioned cells can then be dosed with a stimulus of interest using the perfusion system. In this way, large amounts of quantitative data can be procured in parallel from each cell sample in the array. By properly designing the geometry of the traps, I demonstrated long-term culture of single cell arrays and tumor spheroid arrays as shown in Figure 1.3. Both microfluidic systems are ideal for traditional cell monitoring and drug evaluation, and moreover, they can easily be integrated with nanoplasmonic substrates by bonding the cell culture device onto the substrate with nanoplasmonic probes as illustrated in Figure 1.3. The arrayed metal nanoparticle biosensors can be patterned close to the cell culture area or overlapping with the cell culture area. The whole device is then easily monitored under a microscope and the real-time cell images and plasmonic biosening information can be simultaneously read out.

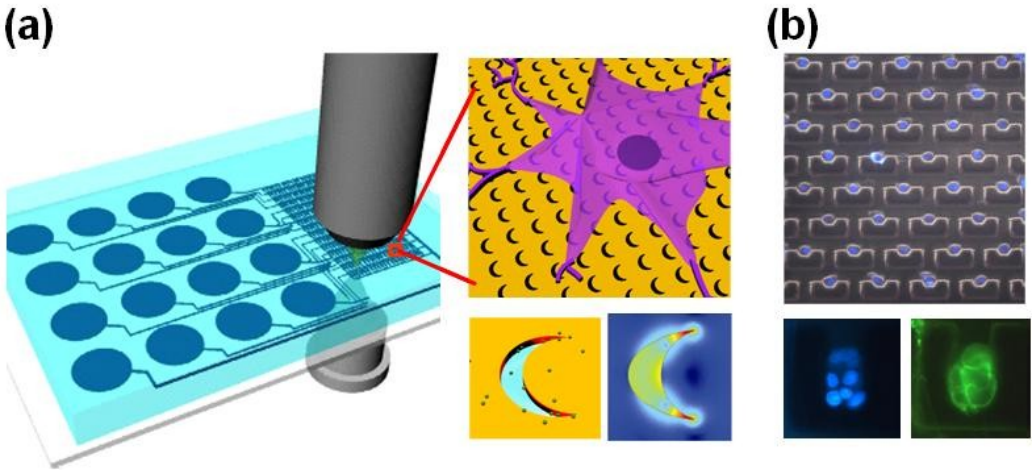

Figure 1.3 Microfluidic system for cell-secretion detection. The cells were cultured in the arrayed cell cultured chamber equipped with a perfusion system for programmable doe profile. At the bottom of the cell culture chamber, arrayed gold nanostructurea serve as the sensor of the secretion protein. The whole device is easily monitored under a microscope and the cell images and the plasmonic biosening information can be simultaneously read out.

1.4 Outline of the work -- Integrated nanoplasmonic system for label-free cellular assay

The overall goal of this dissertation is to develop and integrate real-time label-free nanoplasmonic detection with high-throughput microfluidic cell culture platforms. A number of recent efforts have been made to optimize nanoplasmonic structures in order to maximize signal enhancement. I have proposed several novel nanoplasmonic geometries that provide sensitive, robust and low-cost solutions. Furthermore, I have developed robust cell culture platforms that facilitate monitoring arrayed cells with precise micro-environment control. Beyond traditional cell monitoring, this analytical tool readily lends itself to integration with nanoplasmonic substrates. Such integrated platforms provide high resolution dynamic information on large array of precisely controlled cell populations.

Chapter 2 provides a general overview of nanoplasmonic biosensing, focusing on arrayed nanostructures substrates. The chapter then discusses microfluidic designs for cell culture particularly suitable for real-time protein monitoring. Chapter 3 presents a new nanoplasmonic structure: crescent-shaped nanoholes that are capable of both LSPR and SERS biosensing. Chapter 4 describes a new plasmonic nanosensor that can both be used as a uniform SERS substrate and stand-alone nanoprobe for target and sensing of a living cell. Chapter 5 presents the microfluidic platform for single cell culture and assay. Chapter 6 describes a microfluidic platform for arrayed cancer spheroid culture. The design of nanoplasmonics described in Chapters 3 and 4 and microfluidics in Chapters 5 and 6 can all be integrated for the real-time cell detection system. In Chapter7, we demonstrate this integration with some example devices including a wafer scale integration system and discuss the outlook of integrated nanoplasmonic and microfluidic cellular assay system. Chapter 8 presents the conclusions of these efforts.

References:

(1) Campbell, N. A.; Reece, J. B. *Biology* 6 th edition
(2) Engvall, E.; Perlman, P. *Immunochemistry* **1971**, 8, 871–874.
(3) Burnette, W. N. *Analytical Biochemistry* **1981**, 112, 195–203.
(4) Kolb, A. J.; Kaplita, P. V.; Hayes, D. J.; Park, Y. W. *Drug Discovery Today*, **1998**, 7, 333-342.
(5) Kain, S.; Ganguly, S. *Current Protocols in Molecular Biology*, **1995**, 9.6.1- 9.6.12.
(6) Ammann, D.; Lanter F; Steiner, R. A.; Schulthess, P.; Shijo, Y.; Simon W. *Anal. Chem*., **1981**, 53, 2267–2269
(7)Vo-Dinh, T; Kasili, P.; Wabuyele, M.; *Nanomedicine* **2006**,2, 22-30
(8) Nie, S. M.; Emory, S. R. *Science* **1997**, 275, 1102.
(9) Kneipp, K.; Wang, Y.; Kneipp, H.; Perelman, L. T.; Itzkan, I.; Dasari, R. R., Feld, M. S. *Phys. Rev. Lett.* **1997**, 78, 1667.
(10) Haes, A. J.; Chang, L.; Klein, W. L.; Van Duyne R. P. *J. Am. Chem. Soc*, **2005**, 127, 2264-2271
(11) Liu,G.; Lee, L. P. *Appl. Phys. Lett.* **2005**, 87, 074101-1-3
(12) Lodish, H.; Berk, A.; Matsudaira, P.; Kaiser, C. A.; Krieger, M.; Scott M. P.; Zipursky, S. L.; Darnell J. *Molecular Cell biology* 5th edition.‘
(13) Burgoyne, R. D.; Morgan, A. *Physiological Reviews* **2003**, 83,581-632
(14) Komorowski, J.; Jerczynska, H.; Siejka, A.; Baranska, P.; Lawnicka, H.; Pawlowska, Z.; Stepien, H. *Life Sciences* **2006**, 78, 2558 – 2563.
(15) Cheng, Y. Y.; Huang, L.; Lee, K. M.; Li, K., Kumta, S. M. *Pediatr Blood Cancer* **2004**, 42, 410–415.
(16) Faust, D.; Akoglu, B.; Zgouras, D.; Scheuermann, E. H.; Milovic, V; Stein, J *Biochemical Pharmacology* **2002,** 64, 457-462.
(17) Albrecht, H.; Zbinden, P.; Rizzi, A.; Villetti, G.; Riccardi, B.; Puccini, P.; Catinella, S.; Imbimbo, B. P. *Combinatorial Chemistry & High Throughput Screening* **2004**, 7, 745-756.
(18) Beier, H. T.; Cowan, C. B.; Chou, I. H.; Pallikal, J.; Henry, J. E.; Benford1, M. E.; Jackson, J. B.; Good, T. A.; Coté, G. L. *Plasmonics*, **2007**, 2, 55-64.
(19) Zhang, S.; Li, J.; Lykotrafitis, G.; Bao, G.; Suresh, S. *Adv. Mater.* **2009**, 21, 419–424
(20) Jackson, J. B.; Westcott, S. L.; Hirsch, L. R.; West, J. L.; Halas, N. J. *Appl. Phys. Lett.* **2003**, 82 , 257–259.
(21) Liu.G.; Kim, J.; Mejia, Y. X.; Lee, L. P. *Nano Lett.* **2005**, 5, 119.
(22) Choi, Y.; Kang, T.; Lee, L. P. *Nano Lett*., **2009**, 9, 85–90
(23) Hung, P. J; Lee, P.; Lee, L. P. *Lab Chip*, **2005**, 5, 44 - 48

CHAPTER 2:
BACKGROUND:NANOPLASMONIC BIOSENSING AND MICROFLUIDIC CELL CULTURE

2.1 Surface Plasmon Resonance (SPR), LSPR , SERS, and PRET

Over a wide frequency range, the interaction of metal with incident electromagnetic waves can be analyzed by Maxwell equations and the Drude model. Applying Maxwell's equations to the flat interface between a metal and a dielectric material upon light incidence, the solution is an electromagnetic excitation propagating at the interface confined in the perpendicular direction evanescently and named a surface plasmon polariton (SPP). The dispersion relation of SPP propagating at the interface can be expressed as

$$k = k_0 \sqrt{\frac{\varepsilon_d \varepsilon_m}{\varepsilon_d + \varepsilon_m}} \quad \text{.....(2.1)}$$

Where k and k_0 are the propagation constant of the SPP traveling wave and light, and ε_d, ε_m are dielectric constant of dielectric and metal. The surface plasmon resonance occurs when the denominator in equation (2.1) goes to zero, and therefore, the condition of SPR is very sensitive to the change of the dielectric constant (ε_d) resulting from the surface binding events. To match the momentum of incident light and SPP, a prism or a grating is usually integrated with the metal film and this is the bottleneck of miniaturization of the whole measurement system. The most commonly used coupling method from light to SPP, Kretschmann configuration, is illustrated in Figure 2.1.

Unlike SPR, which propagates along the interface between metal and dielectric, localized surface plasmons (LSP) are non-propagating excitations of conduction electrons in nanometer-scaled metal structures. Begin with the simplest nanostructure, a metal nanosphere; when the wavelength of the incident light is much larger than the diameter of the nanosphere, we can apply a quasi-static approximation. Now the question is as simple as solving the Laplace equation for a metal particle located in a constant electric field. The dipole moment p of the nanosphere with radius a induced by the electric field E is described as:

$$p = 4\pi\varepsilon_0\varepsilon_d a^3 \frac{\varepsilon_m(\omega) - \varepsilon_d}{\varepsilon_m(\omega) + 2\varepsilon_d} E = \varepsilon_0\varepsilon_d \alpha E \quad \text{.....(2.2)}$$

$$\alpha = 4\pi a^3 \frac{\varepsilon_m(\omega) - \varepsilon_d}{\varepsilon_m(\omega) + 2\varepsilon_d} \quad \text{.....(2.3)}$$

ε_d, ε_m are dielectric constant of surrounding dielectric media and metal nanoparticle, and α is defined as polarizability of the nanoparticle. When we add back the time harmonic term of the electric field $E(t)=Ee^{i\omega t}$, the induced dipole p acts as an oscillating dipole $p(t)=pe^{i\omega t}$. The

resulting scattering and absorption cross-section derived from this oscillating dipole can be written as:

$$C_{scat} = \frac{k^4}{6\pi}|\alpha|^2 = \frac{8\pi}{3}k^4 a^6 \left|\frac{\varepsilon_m(\omega)-\varepsilon_d}{\varepsilon_m(\omega)+2\varepsilon_d}\right|^2 \quad \text{.....(2.4)}$$

$$C_{abs} = k\,\mathrm{Im}[\alpha] = 4\pi k a^3\,\mathrm{Im}\left[\frac{\varepsilon_m(\omega)-\varepsilon_d}{\varepsilon_m(\omega)+2\varepsilon_d}\right] \quad \text{..... .....(2.5)}$$

Similar to SPR, the resonance happens at the point when the denominator in equation (2.4) and (2.5) goes to zero, and thus the resonance peak is sensitive to the change of ambient dielectric constant resulting from molecular binding events. Different from SPR based measurement, the localized surface plasmon resonance (LSPR) happens directly upon the incidence of light at the resonance frequency: no momentum matching between incident light and LSP is needed. The nanoplasmonic materials are thus ideal for the application of stand-alone nanosensors for intracellular imaging or integration with micro/nanofluidic systems.

For LSPR sensing, the position change of the resonance peak, due to the ambient refractive index change resulting from the binding of a molecule of interest, is the reporter of the measurement. To maximize the detection sensitivity, we need to optimize the geometric parameters such as shape and size of the nanostructure. By repeating the steps from equation (2.1)~(2.5), replacing the spherical nanostructure with an ellipsoidal nanostructure with axis a_1, a_2, a_3, and solving the Laplace equation again with constant electric field, E, under quasi-static approximation, the scattering for ellipsoidal cross-section is described as:

$$C_{scat} = \frac{k^4}{6\pi}|\alpha_i|^4 \quad \text{.....(2.6)}$$

$$\alpha_i = 4\pi a_1 a_2 a_3 \frac{\varepsilon_p - \varepsilon_m}{3\varepsilon_m + 3L_i(\varepsilon_p - \varepsilon_m)} \quad \text{.....(2.7)}$$

$$L_i = \frac{a_1 a_2 a_3}{2}\int_0^\infty \frac{dq}{\left(a_i^2+q\right)\sqrt{\left(a_1^2+q\right)\cdot\left(a_2^2+q\right)\cdot\left(a_3^2+q\right)}} \quad \text{.....(2.8)}$$

in which L_i is the geometric factor that related to the aspect ratio of the shape of the particles.[1] From equation (2.6)~(2.8), we know that the nanostructure with high aspect ratio have more LSPR peak shift upon the change of dielectric constant of the surrounding media. Since we can use ellipsoids to approximate the shape of whole or part of the arbitrary-shaped nanostructure, we know that the design of nanoparticles with high aspect ratio, sharp tips and large curvature can help to enhance the LSPR shift sensitivity.

When using LSPR for detection of binding molecules, the amount of the peak shift $\Delta\lambda_{max}$ can be described as the following equation (2.9).

$$\Delta\lambda_{\max} = m\Delta n\left(1-e^{-2d/l_d}\right) \quad \text{.....(2.9)}$$

where m is the refractive index sensitivity that is related to the shape and the material as we described in equation (2.6)~(2.8) and Δn is the change of ambient refractive index. The effective

adsorbate layer thickness, d, is fixed by the concentration of the adsorbate under detection. The decay length l_d is related to the material and the shape of the nanoparticles: the sharp tips or the high curvature structure that can generate higher local electric fields usually have smaller field-decay length.[2] At the single nanoparticle point of view, we hope to increase the aspect ratio and create the inter-particle hot spots and sharp tips to get higher peak shift sensitivity (higher m and smaller l_d).

Under the localized surface plasmon resonance condition, the local electric field is highly enhanced near the surface of the nanostructure, and it results in the amplification of Raman scattering signal from the molecules close to the surface of nanostructure. Raman scattering is based on the fact that molecular vibrations have characteristic frequencies in the infrared spectral region. When light is scattered from the molecule, some photons will transfer their energy to the molecules' vibration and result in lower frequency than the incident light. Plotting the spectrum of this scattered light yields a unique molecular fingerprint. However, Raman is a very weak process, with molecular cross-sections in the 10^{-29} –10^{-32} cm^2 range. When the molecule under detection is in close proximity of the noble metal nanoparticles, the enhanced field due to the localized surface resonance can enhance the Raman Scattering signal S_{Raman} as described in the following equation:

$$S_{Raman} = N\sigma\left|A(\nu_L)\right|^2\left|A(\nu_S)\right|^2 I(\nu_L) \quad \text{.....(2.10)}$$

where $A(\nu_L)$ and $A(\nu_S)$ represent the enhancement factors for an excitation light source of intensity $I(\nu_L)$ and Raman scattering fields, σ is the increased Raman cross-section of the molecule in contact with the nanostructure, and N is the number of molecules in surface enhanced Raman spectroscopy (SERS) process.[3] To maximize the SERS signal, we need to design nanostructures in a way such that they can have strong resonance to result in high electric field at the excitation wavelength or Raman signal wavelength. The sharp tips or the high curvature structures are the design goal for high SERS signal enhancement. The high field at the sharp tips can be explained by lightening rod effects: when we approximate the tip with ellipsoid with long axis a and short axis b, the electric field can be described as[4]:

$$E_{tip} = \frac{(1-A)(\varepsilon-1)}{1+(\varepsilon-1)A}E_0 + E_0 \quad \text{.....(2.11)}$$

where

$$A \approx \left(\frac{b}{a}\right)^2 \ln\left(\frac{b}{a}\right) \quad \text{.....(2.12)}$$

The nanogaps between two high curvature structures especially generate strong field by the electromagnetic field coupling effect and are usually called "hot spots" in SERS set ups. The high field at the nanogap can be explained by the capacitor effect.[5] The induced charge on two closely located metal surfaces is:

$$Q_{ind} = \int_Z \sigma_s dA = \frac{1}{iw}\int_{\partial Z} \tilde{K}_{eff} \cdot \hat{n} dl \quad \text{.....(2.13)}$$

$$E_{ind} = \frac{Q_{ind}}{aC_{\lambda}} \quad \text{.....(2.14)}$$

Q_{ind} and E_{ind} are induced charge and electric field respectively. Design and fabrication of the nanostructure carrying interparticle or intraparticle nanogaps is one of the directions of optimizing the SERS performance of nanoplasmonic substrates.

LSPR peak shift and SERS from nanostructures have potential for intracellular imaging and micro/nanofluidic integration. A great amount of research efforts have been put on engineering new nanostructures to enhance the sensitivity of chemical sensing, and the physics of LSPR and SERS also has been more deeply investigated at the same time.

These is a novel plasmonic spectroscopic technology latest developed named plasmonic resonance energy transfer (PRET).[6] Similar to LSPR peak shift measurement, the scattering light from the nanoparticle is collected. However, the molecular detection mechanism is very different. The plasmon quenching dips in the spectrum of LSPR scattering light were observed when the biomolecules conjugated on gold nanopaticles have electron transition energy overlapped with LSPR spectrum of gold nanoparticles. One example demonstrated by Liu et al. is the PRET of reduced cytochrom c molecule that has two optical absorption peaks at 525 nm and 550 nm. When reduced cytochrome c molecules were conjugated to a 30 nm gold nanoparticle that has a LSPR spectrum which covers 457nm ~ 650nm wavelength, two clear dips at 525 nm and 550 nm are clearly observed in the LSPR spectrum of the gold nanoparticle, and the occurence of the dips is explained by energy transfer between the LSPR of the gold nanoparticle to the electron excitation of cytochrome c molecules through dipole-dipole interaction. Similar to the SERS measurement, the read-out signal of PRET is intrinsic to molecules in proximity to or in contact with the nanoprobe surface, and this molecular fingerprint offers the potential for label-free multi-channel read out of local biochemical composition

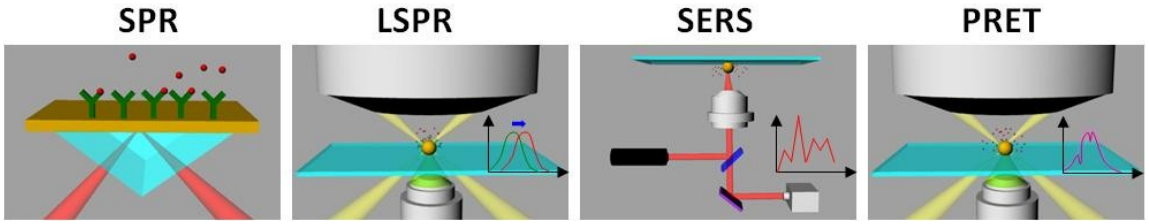

Technique	SPR	LSPR	SERS	PRET
sensitivity	~pM[7]	~10pM[8]	~100 fM[9]	~nM[10]
detection range	~1000 nm	~30 nm	~30 nm	~30 nm
spatial resolution	10 μm*10 μm	nanometer-scale	nanometer-scale	nanometer-scale
label-free detection	Yes	Yes	Yes	Yes

Figure 2.1 Four different technologies for biomolecular detection: surface plasmon resonance (SPR), localized surface plasmon resonance (LSPR), surface-enhanced Raman spectroscopy (SERS), and plasmon resonance energy transfer (PRET).

2.2 Nanoparticle arrays for biosensing

The development of nanoplasmonic materials begins with colloidal gold or silver nanoparticle suspended in solution made by chemical synthesis. For imaging or detection application, these nanoparticles are usually immobilized onto rigid substrates by chemical bonding or electrostatic force. There is alternative of directly patterning the specific shaped nanoparticles on the substrate based on the technologies developed for the micro-fabrication, such as photolithography, e-beam lithography and thin film deposition or etching with self-assembled nanometer-scale templates. To get better uniformity of the signal, the nanostructures are usually patterned on substrate with short range or long range orders, and rectangular array and hexagonal arrays are the most often adopted formats.

Arrayed metal nanoparticle substrates are good for both fundamental research and sensor applications for the following reasons: 1) uniform distributed nanoparticles result in repeatable plasmonic response across the substrate to ensure reliable sensing performance; 2) interparticle distance is well controlled to provide another degree of freedom of tuning the plasmonic resonance and the electromagnetic coupling between the particles are often used to design "hot spots;" 3) several grating dependent optical phenomenon such as photonic crystal and propagating surface plasmons can be excited from the periodically patterned metal nanoparticles; 4) the arrayed particles have higher area density than randomly distributed particles and thus can provide stronger signal per excitation area.

In this chapter, we discuss the methods of fabricating the metal nanoparticle arrays and their optical properties. Focusing on the sensor applications of the metal nanoparticle array, the recent research reporting biomolecular detection by the localized surface plasmon resonance (LSPR) peak shift and surface enhanced Raman scattering (SERS) are summarized.

2.2.1 Fabrication methods of the metal nanoparticle arrays

a). Top down : focused ion beam, e-beam lithography, nanoimprinting

In microfabrication, the patterning method relies on photo lithography, which has a resolution limitation around 100 nm because of the photon diffraction. To surpass this limitation, the photon flux for pattern generation is replaced by heavier particles such as electrons or gallium ions to improve the resolutions to 20nm and 5nm for e-beam lithography and focused ion beam (FIB), respectively. The metal nanoparticle array fabricated by e-beam lithography or FIB was typically used in the research level focus on investigating the physics of arrayed substrates. Large area substrates are difficult to fabricate by these two methods due to the slow and expensive serial fabrication process, which limits the potential for the marketable products.

Nanoimprint lithography(NIL) is a simple nanolithography process which creates patterns by mechanical deformation of imprint resist. The imprint resist is molded and cured by heat or UV light during the imprinting process.[11] The mold of the nanoimprint is made by e-beam lithography or deep UV lithography which counts as the major cost. Since the mold can be used many times before wearing out, it provides lower cost than e-beam or FIB for wafer-scale nanoparticle array fabrication. The resolution that has been reported for NIL is around 10 nm.

b). Bottom up: nanosphere lithography, block copolymer lithography, AAO

Several interesting fabrication methods for metal nanoparticle arrays use naturally formed templates as the masks for thin film deposition or etching. Nanosphere lithography is a fabrication method introduced by Hulteen et al.[12] to produce self assembled closed-packed

polystyrene nanosphere arrays on a hydrophilic substrate that allows deposition of noble metal onto a substrate through the interstitial regions of the mask. The resulting triangular nanoparticle array remains after removal of the polystyrene nanospheres. Using arrayed nanosphere as the mask for thin film deposition and directional etching, other substrate such as nanopillar[13], nanovoid[14] and nanohole[15] arrays are also reported. Due to the improvement of the monodispersion of the nanosphere fabrication and the technique to create large area monolayers, this technology has potential for commercialized nanoplasmonic sensing applications. The limitation of nanosphere lithography is the difficulty to form the monolayer of the polystyrene nanosphere size below 200 nm, and the metal particle shape is limited to trianglular or circular shape. Also, it is difficult to extend the defect free area in the nanoparticle array above 100 μm^2.

Block copolymer synthesis is another technique that enables patterning of ordered domains with dimensions below photolithographic resolution over wafer-scale areas. A block copolymer system composed of specific ratio of polystyrene (PS) and poly-methylmethacrylate (PMMA), under suitable processing conditions, will cause the PS and PMMA to spontaneously microphase separate into a hexagonal lattice of PMMA cylinders in a background of PS. After UV exposure, the PMMA is degraded and removed, leaving the hexagonal arrayed nanoholes in PS matrix. The limitation of this technology is that the pore diameter and lattice periodicity cannot be controlled fully independently; also the thickness (~40 nm) limits metal deposition to below 10 nm for lift-off process and the thin template is easily destroyed during the RIE.[16]

Anodic aluminum oxide films have ordered porous structures with close-packed hexagonal pores that can be used as nanofabrication templates. Since the pore can be made very deep, the AAO is often used as the nanowire or nanorod templates. The limitation of the technology is the periodicity is fixed by the oxidization process and results in limited degrees of freedom for designing the LSPR substrates.[17]

Another way for patterning arrayed nanoparticles is synthesis of metal nanoparticles in suspension, followed by wet coating method such as Langmuir–Blodgett or self-assembled monolayer (SAM) to pattern the nanoparticles array to a solid substrate. Gold nanosphere,[18] nanorod[19] and nanoshell[20] arrayed have all been reported by using the wet coating methods. The limitation of this technique is that only closed packed metal nanoparticle arrays can be generated, and thus the applications are limited.

2.2.2 Optical properties of nanoparticle arrays

In a metal nanoparticle array, there are two major factors to determine its optical properties: the localized surface plasmon resonance (LSPR) for each individual element and the electromagnetic interaction between the nanoparticles in the array. The LSPR of the individual nanoparticles is highly influenced by the size, shape and composition of the nanoparticle as we discussed in Chapter 2.1. The EM coupling between the particles is related to the interparticle distance and the arrangement of the particles. To design a good biomolecular detection system, both factors need to be optimized to fit the operation wavelength in order to maximize detection sensitivity.

Somel research has been focused on interparticle EM coupling. Starting from the simplest system, the LSPR wavelength of a pair of nanoparticles exhibits a red shift when the nanoparticles approach closely to each other and the polarization of the incident light is parallel to the interparticle axis, while blue shifting occurs when the polarization is perpendicular to the axis.[21] This can easily be explained in terms of static dipolar coupling between the nanoparticles,

which have a $1/d^3$ dependence on nanoparticle separation. The consequences of static dipolar interactions for planar arrays is known from the work by Murray and Bodoff in which red shifts were observed for coupled vibrational dipoles in planar arrays with in-plane polarization. For nanoparticles with small enough separations as 5-15 nm, the electrostatic interactions should dominate, and high field enhancement is expected at the junction in between the nanoparticles. This near field coupling has also been demonstrated to propagate the EM wave along a linear array of particles.

However, for nanoparticles which have larger separations comparable with the wavelength of light, electromagnetic coupling between nanoparticles can lead to more complex behavior. With in-plane polarization, a decrease in lattice spacing yields a LSPR blue shift for large separations (>100 nm). The blue shifts demonstrate the importance of radiative dipolar coupling (which has a 1/d dependence on nanoparticle separation) and retardation (which multiplies the dipole field by e^{ikd}) for larger interparticle distances.[22]

When the sub-wavelength separation arrayed nanoparticles is patterned on a continuous film, for example, some hemisphere bumps, the interesting plasmon bandgap is observed. The periodic structure acts like grating for generation of propagating surface plasmon (SP), and when the period of the nanostructure is half that of the effective wavelength of the SP mode, scattering may lead to the formation of SP standing waves and the opening of an SP stop band. When the surface is modulated in both in-plane directions, for example by a periodic array of bumps, SP modes may be prevented from traveling in any in-plane direction, thus leading to a full PBG for SP modes.[23] Similar surface plasmonic effect has also been reported on the hole array on a metal film for transmission enhancement.[24] These results all are the merit coming from the periodic arrangement of nanoparticles, and we can make a good use of them for designing specific biomolecular sensors.

2.2.3 LSPR biosensor by metal nanoparticle array

For LSPR sensing, the position change of the resonance peak due to the change of the ambient refractive index resulting from the binding of molecules of interest is the reporter of the measurement. To maximize the detection sensitivity, the shape of the individual particles and the parameters for arraying the particles need to be well-designed. At the single nanoparticle point of view, increasing the aspect ratio of the nanostructure to create inter-particle hot spots such as sharp tips or interparticle coupling to get higher peak shift sensitivity (higher refractive sensitivity and smaller field decay length as explained in Chapter2.1) is the design goal. One example of the shape enhancement sensitivity was reported by A Lesuffleur et al. They patterned the double-hole array by overlapping two holes in each element. For the high field enhancement region, such as near the apexes, the short electrical field decay length is expected to cause enhanced adsorbate detection sensitivity. The measured shift of 600 nm indicates that the double-hole increase the sensitivity 1.5 times that of the circular hole array.[25] For arrayed nanoparticle substrates, there is another degree of freedom for optimizing the sensitivity: by maximizing the interparticle coupling, we can create hot spots in the array for further signal enhancement.

Table 2.1 lists the bulk refractive sensitivity of different substrates ranking with their amount of shift per change of refractive index unit. Interestingly, the large shift comes from the pattern with periodic hole array. For the separate metal nanoparticle array, the triangle array fabricated from nanosphere lithography still has the biggest amount shift. The most peak shift so far comes from the continuous film with arrayed nano-pattern on it. For example, the triangle

hole array patterned by the nanosphere lithography followed by 200 nm Ag deposition was reported to have 480 nm/RIU sensitivity[26]. The hole array demonstrates 400nm / RIU sensitivity[27] and boost to 600nm when the hole is replace by the double hole array[25]. For these continuously film, it is hypothesized that LSPR, SPR and the interaction with these two modes are contributing to the plasmonic peak shift. When performing the LSPR based biosensing, the bulk sensitivity, m, as well as the decay length l_d need to be optimized. This is an important point to get better sensing capability of the surface binding events.

Substrate	LSPR sensitivity	Authors
double nanohole array	600 nm/RIU	A. Lesuffleur et al. (2007)[25]
nanohole array	400 nm/RIU	A. G. Brolo et al. (2004)[27]
Silver triangle array	350 nm/RIU	A. J. Haes (2002)[8]
Gold nanoislands	68 nm/RIU	E. Hutter et al. (2003)[28]
Gold nanocaps	63 nm/RIU	M. Himmelhaus et al. (2000)[29]

Table 2.1 LSPR shift sensitivity of different nanostructure arrays

2.2.4 SERS from metal nanoparticle array

Molecular vibrations have characteristic frequencies in the infrared spectral region. When light is scattered from the molecule, some photons will transfer their energy to the molecules' vibration and result in lower frequency than the incident light. Plotting the spectrum of this scattered light yields a unique molecular finger print. However, Raman is a very weak process, with molecular cross-sections in the 10^{-29} –10^{-32} cm^2 range. When the molecule under detection is in close proximity of the noble metal nanoparticles, the enhanced field due to the localized surface resonance can enhance the Raman Scattering signal. Previously, SERS signal has usually relied on random "hot spots" and this limits the potential for repeatable biosensing applications. This problem can be solved by using uniform nanoparticle arrays.

In order to enhance the SERS signal in metal particle arrays, it is important to have sharp edges and large curvature in the individual nanostructures. Another good strategy to get stronger SERS signal is to use closely patterned nanoparticle arrays and take advantage of the strong coupling field in the sub-10 nm gap in between the adjacent particles. Finally, the resonance peak of the metal particle array can be adjusted to fit the excitation laser and the absorbance peak of molecules under detection.

Table 2.2 lists several nanoparticle arrays and their demonstration of SERS capability. Besides the goal of designing a high enhancement substrate, the arrayed nanoparticles also provide a good tool of understanding the physics behind the SERS effect. The nanoparticle arrays with well separate elements of narrow LSPR bands were good for these investigations. N Felidj et al. used elongated gold nanodisk arrays with two different LSPR peaks regarding to the polarization of the laser and conclude that SERS signal is maximized with the LSPR peak tuned between the excitation wavelength and the Raman scattering signal wavelength under fixed laser excitation.[30] Haes, van Duyne and co-workers used the wavelength tunable laser on the triangle

particle array to show that the SERS gain was maximized when the LSP wavelength λ_{LSP} was located between λ_{EXC} and λ_{RS}.[31] The SERS efficiency of gold nanowires arrays fabricated by electron beam lithography and lift-off technique are investigated by depositing a molecular probe (BPE) trans-1,2-bis(4-pyridyl)ethylen on the arrays and using an excitation wavelength of 632.8 nm. The observation of the dependence of the Raman enhancement versus the nanowire length is clearly demonstrated; and remarkably a maximum enhancement is observed.

For the close packed nanoparticle array with nanogaps in between each element, A. Wei et al. treated the gold nanospheres with resorcinarene tetrathiol to create self-organizing planar closed packed arrays and demonstrated the SERS by optimizing the LSPR of the film. H. Wang used self-assembled nanoshell array for combining two functions, SERS and surface enhanced absorption spectroscopy, into one substrate. H. H. Wang grew silver nanoparticles in the AAO hole array and demonstrated SERS signal resulting from the sub-10nm gap in-between each silver nanoparticles.[32]

Substrate	SERS demonstration condition	Authors
Gold nanodisk array	$5*10^{-4}$ BPE solution	N. Felidj et al. (2006)[33]
Colloidal gold nanoparticle array	Adsorbed tetrathiol	A wei et al. (2001)[34]
Gold nanosphere array	Adsorbed para-mercaptoaniline	H Wang et al. (2007)[35]
Gold nanowire array	10^{-3} BPE solution	L. Billot et al. (2006)[36]
Nanohole array	Adsorbed oxa	AG Brolo et al.(2004)[37]
Silver particle array on AAO	10^{-6} R6G	H. Wang et al. (2006)[38]
Silver nanorod array	Adsorbed BPE	SB Chaney (2005)[39]
Triangle silver nanoparticle array	Adsorbed benzenethiol	AD McFarland (2005)[40]
Silver particle array	10^{-5} R6G	Y. Lu et al. (2004)[41]

Table 2.2 SERS detection results of different nanostructure arrays

2.2.5 Integration with microfluidic systems

A big portion of the nanoparticle-based chemical sensing experiments mentioned above are done in home-made fluidic cells trying to control the testing environment. The microfluidic system can provide better microenvironment control for the measurement of nanoparticle arrays. However, there is no research being reported regarding the integration with microfluidic and nanoparticle array biosensors so far as we know. In the following chapters, the key components developed for integration of metal nanoparticle arrays and the dynamic cell culture systems will be reported and it is convincing that this integration platform has a great potential for future cell-based assays.

2.3 Microfluidic cell culture

Microfluidics is a technology that manipulates fluid by channel systems with dimensions less then hundreds of microns. The fluid flow in microfluidic channels has small Reynold's number and is dominated by laminar flow, which is capable controlling the distribution of particles in the flow. Microfluidics offers an infrastructure of lab-on-a-chip system, and has the potential to be integrated with other electric, optical and mechanical miniaturization systems. The basic building material of microfluidic devices is an elastic polymer, poly-dimethylsiloxane (PDMS), which is optically transparent and oxygen permeable material. These two characteristics make PDMS microfluidic devices suitable for cell culture and observation. The advantages of culturing cells on microfluidic chip include:

1) The dimensions of microfluidics are at the same order of the size of cells (10s micrometer), and this allows precisely transferring and positioning of the cells.
2) Only small amount of reagent is needed in the microfludics and the well-developed valve and pump systems can assist multiple chemical reagent delivery and control for the high-throughput tests.
3) The media perfusion system of the microfludics provides more physiological mimic culture condition. The fresh media is continuously supplied as well as cell metabolism waste preclusion.
4) The flow allows shear stress control or stimuli to the cultured cells.

2.3.1 Shear stress and mass transport considered for cell culture microfluidic design

In order to design a microfluidic system ideal for cell culture and assay, there are two important parameters need to be precisely controlled: 1) shear stress 2) mass transport, and I will discuss both points as follows:

During the cell culture, the shear stress from the perfusion flow needs to be controlled to avoid the unwanted cell behavior triggered by the shear forces. Shear stress happens when fluid moving along the boundary, thus solving the flow field can give out the answer of how much shear stress is acted at cells or other surfaces. To analyze the fluid dynamics in the cell culture device, we need to go back to the basic of fluidic dynamic theory. Starting from the Navier-Stokes equation for incompressible fluids[42]:

$$\rho(\partial_t v + (v \cdot \nabla)v) = -\nabla P + \eta \nabla^2 v + \rho g + \rho_{el} E \quad \text{.....(2.15)}$$

where ρ is the density, v is the fluid velocity vector, P is the pressure, η is viscosity, g is the gravity and E is the electric field. Considering the case under steady-state with no external gravity and electric field, the Navier-Stokes equation is then written as:

$$0 = -\nabla P + \eta \nabla^2 v \quad \text{.....(2.16)}$$

By setting the pressure of inlet and outlet, we are able to calculate the velocity and the corresponding shear stress information at the area near the cell surface by:

$$\sigma_{ik}' = \eta(\partial_k v_i + \partial_i v_k - \frac{2}{3}\delta_{ik}\partial_j v_j)$$

$$\delta_{ik}' = 0 \text{ when i = k and } \delta_{ik}' = 1 \text{ when i} \neq \text{k} \quad \text{.....(2.17)}$$

The shear stress in specific microfluidic design can be calculated by simulation software such as COMSOL v 3.4.

The displacement of molecules or particles inside the microfluidic system can be caused by diffusion and convection. The mass transport of molecules in a microfluidic system can be described by convection-diffusion equation:

$$\frac{\partial C}{\partial t} + v \cdot \nabla C = D\nabla^2 C \quad \text{.....(2.18)}$$

Solving the equation with proper boundary conditions can help us control the concentration distribution of nutrition or drugs and optimize the cell culture system. One example of utilizing convection-diffusion to analyze the mass transport is regarding to the surface binding reaction in the microfluidic channel. If we look at the cross-section of the microfluidic cell culture devices, for the adhesion type of the cell, the cells are usually attached at the bottom of the device. The nutrition or drug molecules that contact to the cells will bind to the cell surface receptors and be consumed by the cells. The similar case is in the biosensor area, where the surface functionalized with antibodies, and the incoming antigen binds to the surface, depleting the local concentration. We can simplify the question in a 2D case with flow in a infinite parallel-plate channel, and the parabolic flow front can be describe as:

$$v_x(z) = \frac{\Delta P}{2\eta L}(h - z)z \quad \text{.....(2.19)}$$

With boundary condition as

$$v_x(0) = 0,$$

$$v_x(h) = 0$$

For the molecule, the boundary condition can be set as:

$C(0) = C_0$ along the parabolic flow at inlet,

$\frac{\partial C}{\partial n} = 0$ at the upper wall (n is the normal vector to the wall)

$$D\nabla C = \frac{\partial B}{\partial t}$$

where B is the number of surface binding events. The mass transport in microfluidic design can then be calculated by simulation software such as COMSOL v3.4.

2.3.2 microfluidic cell culture technologies

For the past decade, a great amount of cell based research was working under “lab-on-a-chip” or “micro-total-analysis-system” framework. According to different cell lines and different type of cell assays, a variety of microfluidic platforms have been demonstrated. However, there

are some commonly used components or technologies for on-chip cell culture system. Here, these commonly used tools are classified into three categories: 1) flow control system 2) laminar flow assisted reagent delivery 3) surface modification and scaffold for cell attachment. They are introduced separately as follows:

1) Flow control system –pump, valve and bubble filters

To generate the flow in microfluidic channels, proper pumping systems are necessary. Syringe pump are commonly used in perfusion of the on-chip cell culture system, but the big size makes it not possible for the miniaturized system to be put into the cell incubator. Several on-chip pumps such as electro-osmosis pump, piezo-actuator pump, and reciprocal pumps have been reported. To control the flow to enter or shunt to a specific channel, valves systems are usually integrated within the cell culture chip. The valve system also enables multi-injection of different reagents into one main channel. Based on the elastic property of PDMS, the valve is usually operated by applying a mechanical force on top on the channel that pinches a fluidic channel closed. One well-developed method of applying the vertical force is by aligning a second channel layer above the main flow channels and the valve works while the top control channel is expanded by air or water. Finally, to provide a stable cell culture environment, the air bubbles that are easy to destroy the bi-lipid membrane of the cells need to be avoided. There are several designs to trap or filter out the air bubbles coming with the perfusion flow, as well as the de-bubbler by applying vacuum to adjacent chambers.

2) Flow assisted reagent delivery – gradient generator, flow focusing

The low Renold's number in microfluidics enable a good control of mass transport of the reagent molecules in the flow. Hrdrodynamic focusing is usually applied to confine the reagents in a specific area. On the other hand, to well mix two streams of laminar flows, several mirofluidic mixers were reported. Gradient generator is a component that applies both of the techniques above, two stream of laminar flow are divided and mixed to form a linear or longitudinal distribution of the flow and this enables a high throughput drug assay.

3) Surface modification and scaffold for cell adhesion

The microfluidics provide more in-vivo like perfusion system and the in-vivo ECM like surface chemistry of the cells rely on surface modification techniques. For the glass substrate, silane molecules such as poly-L-lysine are often used to create hydrophobic surface for cell attachment, while silanized PEG is often use to create a hydrophilic surface preventing cell attachment. A bunch of hydrogel based material has been integrated within the microfluidic culture system to create 3D scaffolds to better mimic the in-vivo cell patterns,

References:

(1) Maier S. A, *Plasmonics: fundenmental and applications*, Springer, 2007.
(2) Malinsky, M. D. *J. Am. Chem. Soc.* **2001,** 123, 1471-1482.
(3) Baker, G. A. *Anal Bioanal Chem* **2005**, 382, 1751–1770.
(4) Liao, P. F.; Wolaun A. *J. Chem. Phys.* **1982**, 76, 751-752.

(5) Kang, J. H.; Kim, D. S.; Park, Q. Phys. Rev. Lett. **2009**, 102, 093906-1-4.
(6) Liu, G. L.; Long, Y. T.; Choi, Y.; Kang, T.; Lee, L. P. *Nature methods*, **2007**, 4, 1015-1017.
(7) Homola, J.; Yee, S. S.; Gauglitz, G. *Sensors and Actuators B* **1999**, 54, 3–15.
(8)) Haes, A. J.; Chang, L.; Klein, W. L.; Van Duyne R. P. *J. Am. Chem. Soc*, **2005**, 127, 2264-2271.
(9) Liu,G.; Lee, L. P. *Appl. Phys. Lett.* 2005, 87, 074101-1-3.
(10) Choi, Y.; Park, Y.; Kang, T.; Lee, L. P. Nature Nanotechnology, 2009, 4, 742-746.
(11) Chou, S. Y.; Krauss P. R.; Renstrom P. J. *Science* **1996**, 272, 85–87.
(12) Hulteen, J. C.; Van Duyne R. P. *J. Vac. Sci. Technol. A* **1994**, 13, 1553-1558.
(13) Cheung, C. L.; Nikoli´c, R. J.; Reinhardt, C. E.; Wang, T. F. *Nanotechnology* **2006**, 17, 1339-1343.
(14) Teperik, T. V.; Popov, V. V.; García de Abajo, F. J. *Phys. Rev. B* **2005**, 71, 085408.
(15) Prikulis, J.; Hanarp, P.; Olofsson, L.; Sutherland, D.; and Kall M. *Nano Letters***2004,** 4, 1003-1007.
(16) Guarini, K. W.; Black, C. T.; Milkove, K. R.; Sandstromet R. L. *J. Vac. Sci. Technol. B* **2001**, 19, 2784-2788.
(17) Matsumoto, F.; Ishikawa, M.; Nishio, K.; Masuda, H. *Chemistry Letters* **2005,** 34, 508-509.
(18) Kim, B.; Tripp, S. L.; Wei, A. *J. Am. Chem. Soc.* **2001**, 123, 7955-7956.
(19) Kim, F.; Kwan, S.; Akana, J.; Yang, P. *Am. Chem. Soc*. **2001**, 123, 4360–4361.
(20) Wang, H.; Kundu, J.; Halas N. J. *Angewandte Chemie* **2007**, 46, 9040-9044.
(21) Rechberger, W.; Hohenau, A.; Leitneret, A.; Krenn, J. R.; Lamprecht B,; Aussenegg F. R. *Optics Communications* **2003**, 220 137-141.
(22) Haynes, C. L.; McFarland, A. D.; Zhao, L.; Van Duyne R. P.; Schatz, G. C. J. *Phys. Chem. B,* **2003**, 107 7337-7342.
(23) Barnes W. L.; Dereux, A.; Ebbesen T. W. *Nature* **2003**, 424, 823-830.
(24) Klein Koerkamp, K. J.; Enoch, S.; Segerink, F. B.; van Hulst, N. F.; Kuipers, L. *Phys. Rev. Lett.* **2004**, 92, 183901.
(25) Lesuffleur, A.; Im, H.; Lindquist, N. C.; Oh, S. H. *Appl. Phys. Lett*. **2007**, 90, 243110.
(26) Hicks, E. M.; Zhang, X.; Zou, S.; Lyandres, O.; Spears, K. G.; Schatz, G. C.; and Van Duyne, R. P. J. *Phys. Chem. B* **2005**, 109, 22351–22358.
(27) Brolo, A. G.; Gordon, R.; Leathem, B.; Kavanagh, K. L. *Langmuir* **2004**, 20, 4813-4815
(28) Hutter, E.; Pileni, M. *J. Phys. Chem. B* **2003**, 107, 6497–6499
(29) Himmelhaus, m.; Takei, H. *Sensors and Actuators* **2000**, 63, 24-30
(30) Felidj, N.; Aubard, J.; Le´vi, G.; Krenn, J. R.; Hohenau, A.; Schider, G.; Leitner, A.; Aussenegg, F. R. *Appl. Phys. Lett***. 2003**, 82, 3095-3097
(31) McFarland, A. D.; Young, M. A.; Dieringer, J. A.; Van Duyne R. P. *J. Phys. Chem. B* **2005**, 109, 11279-11285
(32) Wang, H.; Liu, C.; Wu, S.; Liu, N.; Peng, C.; Chan, T.; Hsu, C.; Wang, J.; Wang, Y. *Adv. Mater***. 2006** 18 491–495
(33) Felidj, N.; Aubard, J.; Levi, G.; Krenn, J. R.; HohenauA.; Schider, G.; Leitner, A.; and Aussenegg F. R.; *Applied physics letters* **2003**, 82, 3095-3097
(34) Wei, A.; Kim B.; Sadtler, B.; Tripp S. L. *ChemPhysChem* **2001**, 12, 743-745
(35) Wang, H.; Levin, C. S.; Halas, N. J. *J. Am. Chem. Soc.* **2005**, 127, 14992-14993.
(36) Billot, L.; Chapelle, M. L.; Grimault, A. S.; Vial, A.; Barchiesi, D.; Bijeon, J. L.; Adam, P. M.; Royer P. *Chemical Physics Letters* **2006**, 422, 303–307.

(37) Brolo, A. G.; Arctander, E.; Gordon, R.; Leathem, B.; Kavanagh, K. L.*; Nano Lett*. **2004**, 4, 2015-2018
(38) Wang, H.; Liu, C.; Wu, S.; Liu, N.; Peng, C.; Chan, T.; Hsu, C.; Wang, J.; and Yuh-Lin Wang, Y. *Adv. Mater.* **2006**, 18, 491–495
(39) Chaneya, S. B.; Shanmukh S.; Dluhy, R. A.; Zhao, Y. P. *Applied physics letters* **2005**, 87, 031908-1-3
(40) McFarland, A. D.; Young, M. A.; Dieringer, J. A.; Van Duyne, R. P. *J. Phys. Chem. B* **2005**, 109, 11279-11285
(41 Lu, Y.; Liu, G. L.; Lee L. P. *Nano Lett* **2005**, 5, 5–9
(42) Bruus, H. *Theoretical microfluidics* **2008.**

CHAPTER 3:
CRESCENT-SHAPED NANOHOLE ANTENNA AS A SENSITIVE BIOSENSOR

3.1 Introduction

Since the discovery of extraordinary transmission of light through sub-wavelength holes,[1] much attention has been devoted to understanding the role of material properties, film thickness, hole geometry, and relative hole placements in the optical response of hole and hole arrays.[2,3] Recently, it has been shown that such structures may also act as optical antennaes utilizing local surfc.ace plasmon resonances (LSPR) of the nanohole structures to focus electromagnetic fields into extremely small regions.[4] Such hole-based optical antennae have the potential to become powerful biomolecular sensors. Molecular detection techniques based on LSPR shift,[5] surfaced-enhanced Raman spectroscopy (SERS),[6] surface-enhanced fluorescence (SEF),[7] and plasmon resonance energy transfer (PRET)[8] are all highly dependent on the intensity of localized electromagnetic fields, called "hot spots". While many nanoparticle-based techniques have been investigated as substrates for plasmonic-based detection via hot spots, hole geometries may offer significant advantages, including integratability (i.e., integrated optical devices or optical micro/nanofluidics), robustness, and the potential to nanoconfine analyte in hot spot regions.[4,10]

Hole-based plasmonic sensors have suffered from two problems. First, the hole structures have not achieved the sensitivity of nanoparticle-based approaches.[11] This may be largely attributed to limited effort in designing for molecular detection, which is typically focused on creating hot spots near plasmonic surfaces. The optimal hole structures for hot spot creation are likely to be different than structures for maximizing transmission, which has been a large focus since the discovery of extraordinary optical transmission. Specifically, sharp-tip and nanogap geometries are required for high molecular sensitivities. Second, virtually all studies of hole-based arrays have been based on slow and expensive "top-down" approaches such as e-beam lithography or focused ion beam (FIB) fabrication. The serial nature of these techniques allows only small regions to be fabricated, and it is both difficult and not costeffective to integrate such structures into integrated sensing architectures, such as optical microfluidic and nanofluidic devices. In addition, such top-down techniques typically cannot define feature sizes less than 10 nm, which is a critical limitation in creating ultrasharp features for plasmonic detection. We note that several methods to develop large area circular hole arrays, such as nanosphere lithography,[12] microsphere lenses,[13] and soft interference lithography,[14] have recently been developed.

In this chapter the first demonstration of large area noncircular random hole arrays is presented. We have used nanosphere lithography to create random arrays of crescent-shaped nanoholes, as shown in Figure 3.1, and have fabricated such structures on a 4 inch wafer scale, while reproducibly creating sub-10-nm sharp features without using e-beam or FIB. We demonstrate that crescent hole structures serve as counterparts to gold crescent-shaped nanostructures, called nanocrescents, which have been established as powerful plasmonic biosensors in recent years theoretically[15,16] and experimentally.[17-23] With both systematic experimental and computational analysis, we characterize the optical properties of crescent-shaped nanohole antennae and demonstrate their tuning capability by varying all key geometric

parameters. Finally, we demonstrate the LSPR peak shift and SERS for molecular sensing on the crescent-shaped nanohole substrate

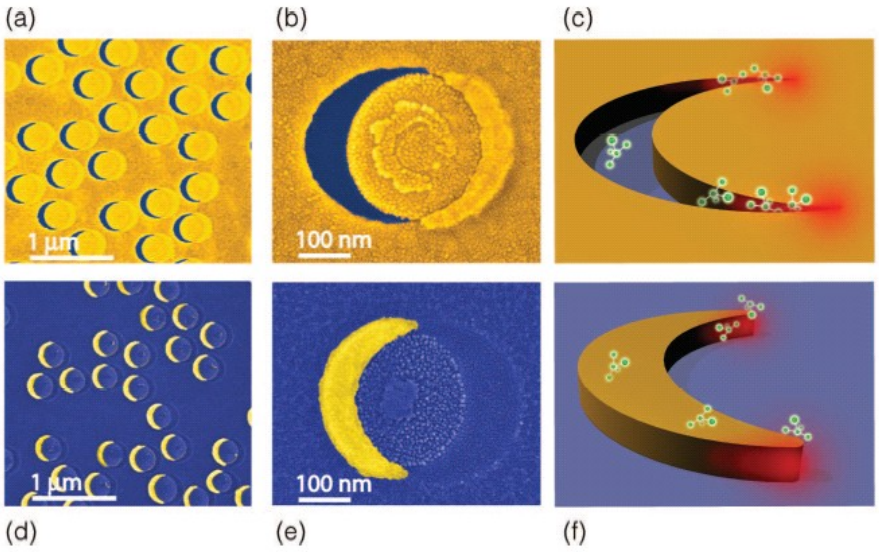

Figure 3.1 Overview of the anti–nanocrescent and nanocrescent structures; SEM images (false color) of (a)(d) random arrayed and (b)(e) single structures, and (c)(f) a conceptual illustration of molecular detection for (a)–(c) anti–nanocrescents and (d)–(f) nanocrescents. The anti–nanocrescent achieves sharper tips with < 10nm radius of curvature, and is amenable to integrated flow–through architectures for molecular detection.

3.2 Methods

3.2.1 Substrate fabrication

The process flow of crescent-shaped nanohole fabrication is shown in Figure 3.2. Briefly, a 2 nm thick titanium adhesion layer and a gold layer of defined thickness were deposited onto clean glass slides by e-beam evaporation (Edwards EB3). Random monolayer arrays of polystyrene (PS) spheres (Polysciences) were then deposited on the gold films as follows: PS sphere suspension, 10 mM N-(3-(dimethylamino) propyl)-N′-ethylcarbodiimide (Sigma-Aldrich) solution in phosphate-buffered saline (pH 7.4, Gibco), and deionized water (Millipore) were mixed at a ratio of 1:0.9:1. The gold surfaces were immersed in the mixture for 1 h, during which PS spheres were adsorbed to the substrate. Nonadsorbed spheres were washed away with a copious amount of deionized water, and the substrates were dried with N2 gas. The size of the adsorbed PS spheres can be tailored with oxygen plasmon treatment (Plasma-Therm PK-12 RIE, at 50 sccm, 100 W). The sphere-coated substrates were then etched using vertical angle ion milling (Veeco Microtech System), after which all of the gold is removed except for a nanodisk masked by each PS sphere. A second gold layer was then deposited on the substrate at a defined angle using e-beam evaporation, at a thickness which matched the initial gold layer. The gold cannot enter the area shadowed by the PS sphere, and a crescent-shaped void results. Finally, PS spheres were removed using tape (Scotch, 3M) and sonication in acetone for 1 h. For comparison, we also fabricated nanocrescents using a similar PS sphere process as shown in 3.2e-h.[20] The resulting crescent-shaped nanohole (as well as nanocrescent) antennae were thus fabricated into large-area random arrays, as shown in Figure 3.1. We used random arrays to isolate the plasmonic characteristics of individual nanostructures from short- and long-range coupling between structures that can result from periodic arrays.

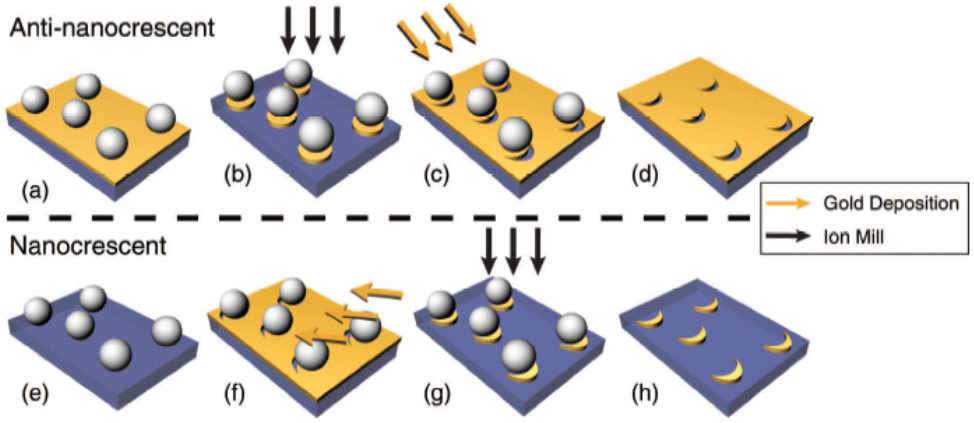

Figure 3.2 Crescent-shaped nanoholes and nanocrescent fabrication; nanosphere lithography fabrication process for (a)–(d) anti–nanocrescents and (e)–(h) nanocrescents.

3.2.2 Optical characterization

Dark-field scattering microscopy and UV-vis absorption spectrometer were used to characterize the optical response of crescent-shaped nanoholes and nanocrescents. While transmission measurements are typical for hole studies, the significant absorption and scattering of sharp crescent-shaped nanohole antennae are more appropriately measured via scattering. Hence, we used dark-field scattering microscopy for characterizing the particle plasmon resonance at the sharp tips and UV-vis absorption spectrometer for the resonance of the whole crescent-shaped nanoholes.

In our dark-field scattering configuration, broad band white light from a halogen source was passed through a dark-field water immersion condenser (NA=1.2-1.4) to illuminate the sample at an angle larger than the collection angle of the objective lens (NA=0.4). The scattering from the substrate alone was imaged by a CCD camera and a spectrometer. For UV-visible adsorption measurement, dark-field condenser was removed to allow the vertical incident while light pass through the sample, and the transmission light is collected and read out by the same spectrometer. Absorption was calculated with normalization to the spectra of light source.

To complement the experimental scattering results, we developed a three-dimensional numerical model using the commercial finite element software COMSOL. We consider a single crescent-shaped nanohole in a large gold sheet with complex permittivity ε given by an analytical model[24] of the experimental data[25] for bulk gold and with relative permeability $\mu = 1$. The crescent-shaped nanohole shape is approximated by an extruded circle subtracted from an extruded ellipse, where the major and minor axis are determined by the angle of deposition and PS sphere radius, respectively. The surrounding environment is assumed to be a vacuum.

3.2.3 LSPR peak shift measurement

To measure the LSPR peak shift of crescent-shaped nanoholes resulting from the change of the bulk surrounding media, the samples mounted on the glass slides with home-made flow cells with exchangeable media of air, water and glycerol. The adsorption spectra were measured by the same configuration as described in 5.2.2. To characterize the LSPR peak shift resulting from the change very close to the surface of crescent-shaped nanoholes, self-assembled monolayer (SAM) of alkinthio was functionalized to the surface of the substrates. The absorption spectra with and without SAM were measured and compared. Finally to demonstrate the molecular binding detection from the crescent-shaped nanoholes substrate in solution environment, biotin/ strepavidin system was adopted. The crescent-shaped nanohole substrate was incubated with 1 mM EZ-Link Biotin-HPDP (N-(6-(Biotinamido)hexyl)-3'-(2'-pyridyldithio)-propionamide for 30mins and the biotin molecules bind to the gold surface via thio bonds, after which the substrate was cleaned with ethanol and dried with N2 gas. 1 mM of Strepavidin solution was then introduced onto the crescent-shaped nanohole substrates, and the change of the absorption spectra resulting from binding of streptavidin to the biotin on the sample surface were measured every 3 mins to record the real time change of the LSPR peaks.

3.2.4 SERS measurement

The SERS measurements were performed by measuring the SERS spectra of crescent-shaped nanohole substrates immersed in known concentration of R6G solution. A 785 nm excitation laser was used since this wavelength is a widely adopted wavelength within the

biological window. The excitation power is set as 0.3 mW and the measurement area was 3 um by 1 um, defined by the focused laser spot size and the slit in front of the spectrometer.

3.3 Results and discussion

3.3.1 Optical Properties Characterization

Due to the nature of shadow-based nanofabrication, the tips of the crescent-shaped nanohole are extremely sharp, achieving a radius of curvature well under 10 nm without e-beam lithography or FIB. Such dimensions give the crescent-shaped nanohole sharper features than rectangular holes,[26] bowtie holes,[27] double holes,[28] and similar structures which have been fabricated using FIB techniques. Interestingly, the tips are found to be sharper than those of positive nanocrescents fabricated by the same PS sphere template (Figure 3.2c,g). We expect this is due to the differences in fabrication between the positive and negative crescents: some unavoidable removal of the PS sphere mask during ion-milling of the nanocrescent limits tip sharpness (Figure 3.2g), while the crescent-shaped nanohole is defined by gold evaporation through the shadow of the PS nanosphere (Figure 3.2c). The increased sharpness causes a higher computed local field enhancement for crescent-shaped nanoholes. Since it is nearly impossible to completely isolate the positive and negative masking properties of PS spheres during fabrication, a positive nanocrescent typically forms opposite each crescent-shaped nanohole during fabrication, as can be seen in the scanning electron microscopy (SEM) images of Figure 3.1b. However it is clear that this "secondary" nanocrescent does not contribute significantly to the optical signal: dark field scattering measurements were nearly identical when taken on both sides of the films (while the nanocrescent appears on only one side), and experimental results agree well with computational results of pure crescentshaped nanoholes.

For the application of plasmonic-based molecular detection, we particularly wish to study plasmon resonances of the sharp tips of the crescent-shaped nanoholes which occur in the optical regime, hence fitting within the "biological window" of visible and near-infrared wavelengths that will not harm biological tissue. For both the crescent-shaped nanohole and its nanocrescent counterpart, in the optical regime the particle plasmon (pp) resonances are dominant and occur at wavelengths near 600 nm for crescent diameters near 300-400 nm. Hence, these structures are the focus of this chapter. The geometric asymmetry of the crescent-shaped nanohole antenna causes a significant polarization dependence, as shown in Figure 3.3. In the case of the crescent-shaped nanohole, the plasmon resonance occurs across the cavity: when the incident electric field polarization is parallel to the long dimension of the crescent-shaped nanohole, denoted pp(c), primarily the tip-cavity modes are excited; when the incident field is perpendicular to the long dimension, denoted pp(u), a resonance across the center of the cavity occurs (Figure 3.3a-c). These resonances are mirrored in the nanocrescent (Figure 3.3d-f). While the peak positions of the two modes appear almost identical, the pp(u) resonance exhibits a slight red shift compared to the pp(c) mode, and this trend has also been observed in nanocrescents.[20] This supports that the polarization dependence is related to separate resonance modes, while the sharp tips may contribute significantly to the signal in both modes (as is discussed further below).

Since resonances of sharp tips are known to achieve sensitive biomolecular detection, we focus on the pp(c) polarization in the remainder of this chapter and note that the plasmon band tuning is nearly identical for pp(u) polarization. Nanosphere lithography offers three primary handles for geometric control: namely, sphere diameter d, gold deposition angle θ, and thickness of the gold film h. Understanding the effect of each of these handles is crucial for designing useful devices well as in probing the underlying physics.

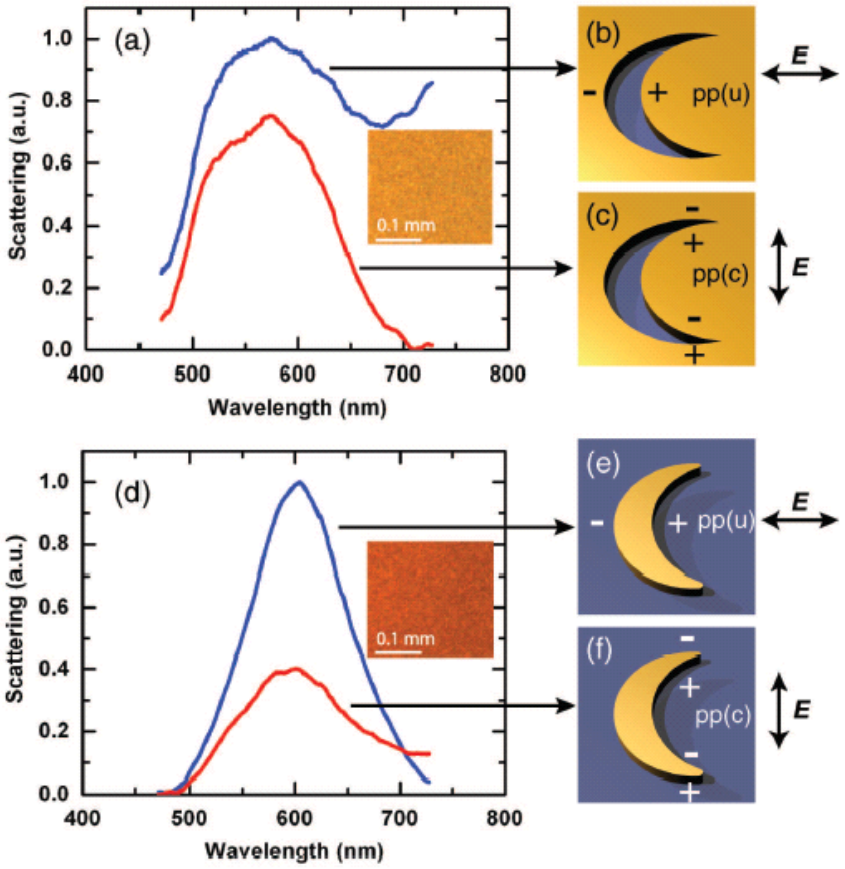

Figure 3.3 Anti–nanocrescent polarization dependence; polarization induced resonant modes of (a)–(c) anti–nanocrescents and (d)–(f) nanocrescents. Insets show dark field scattering images for (a) anti–nanocrescent and (d) nanocrescent random arrays. The pp(c) polarization excites the sharptips useful for molecular detection. The scattering curves are shown for d = 293nm, q = 30◦,h = 25nm.

We fabricated crescent-shaped nanoholes with a wide range of PS sphere sizes, finding that a strong plasmonic response in the optical regime occurred primarily for PS sphere diameters d near 300 nm, as shown in Figure 3.4. Within the size regime of d ≈ 300-400 nm a red shift in the scattering peak occurs with crescent-shaped nanohole size: for example increasing the sphere diameter from 307 to 333 nm results in a 25 nm resonance peak position difference. This behavior has been observed for many different particle and cavity geometries and is due to radiation damping and retardation. We note the magnitude of red shift agrees well with that seen for nanocrescents. In each case in Figure 3.4, the computed local field enhancement is redshifted roughly 100 nm compared to the experimental results. This difference can likely be explained from oversimplification of the computational model and real differences between resonances in the near and far fields. Specifically, the effect of the substrate has been shown to be significant for circular holes,[29] and we suspect the presence of the substrate causes differences between single and double peaks observed in the experimental and computational results. The magnitude

of peak change with increasing nanohole size is nearly identical in the experimental and computational results. Varying the gold deposition angle during crescent-shaped

nanohole fabrication allows some control over the nanohole geometry without significantly changing its size, as shown in Figure 3.5. Surprisingly, though the nanohole shape changes significantly as the deposition angle θ ranges from 10° to 45°, the peak scattering position remains nearly unchanged. To understand this result, we computationally investigated the electric field inside the crescent-shaped nanohole. It is clear from the local electric field presented in Figure 3.5c that the plasmonic response of the crescent-shaped nanohole is dominated by the sharp tips. Since the tip geometry changes only minimally with deposition angle, little change in plasmon peak wavelength would indeed be expected. Thus, the computational and experimental results are in good agreement. For a small deposition angle, a thin slitlike crescent-shaped nanohole forms, which results in increased coupling and a sharper peak. In the near field, our computation predicts local fields of |E|/|E0|) 1500 (Figure 3.5c) at resonance, where this value is taken at least 2 nm from the gold surface. The reduction of this coupling mode with increasing deposition angle causes a broadening of the plasmon peak, as seen in 3.5d. We also considered the effect of varying film thickness as shown in Figure 3.6. Since the skin depth thickness of gold is roughly 30 nm at optical frequencies, in varying the film thickness from 13 to 65 nm we progress from an optically thin film toward an optically thick film. There is an experimental limitation of the aspect ratio of crescent-shaped nanohole size to height of roughly 4 to 1, since the PS sphere template is also deformed during the ion milling process (etching rate of PS:gold ≈ 1:2). This limitation may be overcome in the future by replacing PS nanospheres with a more resilient material such as silica. The effect of film thickness on the crescent—shaped nanohole resonance position stresses that the resonance is not purely a two-dimensional effect. Simulation results suggest that at resonance the locally enhanced field progresses completely through the cavity. This is consistent with observations in holes, where the electromagnetic field is concentrated into a plasmon mode inside the cavity and is then re-emitted as light on the other side. In the crescentshaped nanohole structures in this study, we found transmission minima at the resonance wavelength, which is in contrast to transmission enhancement reported in many hole and hole arrays in films much thicker than the skin depth of gold. At the thicknesses below 65 nm used in this study, light that transmits directly through the gold film may destructively interfere with, or become significant in comparison with, the re-emitted light resulting from the plasmon resonance.[30] Similar transmission minima of hole structures have also been reported in hole studies in films of thickness close to the skin depth. [31-33]

It is clear in Figure 3.6 that as the film thickness decreases the scattering peak is red-shifted. This follows a general rule seen in many plasmonic structures[9] including holes,[32] namely, that as the aspect ratio of structure size to height is increased, a red shift in plasmon peak position occurs. This can occur either by increasing the size (Figure 3.4) or by decreasing the height (Figure 3.6) of the nanostructure. We also note that similar shifts are seen in the resonance of positive nanocrescents. Again, experimental and computational results are in good agreement. As the film thickness increases, two distinct peaks in the plasmon band begin to emerge. As shown in Figure 3.6d, this splitting is caused by a secondary coupling mode on the rounded side of the crescent-shaped nanohole. This splitting is also observed for thin crescentshaped nanoholes with smaller diameter, as shown in Figure 3.4a, which indicates that a critical aspect ratio is required for the double peak to emerge. It is clear that strong similarities exist between the optical responses of crescent-shaped nanoholes and nanocrescents. While Babinet's principle

does not rigorously apply in the regime studied here of finite conductivity and films of finite thickness,[34] the similarities presented here between the complementary structures imply that Babinet's principle is at least qualitatively upheld in this nonideal regime. This has also been recently noted in slit ring resonators (SRRs) and their hole complements.[35]

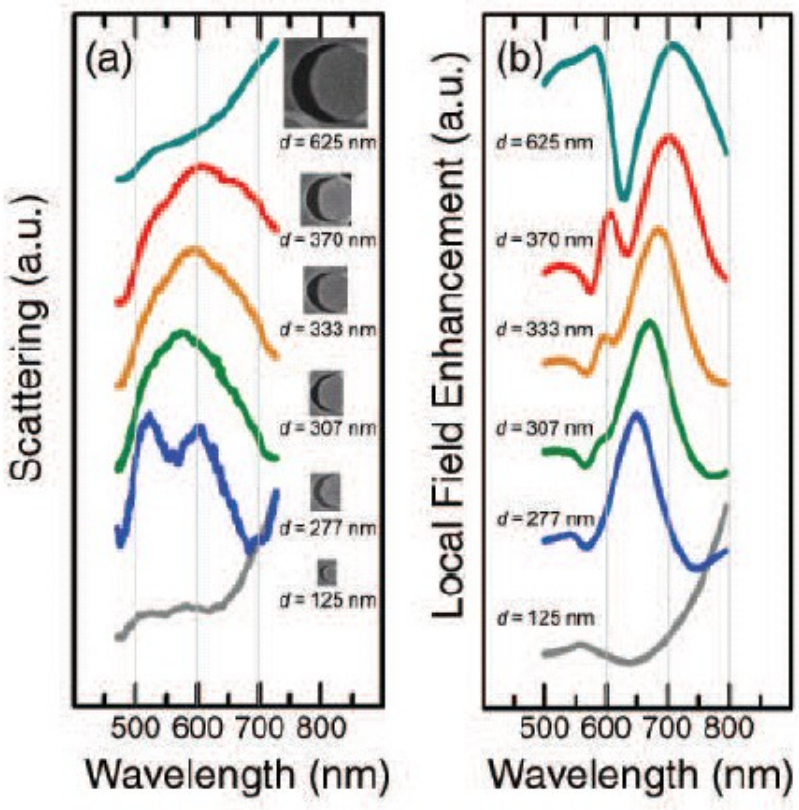

Figure 3.4 The dependence of anti–nanocrescent optical response on size; (a) experimental scattering response and (b) computed near–field show a redshift with increasing anti–nanocrescent size (q= 30◦, h = 53nm, polarization is pp(c))

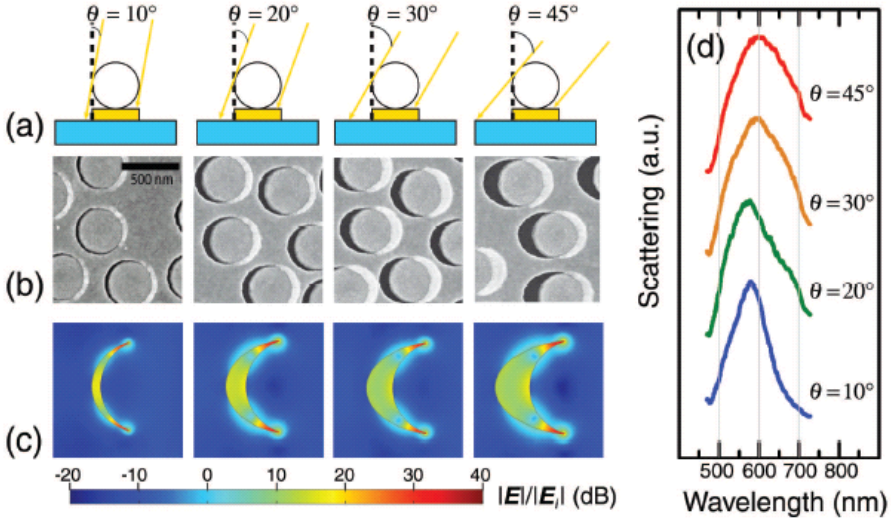

Figure 3.5 The dependence of anti–nanocrescent optical response on deposition angle; (a) side view schematic of varying deposition angle, (b) SEM images, (c) computed local electric field enhancement at resonance, and (d) experimental scattering peak for the corresponding anti–nanocrescent structures (d = 333nm, h = 53nm, polarization is pp(c)). The sharp tips dominate both the local and far–field response.

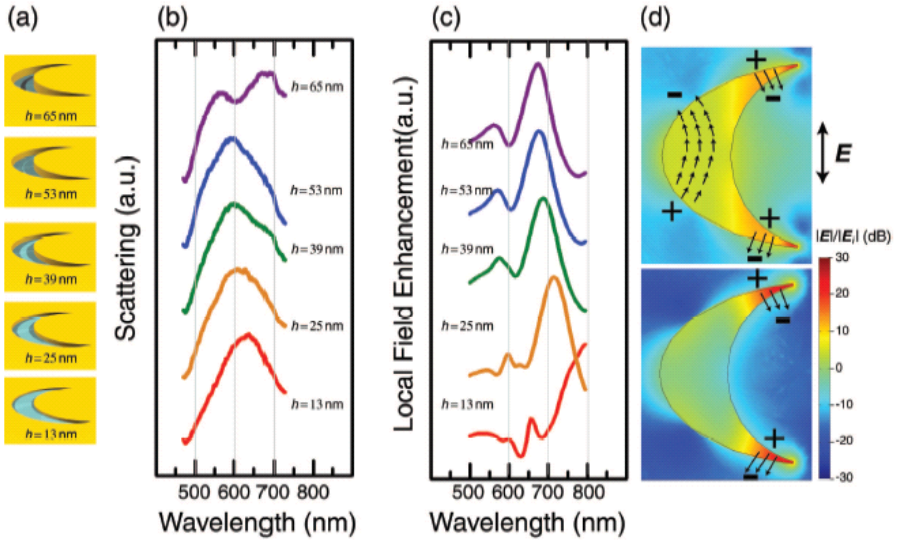

Figure 3.6 The dependence of anti–nanocrescent optical response on anti–nanocrescent thickness; (a) schematic of varying thicknesses, (b) experimental scattering response and (c) computed near–field and (d) near–field electric field distribution for (top) the secondary peak and (bottom) primary peak shown in part (c) (d = 333nm, q = 30◦, polarization is pp(c)). A redshift occurs with decreasing anti–nanocrescent thickness, while a second peak emerges for optically thick films.

After checking the pp mode, let's focus on longer wavelength region of the plasmon resonance among the whole crescent-shaped nanohole. Based on the polarization of the incident light, there two resonance mode which we named C mode (incident electric field polarization parallel to the long dimension of the crescent-shaped nanohole) and U mode (incident electric field polarization perpendicular to the long dimension of the crescent-shaped nanohole), following the terminologies defined in the crescent-shaped nanoholes. The resonance peaks of the C and U modes happened in the infrared range and we characterize the LSPR peaks as in Figure 3.7. These LSPR peaks are sitting within the biological window that has limited absorption in the living cells and can make sure good LSPR peak signal quality.

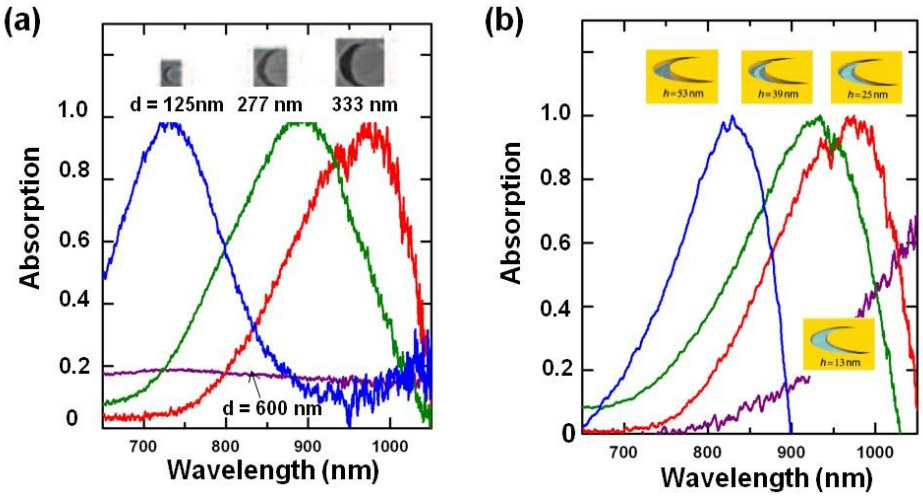

Figure 3.7 Absorption spectra of crescent-shaped nanoholes in infrared regime at C mode resonance. (a) The LSPR peaks red shift with increasing size. (b)The LSPR peaks blue shift with increasing thickness.

3.3.2 LSPR peak shift sensing result

As discussed in Chapter 2.1, the LSPR peak shift resulting from the change of surrounding media of the nanostructure can be written as:

$$\Delta\lambda_{\max} = m\Delta n\left(1-e^{-2d/l_d}\right) \quad \text{.....(2.9)}$$

m is the refractive index sensitivity, and Δn is the change of ambient refractive index. The effective adsorbate layer thickness, d, is fixed by the concentration of the adsorbate under detection. The decay length l_d is related to the material and the shape of the nanoparticles. When immersing the crescent-shaped nanohole samples into homogeneous media such as air or water, the effective adsorbate layer is much larger than l_d, and the amount of peak shift $\Delta\lambda_{max}$ is proportional to Δn (n_{water}-n_{air} = 1.33 - 1 = 0.33), and the refractive index sensitivity is thus calculated.

In Figure 3.8(a), the LSPR peak position of crescent-shaped nanohole substrates with 277 nm in long axis and 25nm Au thickness is 845 nm in air and 903 nm in water. The refractive

index sensitivity is 167 nm / RIU (RIU is one refractive index unit). Comparing to other LSPR substrate such as gold nanoisland and nanoprism substrate, the LSPR sensitivity of crescent-shaped nanohole substrate is superior. For the substrate with circular nanohole array, the sensitivity is reported as 400 nm RIU and the high sensitivity is explained by the interaction of the LSPR inside the nanohole and the propagating surface plasmon resulted from the grating effect of the long range arrayed patterning of the nanoholes. The arrayed crescent-shaped hole is fabricated in order to get higher LSPR sensitivity as in the circular nanohole array. Instead of rectangular array, the crescent-shaped nanoholes array in limited in the hexagonal array due to the closed packed nanosphere template. The crescent-shaped nanohole array is shown is Figure 3.9. However, the measured refractive index sensitivity is 175nm /RIU, pretty closed to the number from the random crescent-shaped nanohole array. The nonachievement of increased sensitivity might resulted to nonperfect array made by drop dry method of make hexagonal array PS nanophere templates. For the arrayed hexagonal circular nanohole array, there is also no high sensitivity as rectangular array. The results match to other literatures and hexagonal array is more complicated when considering the generation of propagating surface plasmon.

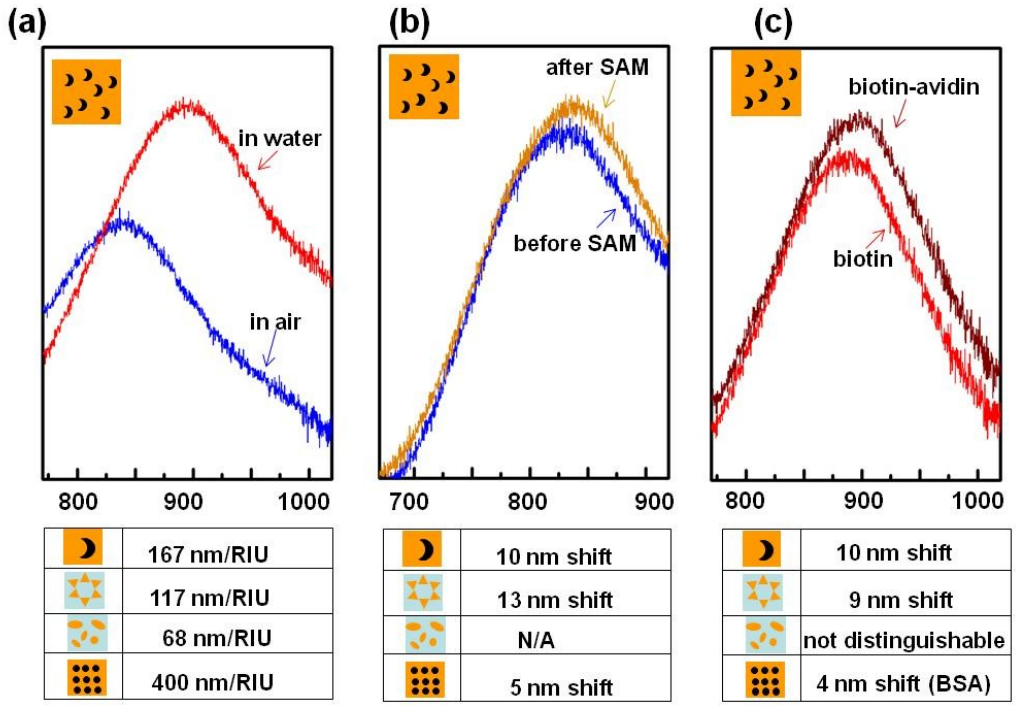

Figure 3.8 LSPR peak shift measurement result of crescent-shaped nanohole substrates with 277 nm diameter and 25 nm gold thickness. (a) the LSPR peaks measured in air and in water (b) LSPR peak before and after surface functionalization of 16-MUA self-assembled monolayer (c) LSPR peaks before and after the avidin molecules bind to the substrates functionalized with biotin monolayer

For LSPR biosensing, the change of the refractive happens at the region very close to the surface due to the molecular binding. In this case, besides the bulk refractive index sensitivity,

m, the electric field decay length, l_d, especially played an important role. l_d is evaluated by functionalized the surface of crescent-shaped nanohole array substrate with alkalinethio, which form a self-assembled monolayer. The LSPR peak position of crescent-shaped nanohole substrate is shown in figure 3.8 (b). There is a 10 nm peak shift after SAM functionalization, and the sensitivity of the local refractive change is good compare to other LSPR sensing substrates. Finally, the LSPR biosensing capability in the solution environment is democstrates by biotin-strepavidin systems. The surface of crescent-shaped nanoholes was functionalized with EZ-link biotin-HPDP. After adding strepavidin solution to the substrate, the LSPR peak were measured real-time to capture the binding process. The LSPR peak shift resulting from the binding events strepavidin to the surface is 10 nm, and the result is also good comparing to other substrates listed in Figure 3.8 (c).

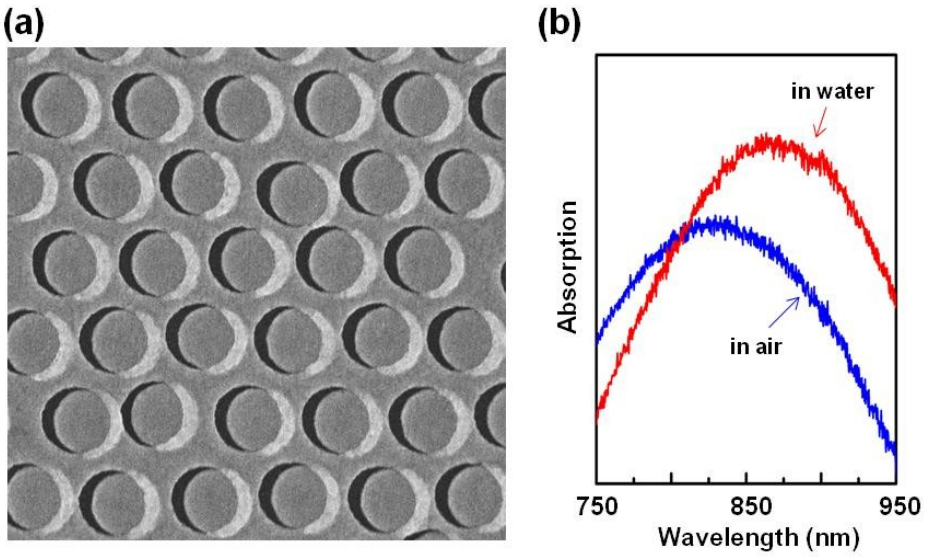

Figure 3.9 LSPR peak shift measurement result of crescent-shaped nanohole array with 277 nm diameter and 25 nm gold thickness. (a) SEM image of crescent-shaped nanoholes patterned in hexagonal array. (b) absorption peak of the substrate in (a) when it is surrounded by air or water.

3.3.3 SERS sensing result

The SERS signal of different concentration of R6G solution from the crescent-shaped nanoholes substrate is shown in Figure 3.10. Some R6G Raman scattering peaks are apparent at 10 nM and clear fingerprint spectrum is present at 10 μM. For the circular nanohole substrate made by the same sized PS nanosphere template, there is only a weak SERS signal shows up at R6G solution of 10 μM. It is concluded that the sharp tip of the crescent-shaped nanohole does play an important role on Raman scattering signal enhancement. By functionalizing the surface of the crescent-shaped nanoholes, either on the gold walls or on the glass bottom with grabbing molecules, the surface binding events could be increased and result in higher SERS signal. Crescent-shaped nanoholes could also be functioned as a nano-reactor due to itscapability to

confine the analytes or reactors. The works regarding SERS application of crescent-shaped nanohole substrates is continuing.

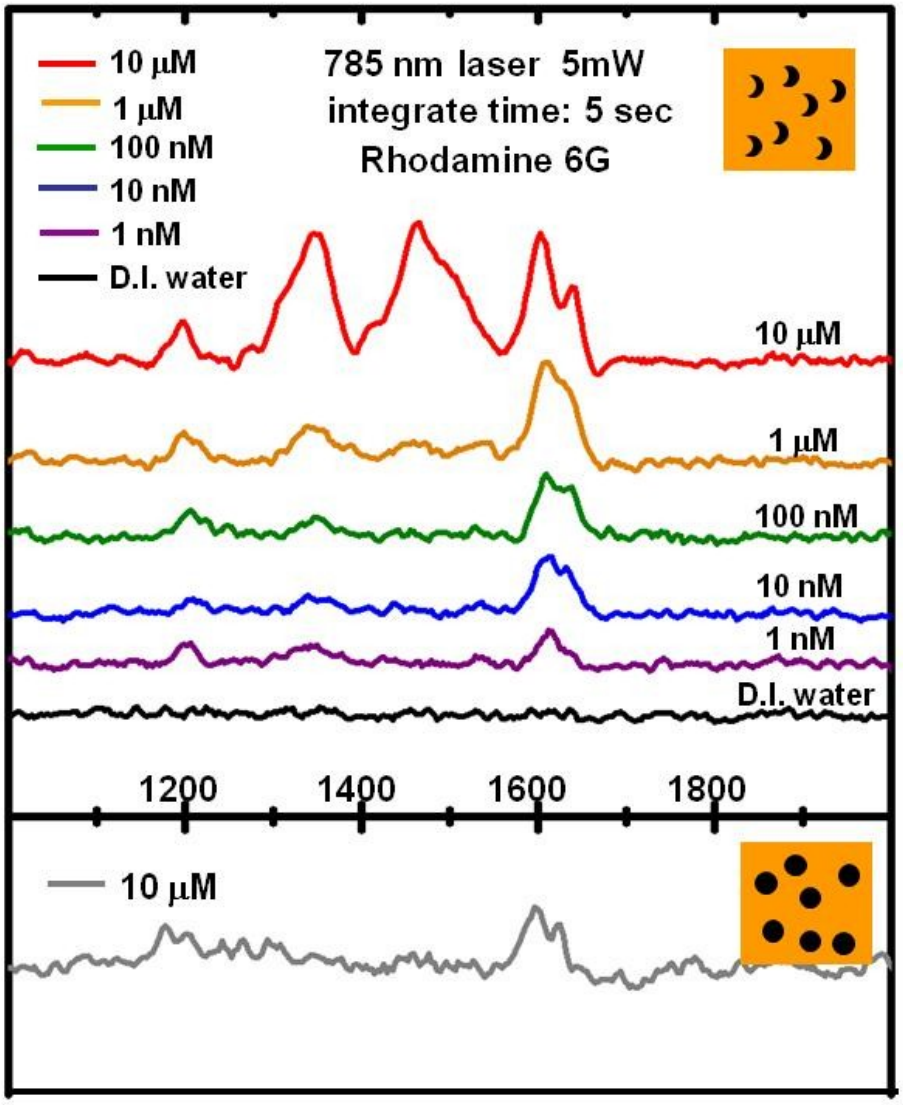

Figure 3.10 SERS measurement result of R6G solution with different concentration on crescent-shaped nanohole substrate (277 nm in diameter, 25 nm gold thickness) and 10 uM R6G solution on circular nanohole substrate.

3.4 Conclusion

Like the positive nanocrescent, we have shown the crescentshaped nanohole can be readily tuned by varying its geometric parameters. However, the crescent-shaped nanohole geometry may offer significant advantages over its positive nanocrescent counterpart. As we have shown, the crescent-shaped nanoholes can be fabricated in large-area arrays with sub-10-nm tips. The tip sharpness exceeds that of positive nanocrescents obtained with the same nanosphere mask and is sharper than rectangular holes, bowtie holes, and double holes that have been fabricated. Such sharp features will be critical in improving molecular sensitivity of hole-based devices. In addition, the hole geometry offers significant advantages over particle-based sensors, including integratability, robustness, and the potential to nanoconfine analyte in hot-spot regions. Both LSPR peak shift and SERS based molecular sensing results are presented, and the sharp tips of crescent-shaped nanoholes do improve the sensitivity comparing to circular nanoholes. In short, the crescent-shaped nanohole may provide the best of both worlds between holebased and particle-based biological and chemical plasmonic sensors.

References:

(1) Ebbesen, T.; Ghaemi, H. F.; Thio, T.; Wolff, P. A. *Nature (London)* **1998**, 391, 667.
(2) Genet, C.; Ebbesen, T. W. *Nature (London)* **2007**, 445, 39.
(3) Coe, J. V.; Heer, J. M.; Teeters-Kennedy, S.; Tian, H.; Rodriguez, K. R. *Annu. ReV. Phys. Chem.* **2008**, 59, 179.
(4) Gordon, R.; Sinton, D.; Kavanagh, K. L.; Brolo, A. G. *Acc. Chem. Res*. **2008**, 41, 1049.
(5) Willets, K.; van Duyne, R. P. *Annu. ReV. Phys. Chem*. **2006**, 58, 267.
(6) Kneipp, K.; Moskovits, M.; Kneipp, H. *Surface-Enhanced Raman Scattering: Physics and Applications*; Springer: Berlin, **2006.**
(7) Fort, E.; Gre´sillon, S. *J. Phys. D* **2008**, 41, 013001.
(8) Liu, G. L.; Long, Y.-T.; Choi, Y.; Kang, T.; Lee, L. P. *Nat. Methods* **2007**, 4, 1015.
(9) Maier, S. A. *Plasmonics: Fundamentals and Applications*; Springer: New York, **2007**.
(10) Sinton, D.; Gordon, R.; Brolo, A. G. *Microfluid. Nanofluid*. **2008**, 4, 107.
(11) Pieczonka, N. P. W.; Aroca, R. F. *Chem. Soc. ReV*. **2008**, 37, 946.
(12) Wu, W.; Dey, D.; Memis, O. G.; Katsnelson, A.; Mohseni, H. *Nanoscale Res. Lett*. **2008**, 3, 351.
(13) Wu, W.; Dey, D.; Memis, O. G.; Katsnelson, A.; Mohseni, H. *Nanoscale Res. Lett*. **2008**, 3, 123.
(14) Henzie, J.; Lee, M. H.; Odom, T. W. Nat. *Nanotechnol*. **2007**, 2, 549.
(15) Kim, J.; Liu, G. L.; Lu, Y.; Lee, L. P. *Opt. Express* **2005**, 13, 8332.
(16) Ross, B. M.; Lee, L. P. *Nanotechnology* **2008**, 19, 275201.
(17) Liu, G. L.; Lu, Y.; Kim, J.; Doll, J. C.; Lee, L. P. *AdV. Mater*. **2005**,17, 2683
(18) Shumaker-Parry, J. S.; Rochholz, H.; Kreiter, M. *AdV. Mater.* **2005**, 17, 2131.
(19) Lu, Y.; Liu, G. L.; Kim, J.; Mejia, Y. X.; Lee, L. P. *Nano Lett*. **2005**, 5, 119.
(20) Rochholz, H.; Bocchio, N.; Kreiter, M. *New J. Phys*. **2007**, 9, 53.
(21) Bukasov, R.; Shumaker-Parry, J. S. *Nano Lett.* **2007**, 7, 1113.
(22) Li, K.; Clime, L.; Cui, B.; Veres, T. *Nanotechnology* **2008**, 19, 145305.
(23) Bocchio, N. L.; Unger, A.; A´ lvarez, M.; Kreiter, M. *J. Phys. Chem.C* **2008**, 112, 14355.
(24) Etchegoin, P. G.; Ru, E. C. L.; Meyer, M. *J. Chem. Phys*. **2006**, 125, 164705.

(25) Johnson, P. B.; Christy, R. W. *Phys. ReV. B* **1972**, 6, 4370.
(26) van der Molen, K. L.; Koerkamp, K. J. K.; Enoch, S.; Segerink, F. B.; van Hulst, N. F.; Kuipers, L. *Phys. ReV. B* **2005**, 72, 045421.
(27) Jin, E. X.; Xu, X. *Appl. Phys. B: Laser Opt.* **2006**, 84, 3.
(28) Lesuffleur, A.; Kumar, L. K. S.; Brolo, A. G.; Kavanagh, K. L.; Gordon, R. *J. Phys. Chem. C* **2007**, 111, 2347.
(29) Shuford, K. L.; Gray, S. K.; Ratner, M. A.; Schatz, G. C. *Chem. Phys. Lett.* **2007**, 435, 123.
(30) Kwak, E.-S.; Henzie, J.; Chang, S.-H.; Gray, S. K.; Schatz, G. C.; Odom, T. W. *Nano Lett.* **2005**, 5, 1963.
(31) Murray, W. A.; Astilean, S.; Barnes, W. L. *Phys. ReV. B* **2004**, 69, 165407.
(32) Park, T.-H.; Mirin, N.; Lassiter, J. B.; Nehl, C. L.; Halas, N. J.; Nordlander, P. *ACS Nano* **2008**, 2, 25.
(33) Prikulis, J.; Hanarp, P.; Olofsson, L.; Sutherland, D.; Ka¨ll, M. *Nano Lett*. **2004,** 4, 1003.
(34) Jackson, J. D. *Classical Electrodynamics*, 3rd ed.; John Wiley & Sons: New York, **1999**.
(35) Zentgraf, T.; Meyrath, T. P.; Seidel, A.; Kaiser, S.; Giessen, H. *Phys. ReV. B* **2007**, 76, 033407.

CHAPTER 4:
BIO-INSPIRED NANOCORALS WITH DECOUPLED CELLULAR TARGETING AND SENSING FUNCTIONALITY

4.1 Introduction

The ability to sense and detect local biomolecular signaling inside and surrounding a living cell may lead to a revolutionary improvement in diagnostic accuracy and therapeutic strategy,[1,2] wherein the molecular components or processes that represent detailed mechanisms of pathologies and treatment responses can be directly investigated. Hence, there is a strong driving force to engineer small probes, ranging from tens to hundreds of nanometers in size, that can be positioned in specified regions inside or surrounding living cells in order to facilitate molecular detection. Most nanoprobes developed for this purpose serve as labels or markers that bind to and report the presence of specific molecules, and their read-out signals are based on the intrinsic properties of the probe, such as the emission of fluorescent molecules, quantum dots, or the scattering of metal nanoparticles.[3–6] In contrast, nanoplasmonic optical antennas (i.e. metal nanoparticles) that enhance molecular spectral information, with techniques such as surface-enhanced Raman spectroscopy (SERS)[7,8] and Plasmonic Resonance Energy Transfer (PRET) [9,10] are promising since the read-out signal is intrinsic to molecules in proximity to the nanoprobe surface. This molecular fingerprint offers the potential for label-free multi-channel read out of local biochemical composition.[11–14]

A key technology in achieving useful cellular nanoprobes is the attachment of ligands to the nanoprobe surface to allow targeting to specific cell types or subcellular regions. While targeted drug delivery[15,16], photothermal therapy [17,18], and MRI contrast enhancement [19,20] have been demonstrated and have large potential for clinical diagnosis and treatment, nanoprobes which can achieve both targeting and label-free sensing (i.e. SERS) have not yet been reported. Achieving both targeting and sensing via SERS in a single nanoprobe is challenging because targeting ligands attached on the surface will impede the SERS detection. Therefore, part of the nanoprobe surface must be kept ligand-free to prevent blocking of the SERS surface, avoid interference of mixed signals, and alternatively to allow conjugation with a different ligand to bind molecules of interest.

Here we present a new type of stand-alone cellular probe called a nanocoral, which combines cellular specific targeting with biomolecular sensing, yet decouples the two functional modes (see Figure 4.1). Analogous to natural sea corals that use rough surfaces to maximize surface area for efficient capture of light and food particles,[21] nanocorals utilize a highly roughened surface at the nanoscale to increase analyte adsorption capacity, and create a high density of SERS hot-spots. In contrast to other SERS cellular nanoprobes, such as nanoshells[22] and nanocrescents[7] composed purely of gold, the polystyrene (PS) hemisphere of the nanocoral can be selectively functionalized with antibodies to target the receptors of specific cells. This functionalization leaves the roughened gold region of the nanocoral clean for SERS measurements. Therefore, the targeting and sensing mechanisms are decoupled, and can be

separately engineered for a particular experiment. In addition, the PS region may also be used as a carrier for drugs or other input chemicals by surface hydrophobic adsorption[23] or encapsulation,[24] making the nanocoral a multifunctional nanosensor.

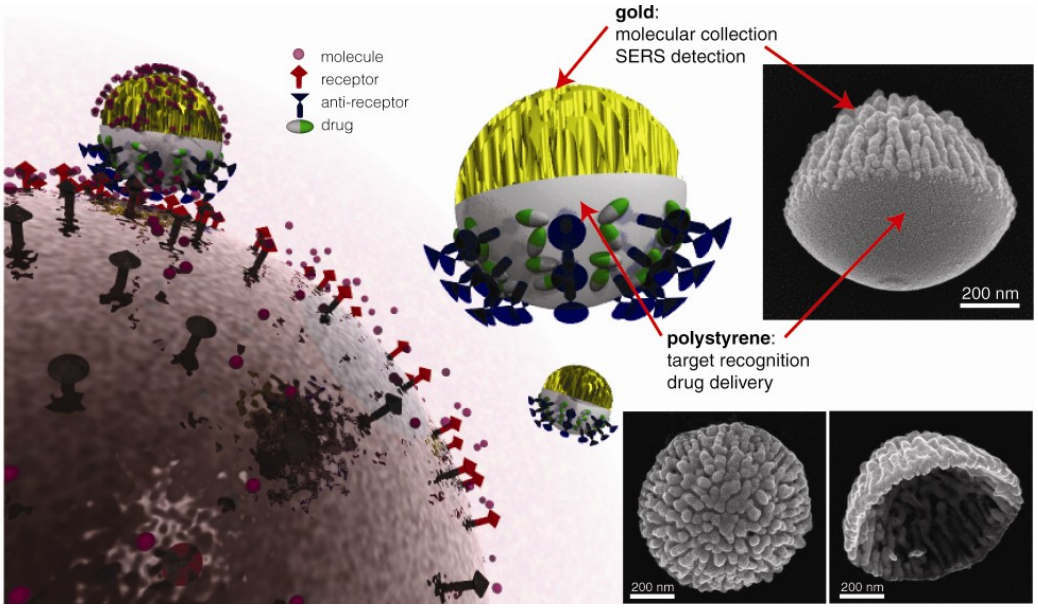

Figure 4.1 Schematic of nanocorals as multifunctional nanoprobes for targeting, sensing and drug delivery; insets show SEM images of fabricated nanocoral probes; the PS template has been etched in the bottom right inset.

The fabrication of the nanocoral array is a simple and cost-effective 3-step process, as illustrated in Figure 4.2. The process starts with the formation of a hexagonal close-packed monolayer of PS nanospheres on a glass substrate by a drop-cast method.[25] The substrate is then loaded into an oxygen plasma etching system, and the plasma etching induces shrinkage of the PS nanospheres as well as deeper trenches on the surface with longer etch times. Gold is then deposited on the PS template to obtain a specific thickness, and the resulting nanocoral array can be directly used for SERS measurements. For applications that require stand-alone probes, the nanocoral array can be released from the surface by sonication (Figure 4.2(d)).

PS nanospheres provide a simple and versatile template for nanostructure fabrication because of their monodisperse size distribution, large range of available particle sizes from several nm to several mm, simplicity of forming self-assembled hexagonal arrays on surfaces, and well-developed chemical processes for etching. A large number of recent substrates, including nanodisks,[26] nanoholes,[27] nanovoids,[28] nanopillars,[29] nanocrescents[30,31] and crescent-shaped nanoholes[32] have been built using nanosphere lithography by using the PS nanospheres as masks for thin film deposition and directional dry etching. Oxygen plasma is a common technique for tailoring the size and interparticle distance of the PS nanospheres, and as the etching process proceeds, the PS nanosphere size decreases while the surface roughness increases. Although the surface roughness of the nanosphere template is usually considered a drawback that limits the range of PS sphere sizes upon etching, here we utilize this etching-

induced roughness as the basic template structure of our nanocorals. Roughness formation during etching has been observed in PS nanospheres during plasma etching,[33] though the causes for surface roughness formation are still not completely understood. We suggest the roughness observed in the nanocorals can be explained by a combination of etchant shadowing and first-order re-emission effects,[34,35] however more study is needed to prove the cause(s) of roughening. The gradual change of the surface roughness of nanocorals during etching is shown in Figure 4.2(e).

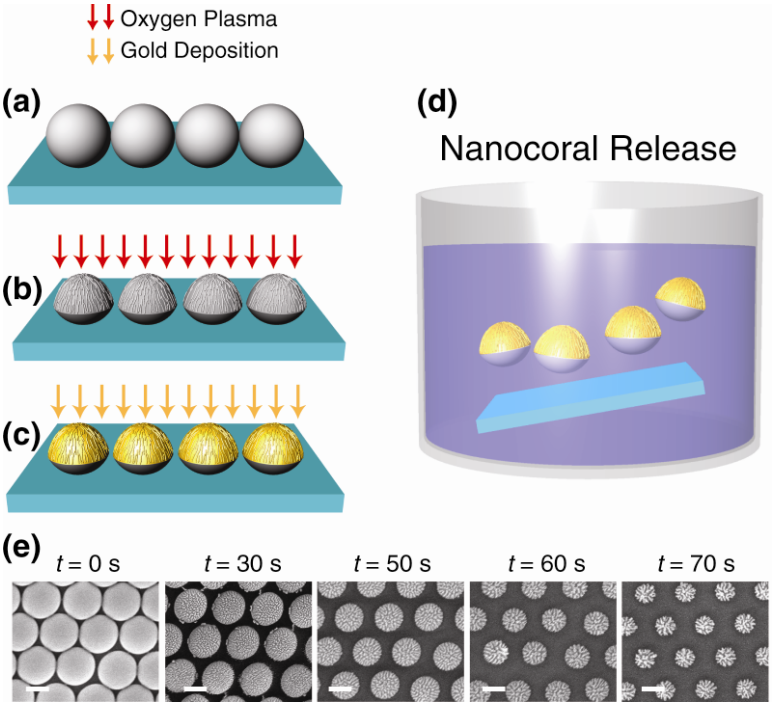

Figure 4.2 Nanocoral fabrication process; (a) self-assembly of PS nanospheres on glass, (b) oxygen plasma etching, (c) gold deposition and (d) release of nanocorals into solution; (e) the gradual etching of the PS template to create the nanocoral template (scale bar = 200 nm)

4. 2 Method

4.2.1 Nanocoral Array Fabrication

The glass substrates (22 mm *x* 22 mm, Fisher Scientific, PA, USA) were cleaned in piranha solution for 10 minutes, then subsequently rinsed with deionized water and dried by nitrogen gas. A mixture (10 μL) of 1:1 methanol and polystyrene nanosphere solution (Polysciences, PA, USA) was dropped onto the glass substrate to form a hexagonal close-packed monolayer of PS nanospheres. The substrate was then loaded into an oxygen plasma etching system (Plasma-Therm PK-12, at 50 sccm, 100 W), and the etching time was adjusted based on the original PS nanosphere size. For example, the PS nanospheres in Figure 1 were etched for 100 seconds to generate nanocorals that were 800 nm in diameter. Gold was then deposited on the PS template (Edwards e-beam evaporator EB3) to obtain a specific thickness, resulting in the nanocoral array. To release the nanocorals, the nanocoral array was immersed in deionized water and sonicated for 5 minutes, after which all nanocorals were released from the surface and suspended in solution.

4.2.2 SERS Characterization:

SERS measurements were taken from nanocorals immersed in known concentrations of R6G solution. We used a 785 nm excitation laser, which is a widely adopted wavelength within the biological window, with a 0.3 mW excitation power. The measurement area was 3 μm by 1 μm, defined by the focused laser spot size and the slit in front of the spectrometer. The SERS measurement was conducted with a 1 mm thick layer of R6G solution on top of the nanocoral substrate; the solution was sandwiched between the substrate and a glass cover slip, with a 1 mm Polydimethylsiloxane (PDMS) spacer.

4.2.3 HER-2 Receptor Targeting

Phosphate buffered saline (PBS) solution (10 μL) containing antibodies (2.5 μg, Anti-HER-2/neu, Becton Dickinson, NJ, USA) was added into nanocoral suspension (10 μL, $3*10^{10}$ nanocorals mL^{-1}). After incubating overnight at 4°C for antibody adsorption onto the PS side of the nanocorals, the mixture was then centrifuged, and the nanocorals were resuspended in PBS (100 μL). The functionalized nanocorals were then loaded onto cultured breast cancer cells (BT474 cell line, ATCC) for 30 minutes at 37°C, followed by washing cells with PBS 1X with sodium azide (0.1%, Sigma-Aldrich, MO, USA) thoroughly to remove the unbound nanocorals. The cells were then dyed with Hoechst 33342 (Sigma-Aldrich, MO, USA) and fixed with paraformaldehyde (1%, Sigma-Aldrich, MO, USA) for imaging. The control was done by functionalizing the nanocorals with isotype antibodies (Mouse Ig Fluorescence Controls, Becton Dickinson, NJ, USA), and repeating the procedure described above. To confirm the Anti-HER-2 functionalized nanocorals do not attach to cells which do not overexpress HER-2, HeLa cells were used following the procedure described above.

4.3 Result and Discussions

4.3.1 Fabrication results of nanocoral array and single nanocorals

The resulted nanocoral substrates are shown in Figure 4.3. For the nanocorals with diameter of 800 nm (Figure 4.3 (a),(b)) and 300 nm (Figure 4.3 (c),(d)), the rough surface patterned on each etched polystyrene template are reproducible. When releasing the nanocorals from the substrates by sonication, the surface pattern and the integrity of are kept as shpwn in figure 4.3 (e)-(h), demonstrating the robustness of the nanostructure. After etching away the PS template, the innerside of nanocoral also carry rough surface feature, make nanocoral a double sided useful nanoprobe.

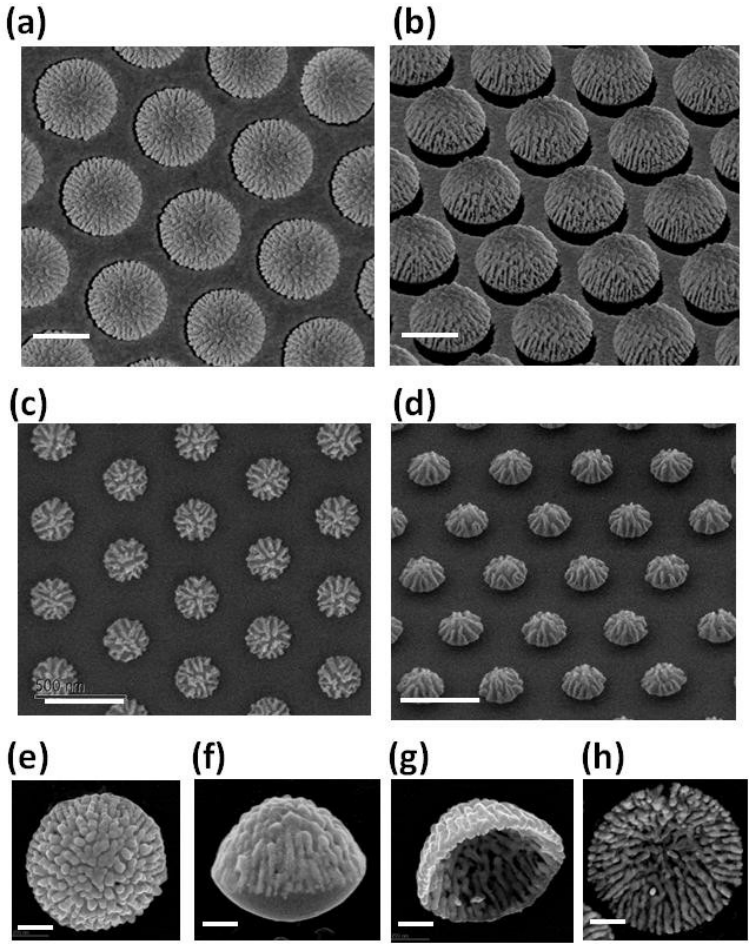

Figure 4.3 SEM images of nanocorals. (a) top view (b) side view of 800 nm nanocoral array. (c) top view (d) side view of 300 nm nanocoral array. (e) top view (b) side view of single nanocoral. (g) (h) after etching away polystyrene template, the innerside of nanocoral also carried rough surface features transferred from the oxygen-plasma etched polystyrene template.

4.3.2 Sensing capability of nanocoral array

We demonstrate the sensing capability of the ultra-rough region of the nanocoral by characterizing the nanocoral array before release into solution (after process step shown in Figure 4.2(c)). In contrast to smooth nanoparticle probes, the high surface area of the nanocoral causes increased adsorption capacity. To demonstrate this effect, we incubated the nanocoral array with Rhodamine 6G (R6G) solution, dried the substrate with nitrogen gas, and measured the fluorescent signal intensity of adsorbed R6G on the nanocoral substrate versus that of a flat gold film. We note that while R6G is not a biomolecule and would likely not be used for sensing in a cellular environment, it is a common molecule used to characterize SERS and fluorescence, and hence allows a comparison of nanocorals with previous and future substrates. As shown in the inset to Figure 4.4 (a), the nanocoral region has significantly higher fluorescence intensity than the flat gold surface: the arrayed nanocorals adsorb 50 times higher fluorescent intensity per unit area than the flat gold surface (see Figure 4.5). The increase in fluorescent signal is at least partially due to increased adsorption of R6G on the nanocoral substrate; however, we cannot rule out surface enhanced fluorescence due to hot-spots or quenching on the gold surface contributing to the observed signal as well.[36] We note the higher fluorescence intensity from the nanocoral array is not attributed to surface enhanced fluorescence due to localized surface plasmon resonance (LSPR) of the nanocoral, since there is no overlapping of the LSPR of the nanocoral substrate (Figure 4.6(a) blue curve) with the adsorption/emission spectra of R6G (530 nm/570 nm).

We then performed SERS measurement of the nanocoral array to characterize the utility of the rough region of the nanocoral as a SERS sensor. We observe a limit of detection of approximately 10 nM of R6G (Figure. 3(b)) due to the roughness of the nanocoral surface. The analytical enhancement factor (EF) of nanocoral is 6.5 x 10^7 (EF=[$I_{SERS\ signal}$ (at λ=867 nm) / $I_{Raman\ signal}$ (at λ=867 nm)] x ([C]$_{Raman}$/[C] $_{SERS}$). Importantly, we find the SERS intensity does not fluctuate significantly across different regions of the sample (see Figure 4.7), which is in stark contrast to many previously reported roughened SERS substrates. Across a nanocoral substrate, the standard deviation in SERS signal was found to be 7% (n = 100); this finding emphasizes the reproducibility of the oxygen plasma roughening method. We note that while local hot-spots (which lead to SERS) are likely to vary in intensity at different locations, the distribution of these hot-spots over a nanocoral produces a uniform signal. To further characterize the SERS signal from single nanocorals, we fabricated sparsely distributed nanocorals on the glass substrate, allowing us to focus on a single nanocoral. The single nanocoral exhibits consistent SERS results to those of the nanocoral arrays: some R6G peaks are apparent at 10 nM and clear fingerprint spectrum is present at 10 μM (see Figure 4.8). We note that the SERS sensitivity can be greatly improved by tagging the gold surface and other preconcentration techniques, and this will be an area of future focus.

While retaining the same PS template, the Raman signal enhancement capability of the nanocorals can be tuned by the thickness of gold deposition. We speculate that as the gold coats the PS template, the trenches become narrower, resulting in sub-10 nm gaps between the adjacent ridges (Figure 4.4(d), TEM image). We hypothesize that these sub-10 nm gaps are the primary cause of the good SERS signal from the nanocorals. This hypothesis is supported by the thickness dependence of the SERS signal shown in Figure 4.4(e): the signal increases as thickness increases up to approximately 63 nm, resulting in narrower nanogaps on the surface. Further gold thickness begins to fill the trenches and reduces SERS signal.

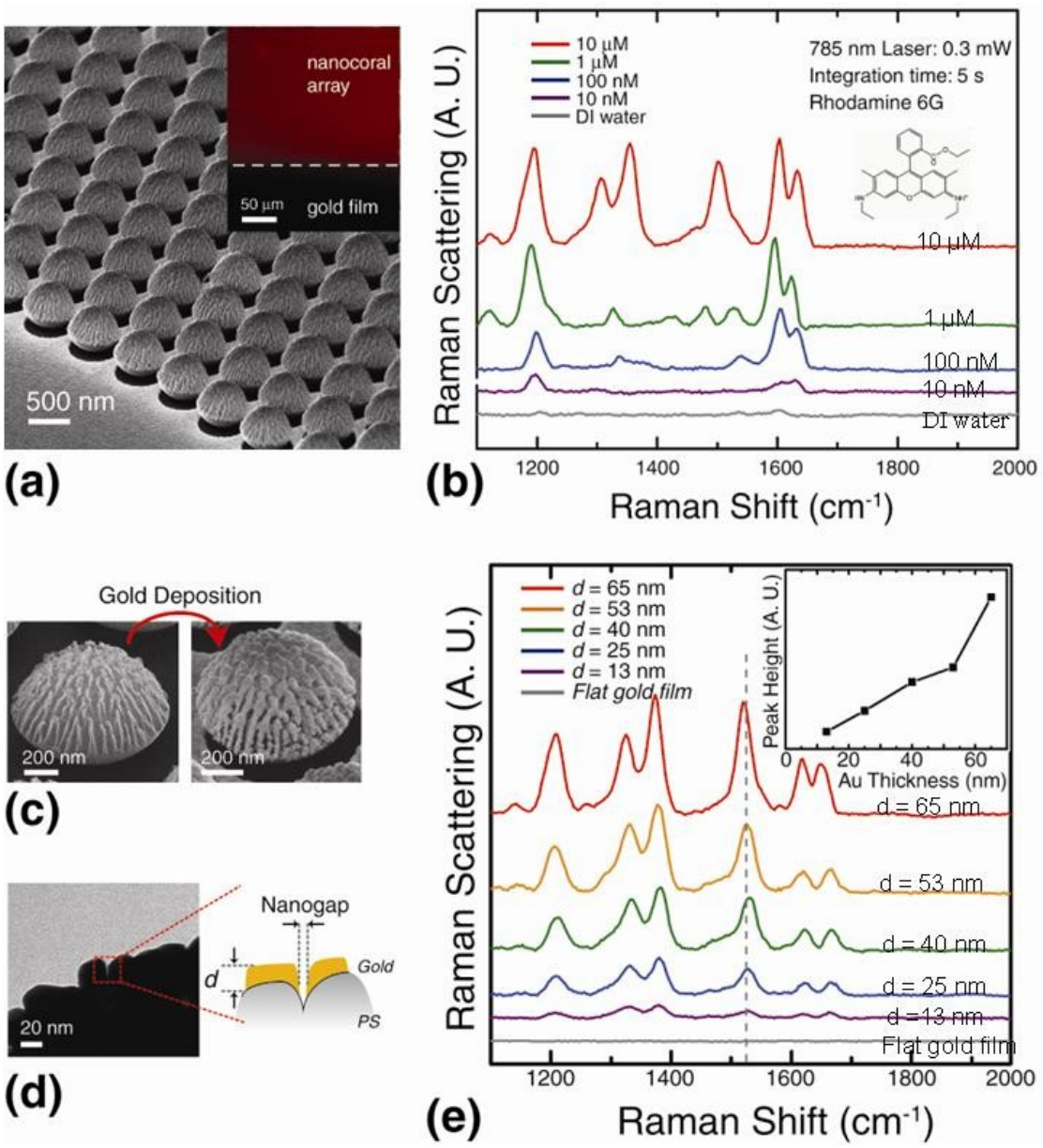

Figure 4.4 SERS signal from nanocorals; (a) SEM images of a nanocoral array; inset shows R6G fluorescent intensity from the nanocoral array and flat gold film; (b) SERS spectra for varying R6G concentration from nanocoral array substrate with 800 nm PS template and 53 nm gold coating; (c) SEM images of nanocorals before and after gold deposition, (d) representative TEM image of sub-10 nm nanocoral nanogap and (e) SERS spectra for nanocorals with different gold thickness (R6G concentration 10 μM).

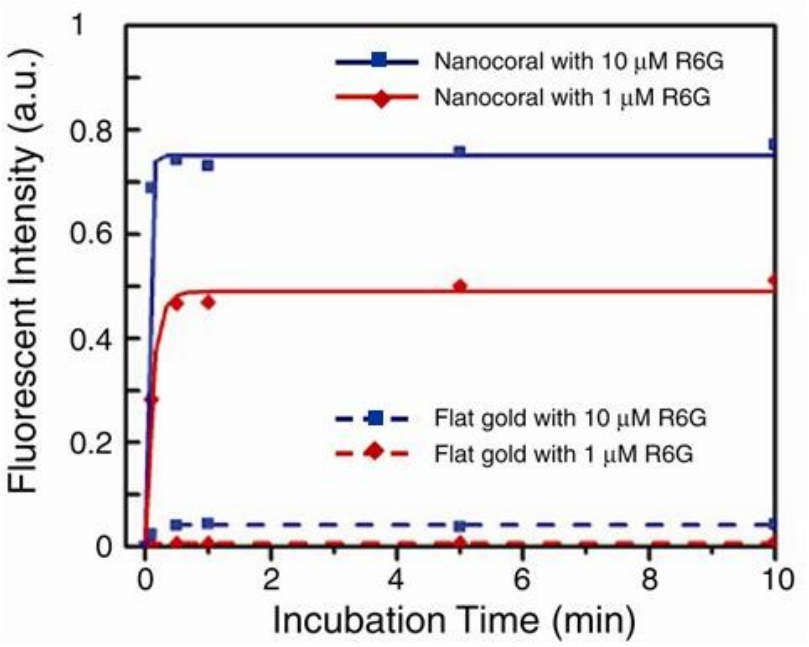

Figure 4.5 R6G molecular adsorption on nanocoral array; by incubating nanocoral arrays and flat gold substrates with 1 μM and 10 μM R6G solution, followed by water cleaning and nitrogen drying, we compared the fluorescent intensity from the nanocoral (300 nm in diameter) and flat gold substrates. In the case of 1 μM R6G incubation, the equilibrium fluorescent intensity from the nanocoral array (red line) is 53 times larger than the flat gold substrates (red dashed line).

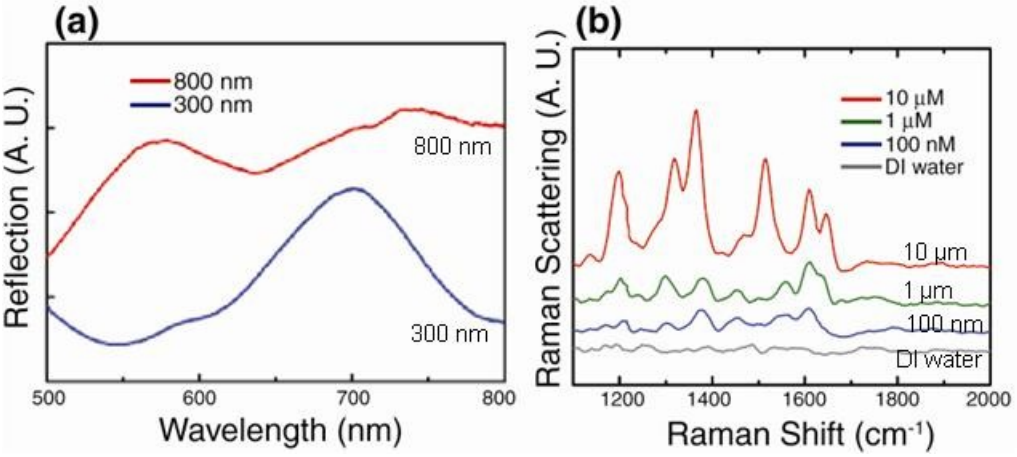

Figure 4.6. SERS from single nanocoral; (a) SERS signal from single nanocoral (800 nm PS template, 53 nm gold) with different R6G concentration, Raman measurement conditions: 785 nm laser at 0.3 mW, 40X objective lens, and 20 sec integration time. We note that small peaks observed for DI water, which are coincidentally near the R6G peaks, are likely caused by the by-product of oxygen plasma-etched polystyrene. (b) SERS signal from the nanocoral and the smooth nanosphere with 53 nm gold coating; (scale bar = 200 nm, R6G concentration = 100 μM, same Raman measurement conditions as (a) with 5 sec integration time).

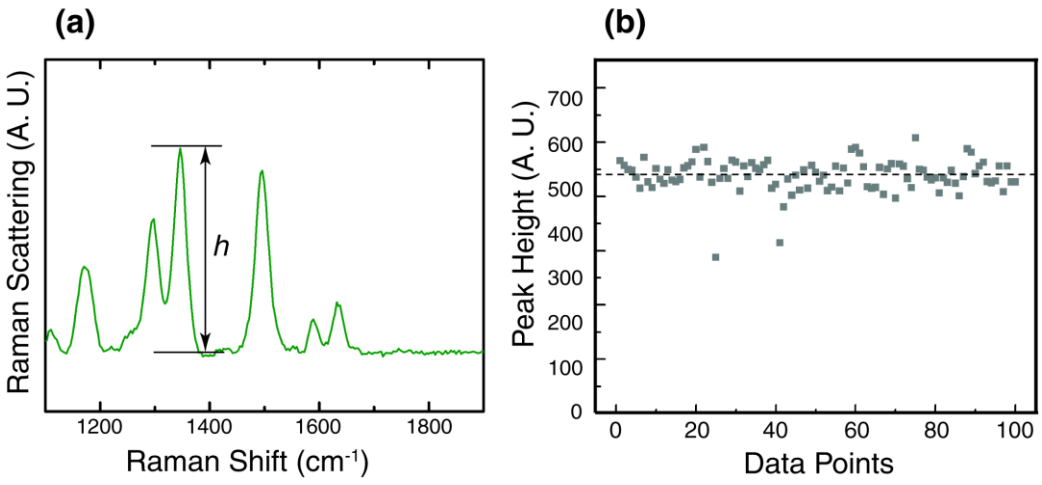

Figure 4.7 SERS signal uniformity test of the nanocoral array substrate with 800 nm PS template and 53 nm gold coating (the same sample as in Figure 3); (a) a representative SERS spectrum for 10 μM R6G solution; (b) the scattering plot of peak height at 1360 cm^{-1} (h marked in (a)) for 100 data points. The standard deviation is 7%, which is in stark contrast to many previous roughened SERS substrates.

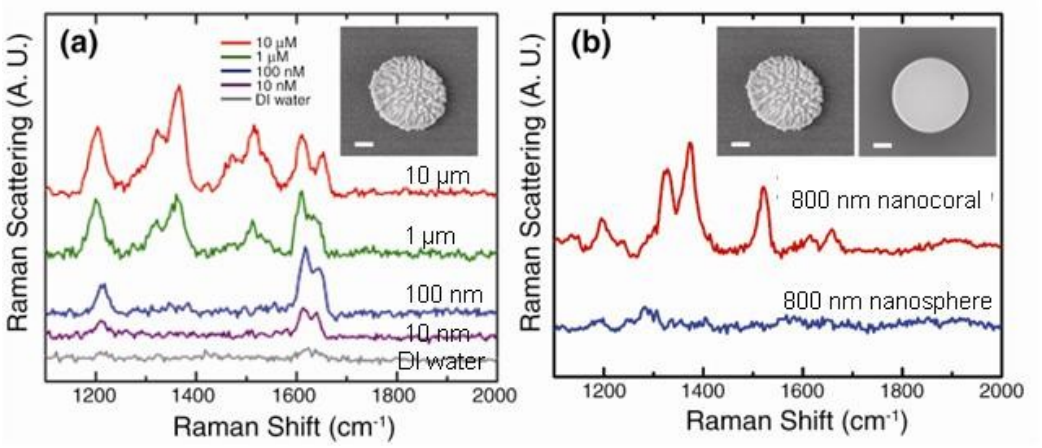

Figure 4.8 SERS from single nanocoral; (a) SERS signal from single nanocoral (800 nm PS template, 53 nm gold) with different R6G concentration, Raman measurement conditions: 785 nm laser at 0.3 mW, 40X objective lens, and 20 sec integration time. We note that small peaks observed for DI water, which are coincidentally near the R6G peaks, are likely caused by the by-product of oxygen plasma-etched polystyrene. (b) SERS signal from the nanocoral and the smooth nanosphere with 53 nm gold coating; (scale bar = 200 nm, R6G concentration = 100 μM, same Raman measurement conditions as (a) with 5 sec integration time).

4.3.3 Targeting the receptors on cancer cell membrane

Having characterized the sensitivity and uniformity of the roughened gold region of the nanocoral, we next demonstrate the targeting function of the PS region. While the gold coated surface of the nanocorals can be used for SERS detection, the PS template of the nanocorals can simultaneously be used to adsorb antibodies or other biological ligands based on hydrophobic attraction, which is widely used for immunological assays.[23] This targeting is demonstrated in Figure 4.9, where by incubating nanocoral suspensions with anti-HER-2 antibodies, we are able to specifically target breast cancer cells (BT474 cell line, ATCC). These cells overexpress Human Epidermal growth factor Receptor 2 (HER-2), which is a well known target for cancer treatment. Figure 4.9(a) shows a phase contrast image of anti-HER-2 functionalized nanocorals attached to the surface of BT474 breast cancer cells. To verify the location of the nanocorals, a fluorescent PS nanosphere was used as the PS template, and these nanocorals can be clearly seen on the cell surfaces in Figure 4.9(b) (Hoechst 33342 dyed cell nucleus in blue). Control experiments (Figure. 4.9(d-i)) show nanocorals do not attach to the cell surface when nanocorals are functionalized with isotype antibodies, or when cells which do not overexpress HER-2 are used. The HER-2 receptor is known to have a fast recycling rate and therefore we expect the receptor-mediated endocytosis of nanocorals will allow for intracellular imaging.[37] By targeting other slowly recycled cancer markers such as epidermal growth factor receptor (EGFR),[6] we expect nanocorals can be designed to stay on the cell membrane for longer times. We emphasize that the ultimate goal of the nanocoral probes would not be to sense HER-2, but instead to use the SERS portion of the probe for multiplexed local detection of biomolecules. In future work, we plan to combine the specific attachment of the functionalized PS region and the high SERS signal from the roughened gold of the nanocorals to create a molecular map of biomolecules at the cell surface. We confirm that antibody attachment is primarily on the PS surface, leaving the gold surface clean for SERS measurements (see Figure 4.10).

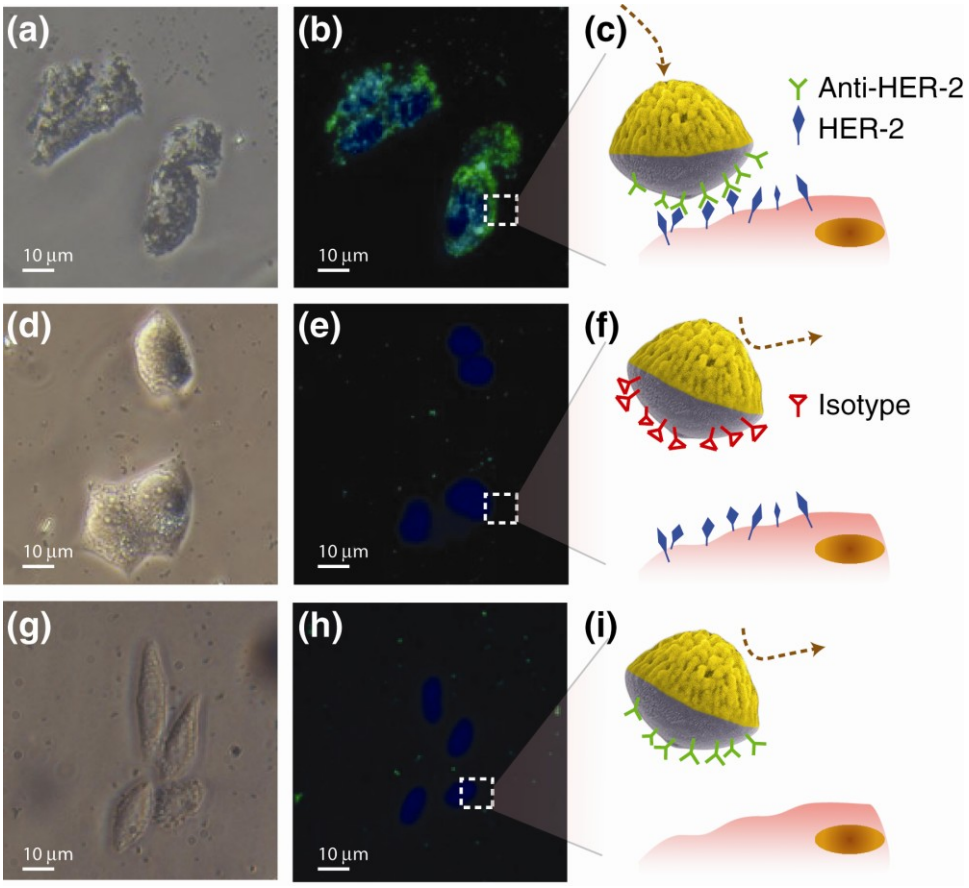

Figure 4.9 Nanocorals as multifunctional probes for living cells; (a) bright field, (b) fluorescent, and (c) schematic images of 300 nm nanocorals attached to BT474 cell surfaces with HER-2/anti-HER-2 binding; fluorescent PS nanospheres are used as the nanocoral template; (d) bright field, (e) fluorescent, and (f) schematic images for a control experiment where PS is functionalized with isotype antibodies, and very few nanocorals bind to the cells; (g) bright field, (h) fluorescent, and (i) schematic images for a control experiment for HeLa cells with PS functionalized with anti-HER-2, and very few nanocorals bind to the cells.

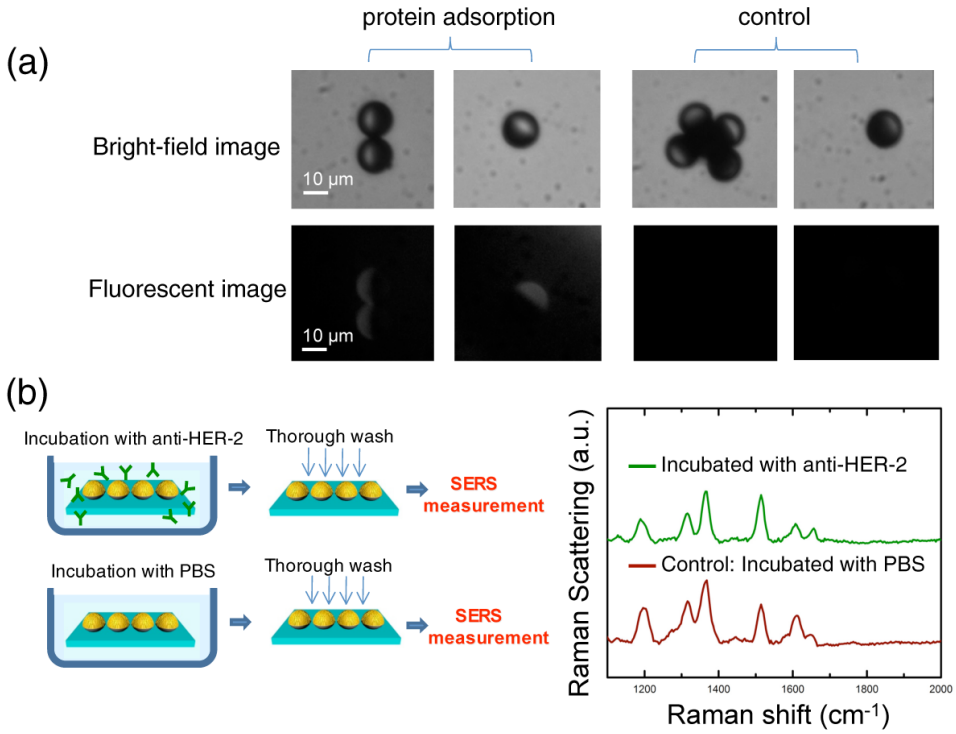

Figure 4.10 Verification of selective attachment of antibody on PS surface; (a) large nanocorals (10 μm) were fabricated and incubated with FITC-tagged BSA solution at 4^{o}C overnight, followed by thorough washing in PBS; the fluorescent image demonstrates the selection adsorption of the protein on the PS surface due to hydrophobic adsorption; (b) to further verify that the gold surface remains clean for SERS detection, 300 nm nanocoral arrays are incubated with HER-2 antibody for 24 hours at 4^{o}C, following by washing, and SERS measurement of R6G (with the same conditions as Figure 3). The control is conducted by incubating the nanocoral substrate with PBS for the same incubation, washing, and SERS steps. The nearly identical SERS signals indicate the HER-2 antibody has not adsorbed on the gold surface at any concentration significant enough to affect the SERS detection of R6G.

4.3.4 The versatility of the nanosphere fabrication and other potential applications of nanocorals

The versatility of the nanosphere fabrication process allows nanocorals to be fabricated over a wide range of sizes for different applications. In Figure 4.11, PS sphere templates for nanocorals with diameters 100 nm, 200 nm, 300 nm, 500 nm, and 800 nm are shown. The rough surface pattern of each nanocoral is observed to be very similar regardless of the PS template size, again supporting the reproducibility of the oxygen plasma roughening technique. In the case of 800 nm nanocoral, hot-spots on the roughened surface dominate the Raman signal enhancement. This is confirmed by comparing the SERS signal from single 800 nm nanocorals and single 800 nm PS nanospheres covered with the same gold film thickness: we observe no SERS signal for the smooth gold-coated spheres, while a strong signal is seen for the nanocorals (see Figure 4.8(b)). While there is potential to use the LSPR of the entire nanocoral structure to improve the SERS signal, we find the surface roughness features are dominant. For example, the SERS sensitivity of 300 nm nanocorals are not superior to 800 nm nanocorals, despite a clear

LSPR spectral peak near 700 nm (see Figure 4.6). However, further fine-tuning of the size and thickness of smaller nanocorals to optimize both shell LSPR and surface hot-spots may lead to better enhancement capabilities.

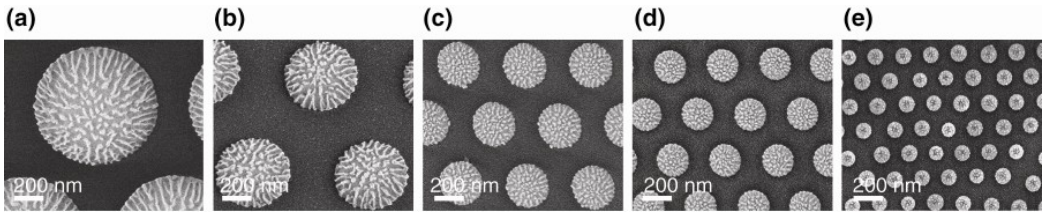

Figure 4.11 Scalability of nanocoral fabrication; SEM images of the roughened PS template of (a) 800 nm, (b) 500 nm, (c) 300 nm, (d) 200 nm, and (e) 100 nm.

4.4 Conclusion

In conclusion, we have demonstrated nanocorals as simple and cost-effective nanoprobes with dual targeting and sensing functionality. The highly roughened gold region of the nanocoral can adsorb more R6G than a flat gold surface, and has a SERS limit of detection of 10 nM R6G with high reproducibility. After release from the substrate and functionalization of the PS region with antibodies, nanocorals attach specifically to breast cancer cells. We have shown the scalability of the nanocorals from 100 nm to 800 nm. Because the nanocoral fabrication technique presented here uses a PS template to create the roughened features, it is not limited to gold. Any material that can be evaporated can be deposited on the PS template, offering this method not just to other plasmonic metals, but other materials that may be of interest for chemical sensors or catalytic converters. In addition, fluorescent markers, drugs, or other chemicals may be embedded in the PS template region to add increased functionality to the nanocoral probes.

References

(1) Alivisatos, P. *Nat. Biotechnol*. **2004**, 22, 47.
(2) Wickline, S. A.; Lanza, G. M.; *Circulation* **2003**, 107, 1092.
(3) Chan, W. C. W.; Nie, S. *Science* **199**8, 281, 2016.
(4) Bruchez, M.; Moronne, M.; Gin, P.; Weiss, S.; Alivisatos, A. P. *Science* **1998**, 281, 2013.
(5) Jain, P. K.; El-Sayed, I. H.; El-Sayed, M. A. *Nanotoday* **2007**, 2, 18.
(6) El-Sayed, I. H.; Huang, X.; El-Sayed, M. A. *Nano Lett.* **2005**, 5, 829.
(7) Lu, Y.; Liu, G. L.; Kim, J.; Mejia, Y. X.; Lee, L. P. *Nano Lett*. **2005**, 5, 119.
(8) Liu, G. L.; Lee, L. P. *Appl. Phys. Lett*. **2005**, 87, 074101.
(9) Liu, G. L.; Long, Y. T.; Choi, Y.; Kang, T.; Lee, L. P. *Nat Methods* **2007**, 4, 1015.
(10) Choi, Y.; Park, Y.; Kang, T.; Lee, L. P. *Nat. Nanotechnol*. **2009**, 4, 742.
(11) Kneipp, K.; Haka, A. S.; Kneipp, H.; Badizadegan, K.; Yoshizawa, N.; Boone, C.; Shafer-Peltier, K. E.; Motz, J. T.; Dasari, R. R.; Feld, M. S. *Appl. Spectrosc*. **2002**, 56, 150.
(12) Qian, X.; Peng, X.; Ansari D. O.; Yin-Goen, Q.; Chen, G. Z.; Shin, D. M.; Yang, L.; Young, A. N.; Wang, M. D.; Nie, S.*Nat. Biotechnol*. **2008**, 26, 83.
(13) Nabiev, I. R.; Morjani, H.; Manfait, M. *Eur. Biophys. J.* **1991**, 19, 311.
(14) Choi, Y.; Kang, T.; Lee, L. P. *Nano Lett.* **2009**, 9, 85.
(15) Yang, P.; Sun, X.; Chiu, J.; Sun, H.; He, Q. *Bioconjugate Chem*. **2005**, 16, 494.
(16) Kohler, N.; Sun, C.; Wang, J.; Zhang, M. *Langmuir* **2005**, 21, 8858.
(17) El-Sayed, I. H.; Huang, X.; El-Sayed, M. A. *Cancer Lett*. **2006**, 239, 129.
(18) O'Neal, D. P.; Hirsch, L. R.; Halas, N. J.; Payne, J. D.; West, J. L. *Cancer Lett*. **2004**, 209, 171.
(19) Veiseh, O.; Sun, C.; Gunn, J.; Kohler, N.; Gabikian, P.; Lee, D.; Bhattarai, N.; Ellenbogen, R.; Sze, R.; Hallahan, A.; Olson, J.; Zhang, M. *Nano Lett*. **2005**, 5, 1003.
(20) Kircher, M. F.; Mahmood, U.; King, R. S.; Weissleder, R.; Josephson, L. *Cancer Res*. **2003**, 63, 8122.
(21) Naumann, M. S.; Niggl, W.; Laforsch, C.;Glaser, C.; Wild, C. *Coral Reefs* **2009**, 109, 3012.
(22) Jackson, J. B.; Halas, N. J. *Proc. Nat. Acad. Sci*. **2004**, 101, 17930.
(23) Cantarero, L. A.; Butler, J. E.; Osborne, J. W. *Anal. Biochem*. **1980**, 105, 375.
(24) Im, S. H.; Jeong, U.; Xia, Y. *Nat. Mater*. **2005**, 4, 671.

(25) Haynes, C. L.; Van Duyne, R. P. *J. Phys. Chem. B* **2001**, 105, 5599.
(26) Hanarp, P.; Käll, M.; Sutherland, D. S. *J. Phys. Chem. B* **2003**, 107, 5768.
(27) Prikulis, J.; Hanarp, P.; Olofsson, L.; Sutherland, D.; Käll, M. *Nano Lett.* **2004**, 4, 1003.
(28) Teperik, T. V.; Popov, V. V. *Opt. Express* **2006**, 14, 1965.
(29) Cheung, C. L.; Nikolic, R. J.; Reinhardt, C. E.; Wang, T. F. *Nanotechnology* **2006**, 17, 1339.
(30) Rochholz, H.; Bocchio, N.; Kreiter, M. *New J. Phys*. **2007**, 9, 1.
(31) Ross, B. M.; Lee, L. P. *Nanotechnology* **2008**, 19, 275201.
(32) Wu, L. Y.; Ross, B. M.; Lee, L. P. *Nano Lett.* **2009**, 9, 1956.
(33) Haginoya, C.; Ishibashi, M.; Koike, K. *New J. Phys*. **1997**, 71, 2934.
(34) Drotar, J. T.; Zhao, Y. P.; Lu, T. M.; Wang, G. C. *Phys. Rev. B* **2000**, 62, 2118.
(35) Drotar, J. T.; Zhao, Y. P.; Lu, T. M.; Wang, G. C., *Phys. Rev. B* **2000**, 61, 3012.
(36) Fort, E.; Grésillon, S. *J. Phys. D* **2008**, 41, 013001.
(37) Wuang, S. C.; Neoh, K. G.; Kang, E.; Pack, D. W.; Leckband, D. E. *Biomaterials* **2008**, 14, 2270.

CHAPTER 5:
LONG-TERM CYTOTOXIC DRUG ASSAY VIA SINGLE-CELL MICROFLUIDIC ARRAY

5.1 Introduction

Different cells have unpredictable and heterogeneous behaviors amongst a population.[1-2] There is much interest in quantifying the range of biological responses of individual cells to various physiologically-relevant stimuli as opposed to bulk averages.[3-4] One important example is that under the same dose of anticancer drugs, what will the distribution of cancer cells' response be after they are exposed to the cytotoxic drugs? The portion of the cells that shows drug resistance should be evaluated and specifically analyzed. If we are able to keep our eyes on each single cell during and after the drug exposure, recording their behavior in response to the drug, this information can be very helpful for drug development.

Most of the cell-based cytotoxic drug assays are done on a bulk of cells.[5-8] Multi-well plates are the most common tool that include more than a million cells for each drug testing conditions. The read out of the cell behavior or change of proteomic composition reflected the whole group of the cells and the complicated cell-cell communication effects are not able to be decoupled. Single cell analysis has been researched these years, while this is a low throughput process where only a few of the single cells able to be observed under the stimuli.

In this chapter, single-cell microfluidic arrays for long-term cytotoxic drug assays are reported. Hydrodynamic single cell trapping technology has been developed earlier in ourlab [9,10], by integrated with perfusion culture technology, long-term single cell cultures for both adherent and suspension cells were demonstrated.[11] This technique allows dynamic microfluidic control of perfusion with uniform environments for individual cells. Here, I further demonstrated the long-term cell culture and drug assay in the single cell trapping device.

The single cell drug assay system is shown in Figure 5.1. In each cell culture chamber formed by the PDMS device, there are arrayed U-shape trap for each single cell. The platform provides a precise and uniform microenvironment for each arrayed individual cell, and the cell-cell interaction effects were decoupled, allowing the research on the cells' behaviors purely due to the drug. The multi-dose profiles can be switched by the perfusion system to mimic in-vivo like dose condition, and most important of all, after the drug exposure, the temporal behavior of the cells can be traced at a single cell resolution for days by taking time-lapse images.

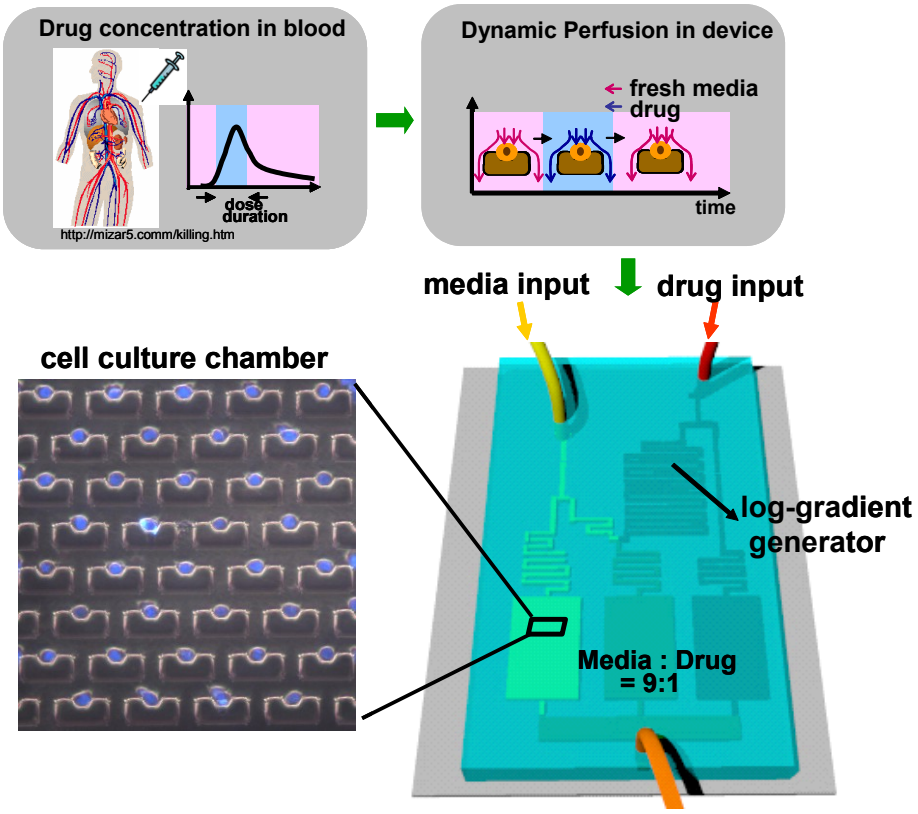

Figure 5.1 Microfluidic single cell array for long-term cytotoxic drug assay. The platform provides precise and uniform microenvironment for each arrayed individual cells, and the cell-cell interaction effect was decoupled and allowed the research of the cells' behaviors purely due to the drug. The multi-dose profiles can be switched by the perfusion system to mimic the in-vivo like dose condition, and after the drug exposure, the temporal behavior of the cells can be traced at a single cell resolution for days by taking the time-lapse images.

The anticancer drug we used in this project is Paclitaxel (Taxol).[12] Taxol binds microtubules and results in suppression of microtubule assembly dynamics.[13] Under this treatment, the cells are prone to be arrested at mitotic phase of the cell cycle, and end with cell death. However, detailed biochemical events downstream of Taxol binding to microtubules are still unknown. One interesting finding is that the Taxol induced cell apoptosis depends on both drug concentration and exposure time. Although several experiment done by the bulk cell assay were reported and the model of apoptosis under different drug treatment is proposed, the temporal behavior of the single cells has never be investigated because of the lack of the proper tools. More importantly, the fate of each individual cell hasn't been researched in detail while the distribution of the dynamic response of the cells might give a big clue to optimize the treatment. Here, by using Taxol as an example, we will demonstrate the capability of our device for information rich assay regarding to the real-time cell behavior amidst the exposure to different drug profile.

As the result that will be discussed later in this chapter, the long term single cell drug assay system works well and this device is one of the systems we developed for future integration with the secretion protein detection sensors for single cell drug assayed based secretion researches.

5.2 Methods for Long-term Single Cell Drug Assay

For demonstration of long-term cytotoxic drug assay, HeLa cells were due to their specific response to the anti-cancer drug, Taxol. Two other adherent cell lines, MCF-7 and CHO cells were also used for testing the versalitity of the long-term single cell culture. One human promyelocytic line, HL-60 cells, were used to demonstrate the drug assay for non-adherent cells. For cell loading, the adherent cells in the culture dishes were treated with 5 mL Trypsin EDTA (0.25 %, Gibco, Carlsbad, CA) to detach the cells and then specific amount of cell culture media was added to form the cell suspension with the cell density of 10^6 ml^{-1}. For non-adherent HL-60 cell lines, the cell suspension is directly used for loading. To get the good single cell loading efficiency, a key experimental detail is to triturate the cell suspension well to make sure the cells are well-separated. Freshly suspended cells are introduced into devices by a 0.15 inch wide tubing that is connected to the syringe at one end and the inlet of the microfluidic device at the other. After the cells begin to enter the device, the fresh media perfusion at the 40 μL min^{-1} setting of the syringe pump is used to wash out the excess cells. The single cell trapping efficiency is around 95% and can be done within two minutes. After the cell loading, the perfusion rate of the fresh media is decreased to 0.5 μL min^{-1} for cell culture. The previous steps were all done within a bio-safety hood to reduce the likelihood of contamination. The single cell culture devices were then either maintained in an incubator between imaging, or heated at 37 °C on a microscope stage for time-lapse imaging experiments (see Figure 5.2 for experiment setup of real time cell growth monitoring).

After 24-hour culture, when most of the Hela cells well spread in the device, we started to introduce anticancer drug, Taxol (Sigma Aldrich), at different concentration for certain dose duration before switching back to fresh media. The two dose profiles we designed are: a) 10 μM for 2 hours and a switch back to fresh media perfusion, and (b) 100nM Taxol for 2 days and a switch back to fresh media. In the whole process before, during and after drug dose, the single cells were monitored in real-time and the timing of apoptosis and division of each single cells was recorded. The HL-60 Taxol drug assay was done after 24 hours of cell loading with 10 μM dose concentration for 2 hours followed by the switch back to fresh media perfusion

For time-lapse experiments an Olympus MIC-D microscope was outfitted with a heated stage to maintain the temperature at 37^{o}C. Time-lapse images were collected using the provided MIC-D software every 3 to 6 minutes. Images were analyzed to determine morphology and cell division using IrfanView. Cells were identified as apoptotic if the blebbing started to show and the dividing event was counted if it retracted from adherent morphology, became spherical and then separated into two daughter cells.

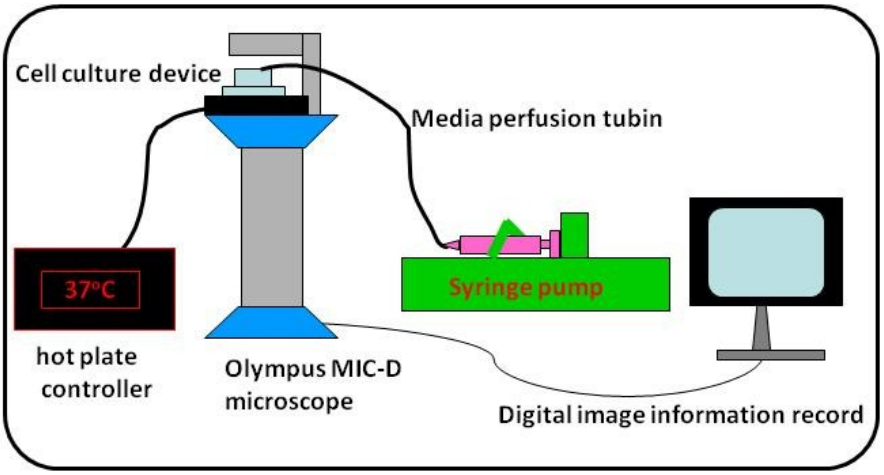

Figure 5.2 A schematic of long-term real-time cytotoxic drug assay monitoring system setup. An Olympus MIC-D microscope was outfitted with a heated stage to maintain the cell culture temperature at 37^0C as well as continuous media perfusion to the cells. Time-lapse images were collected using the provided MIC-D software every 3 to 6 minutes.

5.3 Result and Discussion

5.3.1 Single cell culture for different cell lines

Single cell culture of HeLa cells for 24 hours was previously demonstrated and analysized[11] (see Figure 5.3(a)). Single cell culture results of other three cell lines: MCF-7, CHO and HL-60 were listed in Figure 5.3(b)-(d). In Figure 5.3(a), HeLa cells were well spread close to the cell traps with several cell division events happening during the first 24 hours after cell loading. MCF-7 cells were prone to adhere to each other once they came in contact with each other as shown in Figure 5.3(b), and this observation is the incipient of the idea about tumor spheroid culture that will be discussed later in Chapter 6. CHO cells in Figure 5.3(c) are smaller than HeLa or MCF-7 cells, so the cells relatively easily to escape from the trap and result in a pretty empty cell distribution after 24 hours. The HL-60 cell culture result is shown in Figure 5.3(d). Since HL-60 is a non-adherent cell type, they are relatively easily washed out off the traps. In the time-lapsed movie, some HL-60 single cells showed amoeba-like movement with a growing size. No division events of HL-60 cells were captured during 24-hour culture. The impact of the stress or contact force of the trap structure on HL-60 cell growth needs further investigation.

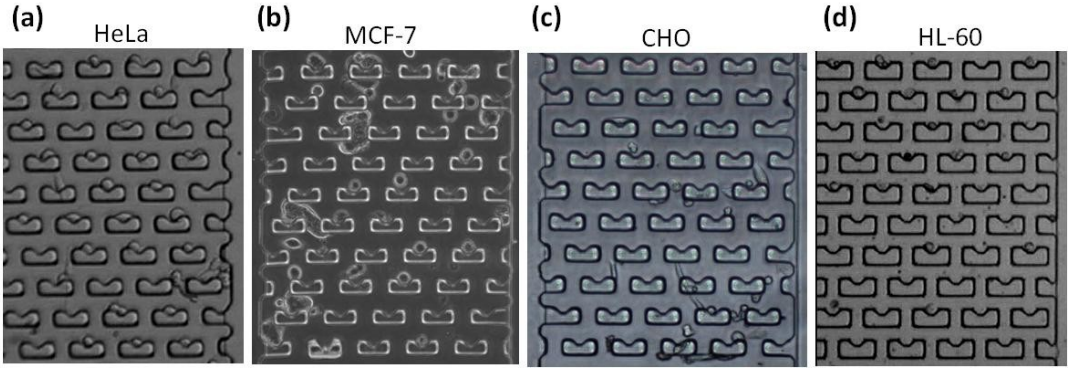

Figure 5.3 Single cell culture results of four different cell lines: (a) HeLa (b)MCF-7 (c) CHO (d) HL-60 The images were taken 24 hours after cell loading. (a) HeLa cells (b)MCF-7 cells (c) CHO cells (d) HL-60, non-adherent human leukemia cells.

5.3.2 Single HeLa cell behavior under drug profile

The result of the anti-cancer drug assay of drug profile (a), 10 μM Taxol dose for 2 hours and switching back to fresh media perfusion, is shown in Figure 5.4. In Figure 5.4 (b), 24 hours after cell loading, changes in cell morphology are observed to move away from a spherical morphology towards an adherent morphology. The anti-cancer drug, Taxol, is then introduced to the cells at this time point. In Figure 5.4 (c), it can be can clearly seen that a big portion of the cells are round up while mitotic arrest happens 24 hours after drug exposure (48 hours since cell loading). 48 hours after drug exposure (72 hours since cell loading), there are several case of the apoptosis shown in Figure 5.4 (d). In Figure 5.5, time-lapsed images of 5 cells under drug profile (a) are organized in such a way that we can clearly time the mitotic arrest events and the cell apoptosis as the data we'll use in the next sub-chapter.

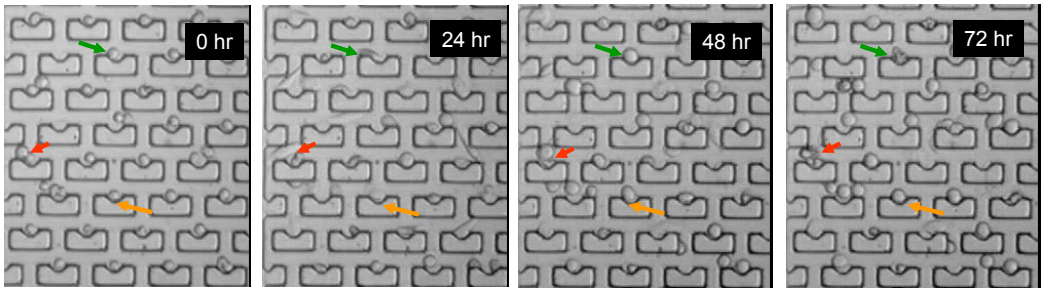

Figure 5.4 Cell morphology after exposure to Taxol. (a) cell image right after cell loading (b) cell image after culture for 24 hours in the single cell array right before introduction of the drug, Taxol (c) 24 hours after Taxol exposure (48 hours from the cell loading) (d) 48 hours after Taxol exposure (72 hours from the cell loading)

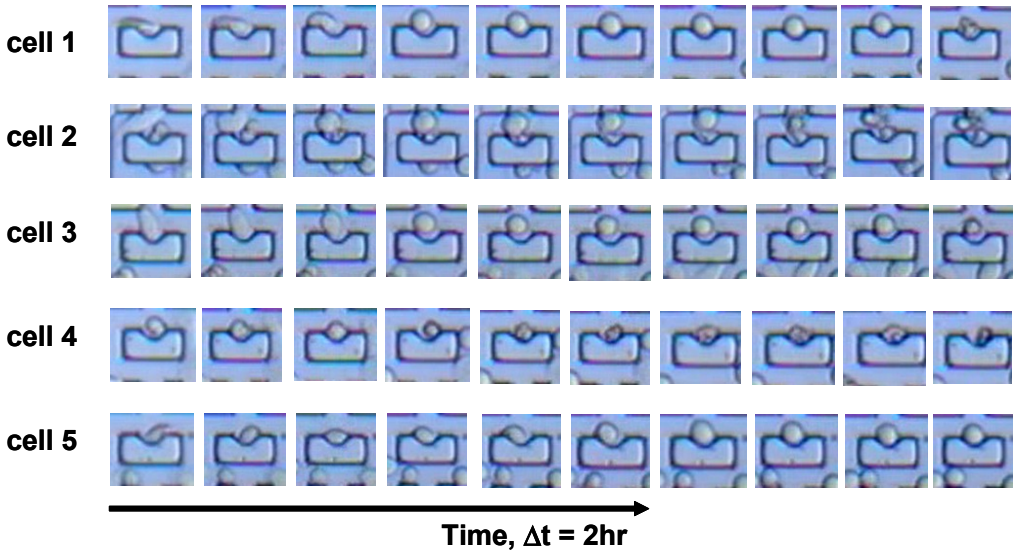

Figure 5.5 time-lapsed images of 5 single cells under drug profile. The image of each cells every 2 hours is shown and the processes of the mitotic arrest and apoptosis are clearly seen.

5.3.2 Taxol concentration-dependent HeLa cell apoptosis

It is generally believed that when cells are treated with low concentrations of Taxol (such as 10–100 nM), suppression of microtubule dynamics may only inhibit formation of mitotic spindles, resulting in an arrest at G2/M phase of the cell cycle.[14,15] Dysfunctional mitotic microtubules might trigger the mitotic spindle checkpoint that promotes apoptosis. Cells arrested at the G2/M phase are characterized by p34/cdc2 activation and Bcl-2 phosphorylation which both contribute to apoptosis. Under this condition, the cells are expected to be arrested in the mitosis for a longer time before they undergoing apoptosis. Some of the treated cells may exit

mitosis since they progressively become less sensitive to the checkpoint signal. This is also an important motivation to pick out these cells for further analysis by using our single cell drug assay platform.

On the other hand, high concentrations of Taxol have been shown to cause massive microtubule damage, which triggers the apoptosis by other signaling pathways. The apoptosis induced by these pathways does not require mitotic arrest and it may occur in a cell at any phase of the cell cycle.

We designed our drug assay using 100 nM Taxol for 2 days and 10 μM for two hours followed by fresh media perfusion. We observed 100 cells for 3 days in each set up. The time of each single cells entering mitotic arrest and apoptosis is recorded and distribution of the duration in between the mitosis entering and apoptosis is plotted. Our data in Figure 5.6 show that under the 100 nM - 2 day dose profile, a big portion the cells underwent apoptosis around ~30 hours after mitotic arrest, providing the supportive evidence of the mitotic spindle checkpoint model. This result also implies the existence of a "clock" within the cell system for the programmed cell death. While under the high dose concentration profile, as shown in Figure 5.7 the apoptosis events didn't correlate with the mitosis very much suggested that massive microtubule damage triggered apoptosis can happen at any time during the cell cycle.

The single cell drug assay system also allows acquirement of clear nuclear deformation analysis images as shown in Figure 5.8. Some cells showed anaphase arrest, in which the division process is frozen at the dose time point. Most of the cells showed DNA condensation which is a typical phenomenon after high dose Taxol treatment. In the high concentration Taxol set up, as shown in Figure 5.9, among the 30 cells that still survived after 3 days culture after drug exposure, 50% were the new born cells within 24 hours priority to the dose. These surviving cells showed higher mobility then the others.

5.3.3 Modification of single cell culture systems for dark-field microscopy

The morphology and movement of single cells cultured in the device can be easily observed under inverted bright-field optical microscopes. For future applications that need the observation under dark-field microscopes, certain modifications are needed. To accommodate the limited working distance of dark-field liquid immersion condensors, the thickness of the PDMS single cell culture device is tailored below 2 mm. The tubing connection junctions need to be strengthened with epoxy and certain distances in between the inlet/outlet and the focus area is needed. Figure 5.10 shows one example of observing a single cell culture device under a dark-field microscope. As shown in Figure 5.10 (a), the boundary of each single trap scattered the oblique incident light and the trap structure is clearly imaged. In figure 5.10 (b) and (c), dark-field images of single cells with and without gold nanoparticle internalization is presented. The bright scattering light from the internalized gold nanoparticles can be clearly seen in Figure 5.10 (c). This dark-field imaging compatible system can be an important for cellular nanoplasmonic spectroscopy researches.

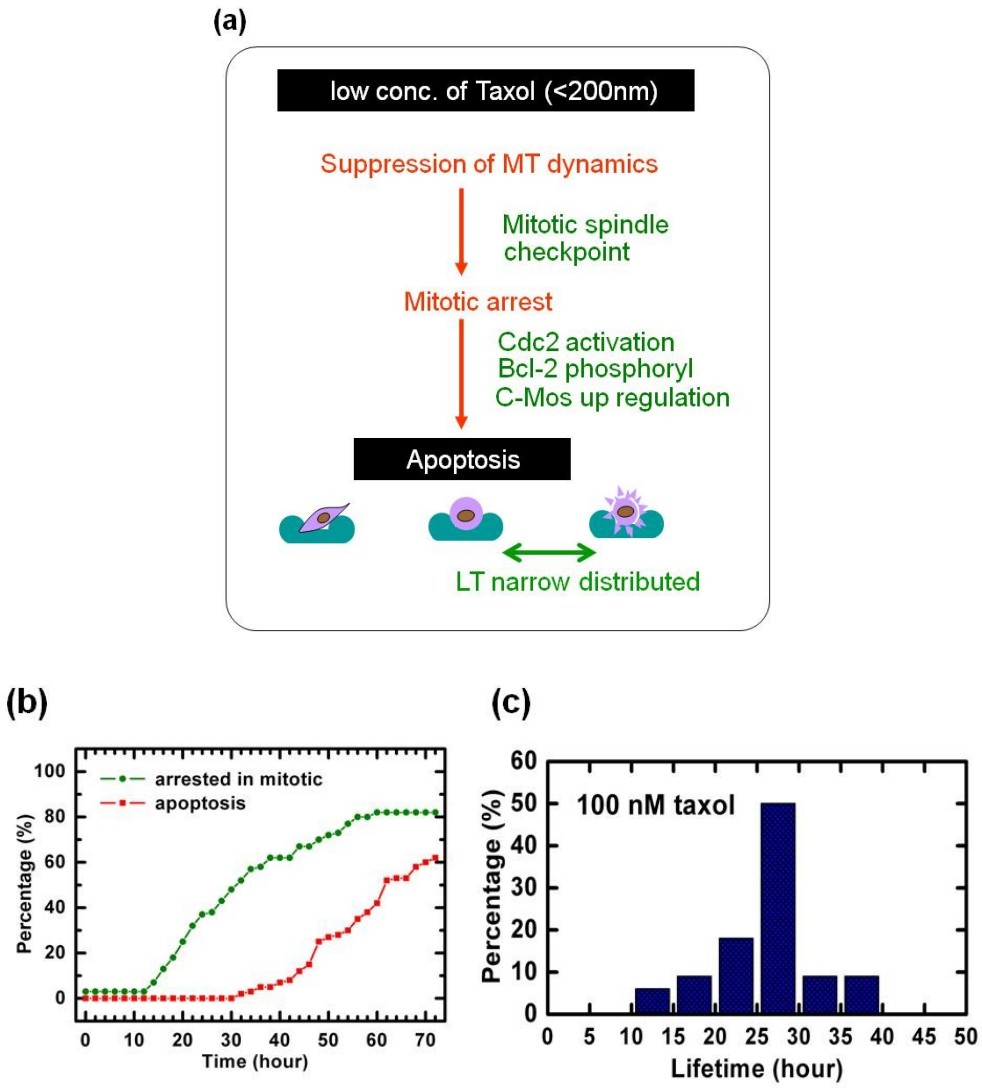

Figure 5.6 Single HeLa cell behavior under a low concentration (100 nM) dose of Taxol. (a) under this dose profile, dysfunctional mitotic microtubules might trigger the mitotic spindle checkpoint that promotes apoptosis. Cells arrested at the G2/M phase are characterized by p34/cdc2 activation and Bcl-2 phosphorylation which both contribute to apoptosis.[4,5] (b),(c) big portion the cells underwent apoptosis around ~30 hours after mitotic arrest, providing the supportive evidence of the mitotic spindle checkpoint model. This result also suggested the existence of a "clock" within the cell system for the programmable cell death.

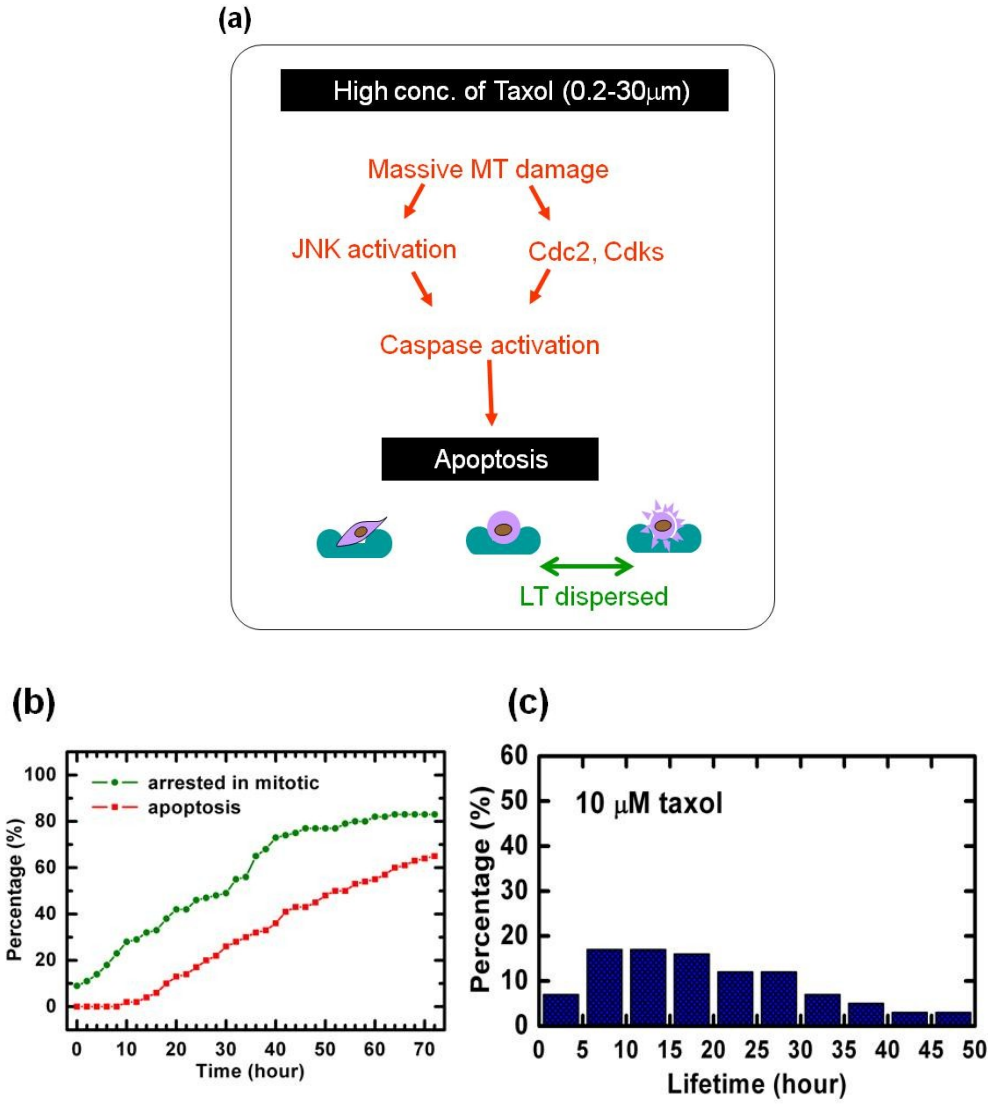

Figure 5.7 Single cell behavior under high concentration (10 μM) dose of Taxol. (a) high concentrations of Taxol have been shown to cause massive microtubule damage, which triggers the apoptosis by other signal pathways.[4,5] (b) (c) the apoptotic events didn't correlate with the mitosis very much showing the massive microtubule damage triggered apoptosis can happen any time during the cell cycle.

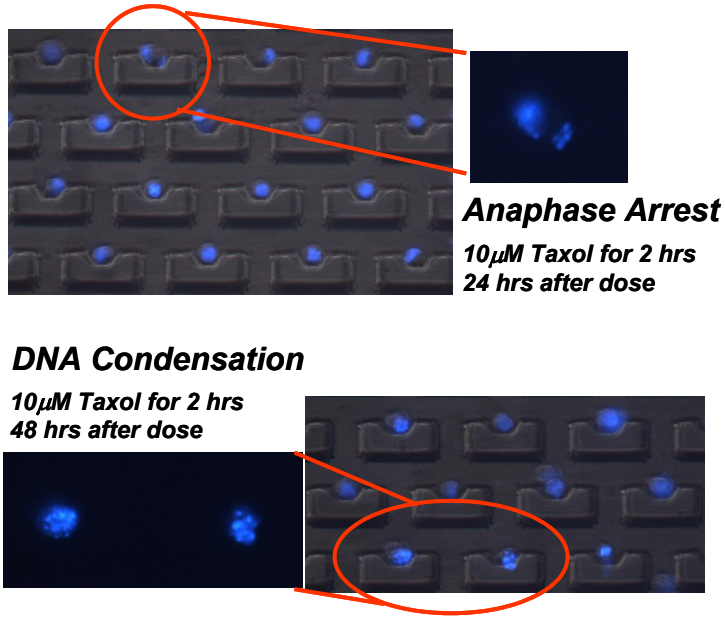

Figure 5.8 Nuclear Morphology analysis after HeLa cells exposed to 10 μM Taxol

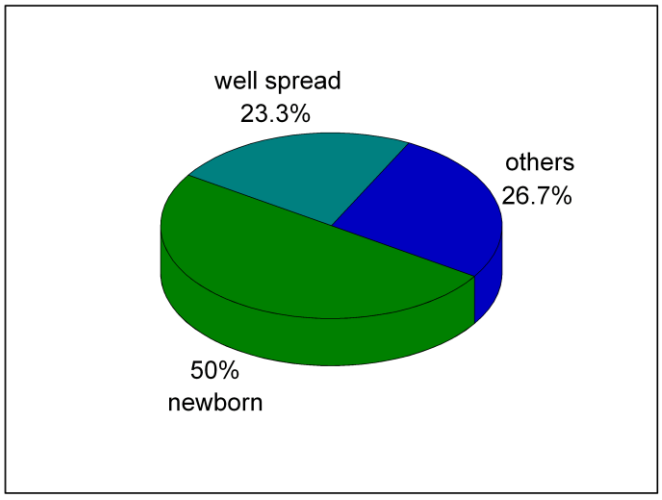

Figure 5.9 Analysis of the cells that survived after 3 days of Taxol dose: among the 30 cells that still survived after 3 days culture after drug exposure, 50% were the new born cells within 24 hours prior to the dose.

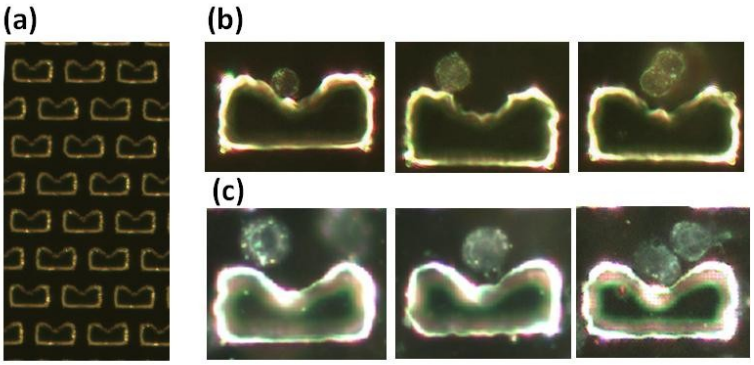

Figure 5.10 Single cell analysis under dark-field microscopy. (a) the boundary of each single trap scattered the oblique incident light and the trap structure is clearly imaged. (b),(c), dark-field images of single cells with (b) and without (c) gold nanoparticle internalization are presented. It can be clearly seen in Figure 5.10 (c) the bright scattering light from the internalized gold nanoparticles. This dark-field imaging compatible system can be an important for cellular nanoplasmonic spectroscopy researches.

5.4 Conclusion

We demonstrate the single-cell microfluidic arrays for long-term cytotoxic drug assays by using the Taxol working on the single HeLa cells. The Taxol concentration dependent cell apoptosis events are analyzed. This device is one of the systems we developed for future integration with the secretion protein detection sensors for single cell drug assay based secretion research. By using the single cell microfluidic array integrated with the nnaoplasmonic probe, we hope to detect cell secretions under specific dose profiles at the single cell resolution.

References:

(1) Lidstrom, M. E.; Meldrum, D. R. *Nature Reviews Microbiology* **2003**, 1 158-164

(2) Rosenfeld, N.; Young, J. W.; Alon, U.; Swain, P. S.; Elowitz, M.B. *Science* 2005, 307, 1962–1965.

(3) Mettetal, J. T.; Muzzey, D.; Pedraza, J. M.; Ozbudak E. M.; van Oudenaarden A. *Proc. Natl. Acad. Sci. U.S.A*. **2006**, 103, 7304–7309.

(4) Kholodenko, B. N. *Nat. Rev. Mol. Cell Biol*. **2006**, 7, 165–176.

(5) Raymond, E.; Buquet-Fagot, C.; Djelloul, S.; Mester, J.; Cvitkovic, E.; Allain, P.; Louvet, C. Gespach, C. *anti-cancer drugs***, 1997**, 8, 876-885

(6) Inoue, A.; Narumi, K.; Matsubara, N.; Sugawara, S.; Saijo, Y.; Satoh K.; Nukiwa T. *Cancer Letters* **2000**, 157, 105-112

(7) Damiano, J. S.; Cress, A. E.; Hazlehurst, L. A.; Shtil, A. A.; Dalton W. S.; *Blood* **1999,** 93, 1658-1667

(8) Belotti, D.; Vergani, V.; Drudis, T.; Borsotti, P.; Pitelli, M. R.; Taraboletti G. *Clinical Cancer Research* **1996**, 2, 1843-1849

(9) Hung, P. J.; Lee, P.; Lee, L. P. *Biotechnology & Bioengineering* **2005**, 89, 1-8.

(10) Di Carlo, D.; Aghdam, N.; Lee L. P. *Analytical Chemistry* **2006**, 78, 4925-4930

(11) Di Carlo, D.; Wu, L. Y.; Lee. L. P. *Lab chip* **2006**, 6, 1445-1449

(12) Wani, M.; Taylor, H.; Wall, M.; Coggon, P.; McPhail, A *J Am Chem Soc* 1971, 93, 2325–2327.

(13) Wang, T. H.; Wang, H. S.; Soong Y. K. *Cancer* **2000**, 88, 2619-2628

(14) Jordan, M. A. ; Toso, R. J.; Thrower, D.; Wilson, L. *Proc Natl Acad Sci* **1993**, 90, 9552–9556

(15) Lieu,C. H.; Chang, Y. N.; La Y. K. *Biochem Pharmacol* **1997**, 53, 1587–1596

CHAPTER 6:
MICROFLUIDIC SELF-ASSEMBLY OF TUMOR SPHEROIDS FOR ANTI-CANCER DRUG DISCOVERY

6.1 Introduction

Multicellular tumor spheroids have recently received a great deal of attention in cancer research and have been applied to the evaluation of anticancer drugs[1]. This is because the 3D multi-cellular aggregates more accurately simulate the tumor micro-environment in vivo by reproducing nutrient and signal gradients and removing the effect of unnatural adhesion to artificial surfaces or gels[2-7]. The intercellular adhesion in tumor spheroids was reported to assist tumor cells evading the cytotoxic effects of anti-cancer drugs[8-10]. For example, the IC50 value for Taxol (commonly used in breast cancer treatments) was reported to be about 2 orders of magnitude higher in spheroids of the MCF-7 breast cancer cell line when compared to cells grown in a monolayer, and this information is valuable for identifying correct clinical dosing[11].

There are several techniques to generate tumor spheroids, such as growth on non-adherent surfaces[12,13], suspension in spinning flasks[14,15], or by the hanging drop method[16,17], but most lack the ability to precisely control the number of cells in each spheroid or allow testing on the growth platform. This could lead to an increased variation in measured IC50 values. Additionally, in all the spheroid culture methods above, the cells in suspension randomly form interactions before intercellular adhesion occurs, and the process to create a sample is cumbersome and time intensive. Existing microfluidic spheroid culture was done by scaling down traditional hanging drop methods to the chip scale[18]. In contrast, our physiologically-inspired biomimetic design is based on a hydrodynamic cell trapping method enabled by microscale fluid dynamics and allows the capability of continuous perfusion flow control and compact spheroid formation, maintenance, and testing all in one platform (Figure 6.1).

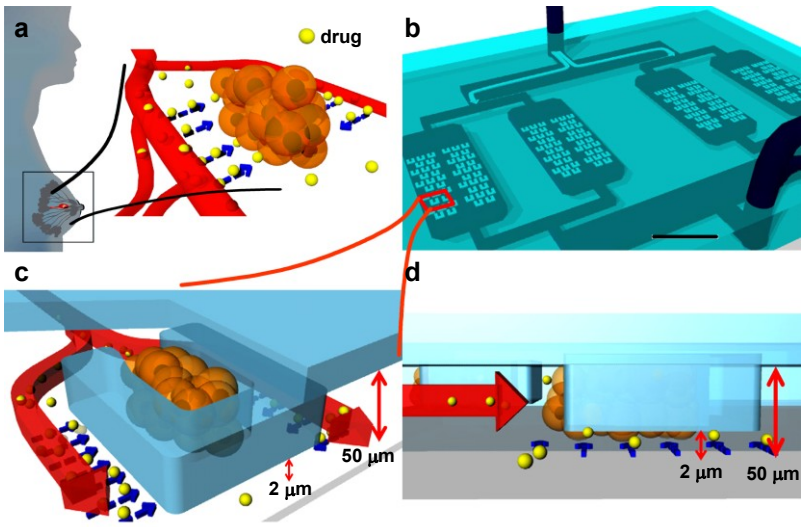

Figure 6.1 Microfluidic spheroid culture array. (a) A schematic diagram of in-vivo tumor spheroid which is characterized by tumor cells aggregating in three dimensions. Drug molecules coming from nearby blood vessels during the dosing are also shown. (b) A diagram of device. The spheroid culture chamber is formed by bonding the PDMS device to a glass slide. In each chamber, there are U-shape traps arrayed in the density of 7,500 traps per square centimeter. (c) Perspective view of one of the U-shape traps. It protrudes from bulk PDMS and traps the cells coming with the flow. Drug molecules coming with the flow enter through the 2 μm perfusion channel underneath the trap which mimics the situation in-vivo. (d) Side view of the trap. The 2 μm perfusion channel is more clearly shown.

We located a number of MCF-7 cells in U-shaped trapping sites on a chip as a cellomic array format [19](Figure 6.2a). The enhancement of spheroid formation was done by maintaining compact groups of cells in the trap due to normal stress resulting from continuous perfusion (Figure 6.2b). A large amount of tumor spheroids (7,500 spheroids per square centimeter) with a narrow size distribution (10 ± 1 cells per spheroid) can be formed in the device. After spheroid formation, long-term culture and drug assays of the spheroids may be performed immediately by loading media or drugs via the same perfusion system (Figure 6.2c-d).

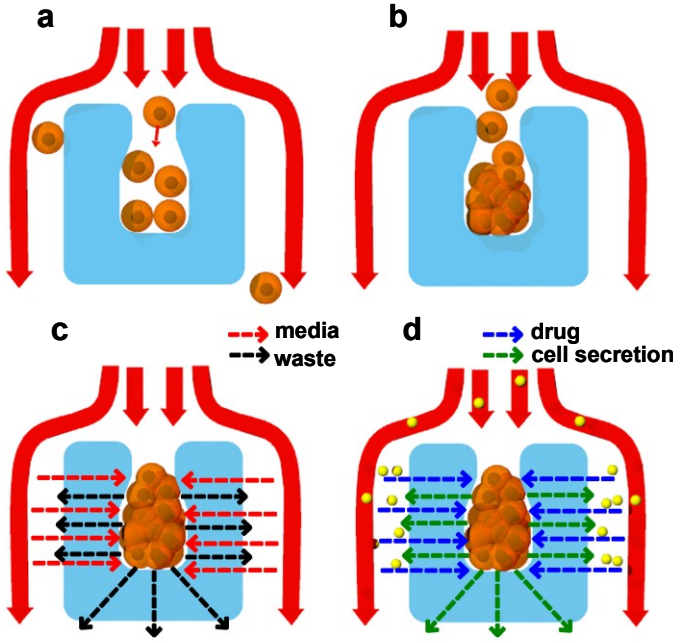

Figure 6.2 Flow-enhanced tumor spheroid culture (a) Cells were trapped by the U-shape trap hydrodynamically. (b) After the cells filled up the traps, enhancement of spheroid formation was done by maintaining compact group of cells in the trap due to normal stress resulting from continuous perfusion. (c) Well-formed tumor spheroids can be long-term cultured by perfusion of the media. (d) Drug assays may be performed by loading drugs via the perfusion system. The cell secretion diffused out of the trap can be gathered and analyzed.

Microfluidic cell culture arrays for individual cells and large group of cells have previously been demonstrated[20-26] . Here we focus on self-assembly of highly uniform cancer spheroids in a dynamic perfusion platform for drug assays. Similar to other cell culture arrays, the device can precisely control the homogeneous environment of each array element by in-vivo like microfluidic perfusion and be utilized for high-throughput analysis.

In this paper, we designed, fabricated the physiologically relevant spheroid array, and characterized the speed of spheroid formation for spheroids containing about 10 MCF-7 cells.. We observed the kinetics of intercellular adhesion in varied conditions of flow induced compression. We focused on small spheroids, which have been reported to have higher resistance to drugs than monolayers[8], but are more difficult to form in a uniform manner than large spheroids using current techniques. Small spheroids more accurately represent tumors at an earlier stage of development, or secondary sites shortly after metastasis. Additionally, the techniques presented can be applied to fabricate different size spheroids based on the experimental requirement by adjusting the trap size.

6.2 Methods

6.2.1 Microfluidic device design and fabrication

The microfluidic spheroid culture array device was fabricated by PDMS (Sylgard 184, Dow Corning) replicate molding using a soft lithography method described previously.[27] The master copies for PDMS molding were fabricated with negative photoresist (SU-8 2002 for 2 μm thick pattern and SU-8 2050 for a 50 μm thick pattern, Microchem Corporation). For device design, each U-shape trap has inner volume of 35 μm x 70 μm x 50 μm, which can typically contain about 10 MCF-7 cells. To allow perfusion flow, we designed a 2 μm gap between the PDMS structure and the glass substrate. After curing PDMS on the mold at room temperature overnight, we cut off a single device, punched the inlet and outlet ports, and then bonded the PDMS device to a glass slide after oxygen plasma treatment. Tubings of 0.12 inch inner diameter (Cole Parmer) were used to connect to syringes for cell loading and media injection.

6.2.2 Tumor Spheroids Culture in Microfluidic Device

Tumor spheroid formation in the microfluidic device was demonstrated by using the MCF-7 breast cancer cell line (American Type Culture Collection, Bethesda, MD). Before loading the cells into microfluidic devices, the cells were cultivated in 100 mm diameter Petri dishes in Dulbecco's Modified Eagle medium containing 10% fetal bovine serum supplemented with 4 mM L-glutamine.

The devices and connecting tubings were sterilized carefully by flushing with 70% ethanol and washed with DI water in a sterile laminar flow hood prior to use. We loaded CO2 Independent Media (Gibco, Grand Island, NY) into the devices first and ensured the channels were free of air bubbles. MCF-7 cells were suspended by trypsinization in 2 mL Trypsin EDTA (0.25 %, Gibco, Carlsbad, CA) plus 6 mL CO2 independent media. Suspended cells at approximately 106 cells ml-1 were loaded into the microfluidic spheroid culture array device for cell trapping. After loading the cells, flow of media (CO2 Independent Medium supplemented with 10% fetal bovine serum, 4 mM L-glutamine, and 1% penicillin / streptomycin) was maintained at 40 μl min^{-1} (average fluid velocity in the chambers of 16 mm sec-1) for 15 mins by programmable syringe pump to rinse away excess cells. The perfusion rate was then switched to 0.05~10 μl min^{-1} to investigate the spheroid formation under different flow rates and applied compression. During the whole process of spheroid culturing, the device was placed on a heated stage at 37^{o}C and images were recorded over time every 6 minutes. For control experiments, the cell suspension was loaded into a 10 ml Petri dish which sat on the same heating and real time observation platform.

Microscopy was performed with either an Olympus CKX41 inverted microscope with a 40X objective for high resolution images and movies, or an Olympus MIC-D for large field of view experiments to collect large amounts of data per experimental run. Data on the speed of spheroid formation was collected from movies by recording the time when all cells in a trap adhere completely to each other. This is observed by determining the loss of contrast or independent movement for individual cells in the trap. In each movie we optimized the view field to contain a maximum of 20 traps to get the clearest images.

To verify the spheroid structure, we use 5-hexadecanoy-laminofluorescein (0.4 μM, Invitrogen) to dye the cell membrane by injecting the dye solution into the microfluidic device at 1 μl min-1 perfusion rate for 10 minutes after 24 hours of culture. Then we dyed the nucleus using Hoechst 33342 (5 μg ml-1, Sigma Aldrich) by injecting the dye into microfluidic device at

1 μl min-1 perfusion rate for 10 minutes. Fluorescent images were then collected using an Olympus CKX41 inverted microscope and attached color camera and imaging software (QCapture Pro).

6.3 Results and discussion

6.3.1 Spheroid array uniformity

For drug assays, homogenous spheroid samples are necessary for statistical analysis. To generate spheroids with a narrow size distribution in an array, the first task is to load equal amount of cells in each trap. The results of trapping uniformity are shown in Figure 3a. The MCF-7 cells filled up the trap space uniformly. The deviation of number of cells in each trap may come from the slight difference of the volume between each individual MCF-7 cell, and will certainly depend on cell type. We dyed the cell nucleus to get the average number of cells in each trap (N= 50) as 9.6 with a standard deviation of 1.31. In the control experiment, we loaded a cell suspension prepared by the same protocol into a 100 mm diameter Petri dish. The size of the cell clusters formed after 14 hours (N=50) was then measured. We compared the seeding uniformity of the trap array with control experiment in Figure 6.3b. After uniformly loading the cells, the second task is to minimize the cells escaping from the trap during the spheroid formation, since MCF-7 cells were seen to actively migrate out of trapping structures during perfusion culture (Supplementary Video 1). Higher flow rate resulted in better uniformity since they confine the cells better and fewer escaping events were observed (Figure 6.3c-d, Supplementary Video 2). Under lower flow rates, the cells escape from one trap to reenter another trap or connect with other escaping cells that resulted in cluttered cells patterns in the trap array (Figure 6.3e).

6.3.2 Spheroid formation and dynamics

After completing the cell loading process, MCF-7 cells filled up the U-shape traps in the microfluidic spheroid culture device. We observed tumor cells adhering to neighboring cells in the same trap gradually under time lapse microscopy (Figure 6.4). This is seen as a gradual reduction in contrast between individual cells. In the trap, the cells were maintained in compact groups and had higher opportunity to interact with each other when compared to those cultured on a plain glass slide or Petri dish (Figure 6.4 d).

The perfusion flow surrounding the trap played an interesting role in spheroid formation. For low flow rates, 0.05 μl min-1 (average velocity = 20 μm sec-1), before trapped cells adhere to each other, a portion of them tended to migrate away through the upper opening of the trap (Figure 6.4 c). To address this, we utilized the normal stress due to the fluid flow to apply a force that maintained cells compressed and able to adhere to each other. In Figure 6.4a, at a perfusion rate of 0.2 μl min-1(average velocity = 80 μm sec-1), we observed that the escaping cells were pushed back by the flow and then formed a spheroid. Under the higher perfusion rate of 10 μl min-1(average velocity = 4000 μm min-1) as in Figure 6.4b, the cells were confined better and formed intercellular adhesions faster. Flow rates above 60 μl min-1 tend to push the cells to squeeze through the 2 μm gap underneath the trap structure thus the optimum flow rate for spheroid culture is in between 10 to 60 μl min^{-1}.

The spheroids formation is very cell type specific. When loading HeLa cells in the same microfluidic device as shown in Figure 6.5, the HeLa cells move away from the trap gradually without forming any solid spheroids.

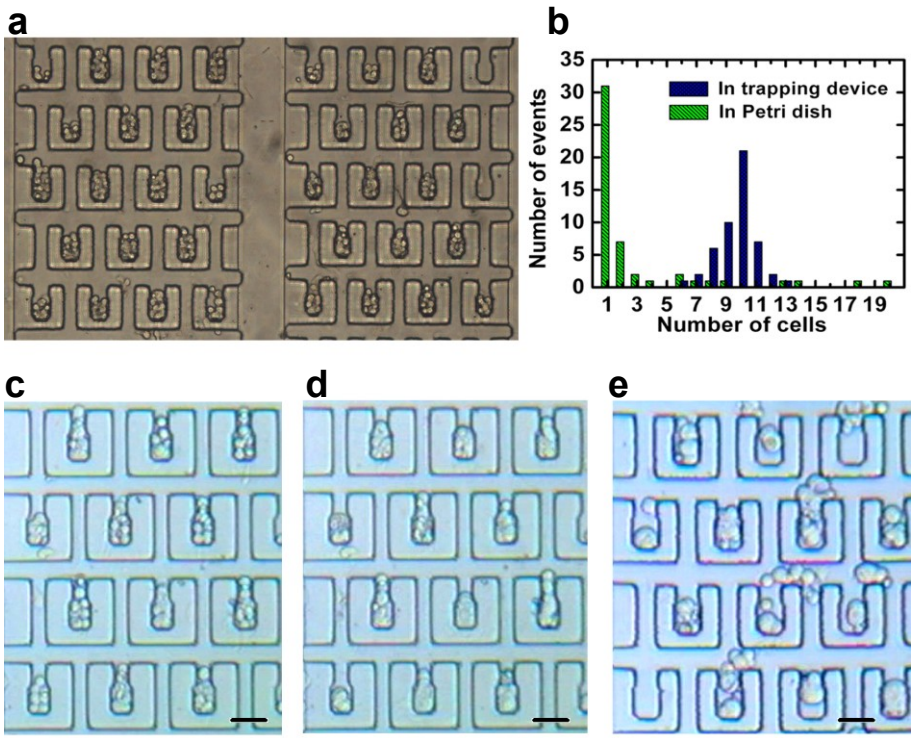

Figure 6.3 Spheroid array uniformity (a) The image taken right after MCF-7 cell loading illustrates that the cells filled up the trap space uniformly. (b) Comparison of cell seeding uniformity in trapping device (blue) and in Petri dish (green). The distribution of number of cells in each cell trap is centered around 10 cells per trap (N=50). While in the control experiment done in Petri dish, there were many single cells seeded and the size of other cells cluster were randomly distributed (N=50). (c) Real time observation of spheroid formation beginning with uniformly trapped cells. (d) After 11 hours of culture at higher flow rate (10 μl min-1), the spheroids formed with better uniformity. (e) Beginning with similar cell trapping uniformity as in (c), a cluttered cell pattern formed under lower flow rate after 24 hours of culture due to cells escaping from the traps. (scale bar = 50 μm).

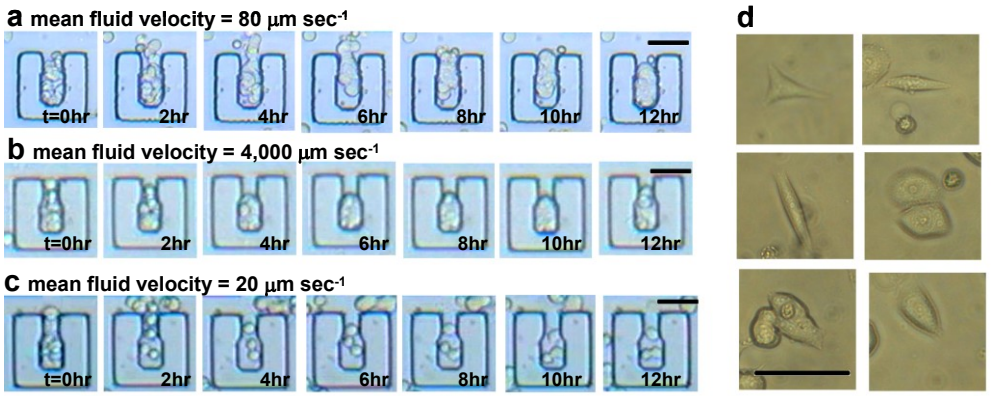

Figure 6.4 Spheroid formation at different average flow velocities. Frames taken from movies for every 2 hours showed (a) for flow rate as 0.2 μl min-1 (velocity = 80 μm min-1), the escaping cells were pushed back by the flow and then formed a spheroid. (b) Under the higher flow rate as 10 μl min-1 (velocity = 4000 μm min-1), the cells were confined better and formed intercellular adhesions faster. (c) For lower perfusion flow, 0.05 μl min-1 (average velocity = 20 μm min-1), before trapped MCF-7 cells adhere to each other, a portion of them tended to migrate away through the upper opening of the trap (d) The spreading morphology of MCF-7 cells cultured in a Petri dish. (scale bar = 50 μm).

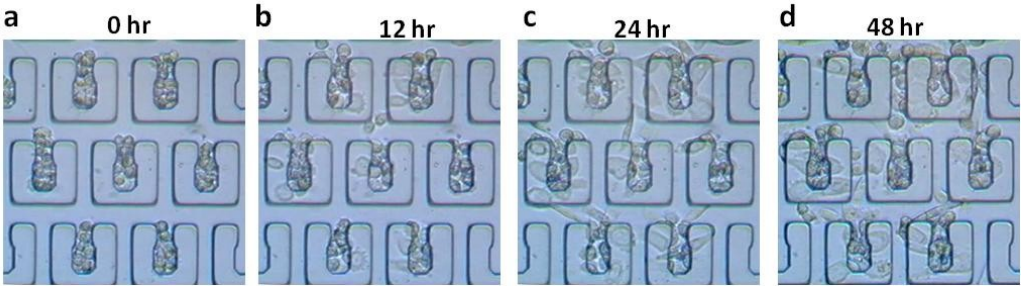

Figure 6.5 Spheroid formation is cell-type specific. Hela cells culture in the cell trap are prone to move away from the trapping zone. (a) cell loading efficiency is similar to the loading of MCF-7 cells (b)12 hours after loading, some cells are trying to move out from the trap (c)(d) 24 and 48 hours after cell loading, more cells move away and there are no spheroids formed.

The time of spheroid formation is shorter under higher flow rates since cells were more compactly grouped in the trap. At different perfusion rates of 10, 0.6, and 0.05 μl min-1, the average time for spheroid formation are 7, 9, and 11 hours respectively (Figure 6.6). To further investigate the structure of the spheroids, we dyed the cell membranes and the cell nuclei (Figure 6.7b-c). The images indicated separate cells were adhering to form a combined structure. This was further supported when after 24 hours of culture we applied high pressure and dislodged entire spheroids – not individual cells. In Figure 6d a well-formed spheroid that was pushed out from one of the microfluidic traps is shown.

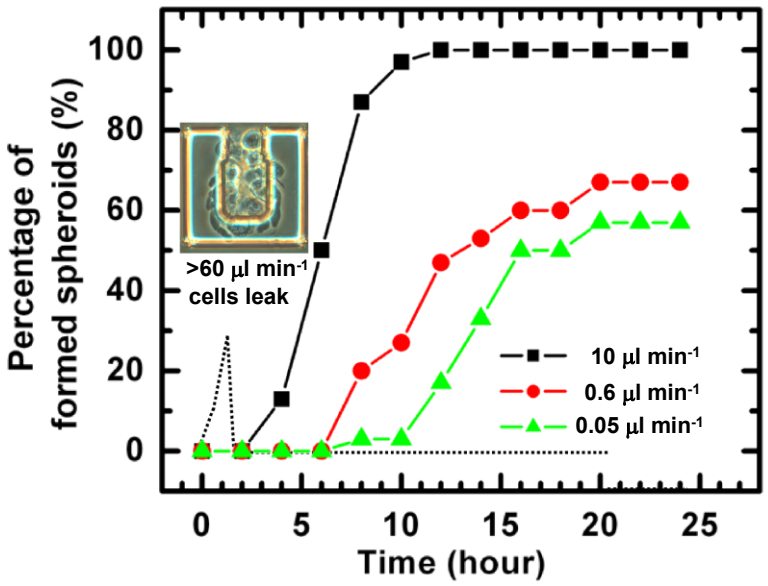

Figure 6.6 Dynamics of spheroid formation. The percentage of well-formed spheroids in the trap array under perfusion flow rate of 10 μl min-1 (N=30), 0.6 μl min-1(N=15), and 0.05 μl min-1 (N=30) are reported every 2 hours. The analysis shows that the time of spheroid formation is shorter and the percentage of well-formed spheroids is larger under higher flow rate. Flow rates above 60 µl min-1 tend to push the cells to squeeze through the 2 µm gap underneath the trap structure (the dotted line).

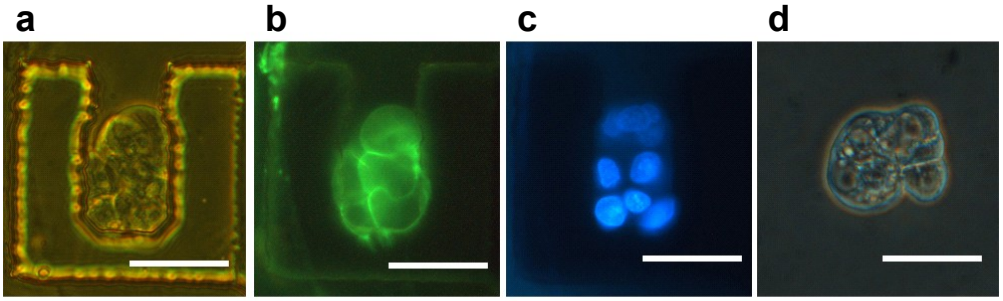

Figure 6.7 Detailed structure of spheroids (a) A phase contrast image of a spheroid formed in the trap. (b) An image of a spheroid with fluorescent dyed cell membranes which shows the separate cells were adhering to form a combine structure. (c) An image of a spheroid with fluorescent dyed cell nuclei which shows distinct cell nuclei rather than one fused nucleus in the spheroid. (d) A phase contrast image of a well-formed spheroid pushed out from one of the microfluidic traps. (scale bar = 50 μm)

6.4 Conclusions

The biologically-inspired microfluidic self-assembly of spheroids and formation with perfusion flow control allows us to maintain compact groups of the trapped cells and enhance spheroid formation. Increased flow (up to 10 μl min^{-1}) is shown to enhance spheroid rate of formation and increase spheroid uniformity (10±1 cells per spheroid) presumably by maintaining tighter contact between cells. With this platform, anti-tumor assays can be done immediately after the spheroid formation right in the growth platform. This may lead to identification of improved dosage regimes for anti-cancer drugs in pre-clinical in-vitro experiments, saving time and reducing costs.

References:

(1) Desoize, B. *Crit Rev Oncol Hematol* **2000**, 36, 59- 60.
(2) Mueller-Klieser, W. *Crit Rev Oncol Hematol* **2000**, 36, 124-139.
(3) Sutherland, R. M. *Science* **1988**, 240, 177–184.
(4) Knuechel, R.; Sutherland, R. M. *Cancer Journal* **1990**, 3, 234–43.
(5) Acker, H. J. *Theor. Med* **1998**, 1, 193–207.
(6) Mueller-Klieser, W. *Am J Physiol* **1997**, 273, C1109–C1123.
(7) Bates, R. C.; Edwards, N. S.; Yates, J. D. *Crit Rev Oncol Hematol* **2000**, 36,61–74.
(8) Olive, P. L.; Durand, R. E.; *Cancer Metastasis Review* **1994**, 13, 121-138.
(9) Desoize, B.; Gimonet, D.; Jardiller, J. C.; *Anticancer Res* **1998**, 18, 4147–4158.
(10)Faute, M. A.; Laurent, L.; Ploton, D.; Poupon, M. F.; Jardillier, J. C.; *Bobichon H. Clin Exp Metastasis* 2002, 19, 161-168.
(11) Nicholson, K. M.; Bibby, M. C.; Philips, R. M. *European Journal of Cancer* 1997, 33, 1291-1298.
(12) Yuhas, J. M.; Li, A. P.; Martinez, A. O.; Ladman, A. J. *Cancer Res.* 1997, 37, 3639-3643.
(13) Haji-Karim, M.; Carlsson, J. *Cancer Res.* 1978, 38, 1457-1464.
(14) Sutherland, R. M.; McCredie, J. A.; Inch, W. R.; *J Natl Cancer Inst* 1971, 46, 113-120.
(15) Kunz-Schughart, L. A.; Kreutz, M.; Knuechel, R. *Int J Exp Pathol* 1998, 79, 1–23.
(16) Keller, G. M. *Curr Opin Cell Biol* **1995**, 7, 862-869.
(17) Kelm, J. M.; Timmins, N. E.; Brown, C. J.; Fussenegger, M.; Nielsen, L. K. *Biotechnology & Bioengineering* **2003**, 83, 173-180.
(18) Torisawa, Y.; Takagi, A.; Nashimoto, Y.; Yasukawa, T.; Shiku, H.; Matsue, T. *Biomaterials* **2006**, 28, 559–566.
(19) Di Carlo, D.; Aghdam, N.; Lee, L. P. *Analytical Chemistry* **2006**, 78, 4925-4930.
(20) Deutsch, M.; Deutsch, A.; Shirihai, O.; Hurevich, I.; Afrimzon, E.; Shafrana, Y.; Zurgil, N. *Lab Chip* **2006**, 6, 995–1000.
(21) Di Carlo, D.; Wu, L. Y.; Lee, L. P. *Lab Chip* **2006**, 6, 1445–1449.
(22) Chin, V. I.; Taupin, P.; Sanga, S.; Scheel, J.; Gage, F. H.; Bhatia, S. N. *Biotechnology & Bioengineering* **2004**, 88,399-415.
(23) Kim, L.; Vahey, M. D.; Lee, H.; Voldman, J. *Lab Chip* **2006**, 6, 394–406.
(24) Thompson, D. M.; King, K. R.; Wieder, K. J.; Toner, M.; Yarmush, M. L.; Jayaraman, A. *Analytical Chemistry* **2004**, 76, 4098-4103.
(25) Hung, P. J.; Lee, P.; Lee, L. P. *Biotechnology & Bioengineering* **2005**, 89, 1-8.

(26) Tourovskaia, A.; Figueroa-Masot, X.; Folch, A. *Lab Chip* **2005**, 5, 14–19.
(27) Hung, P. J.; Lee, P.; Sabounchi, P.; Aghdam, N.; Lin, R.; and Lee, L.P. *Lab Chip* **2005**, 5, 44-48.

CHAPTER 7:
INTEGRATION OF NANOPLASMONIC OPTICAL SENSOR ARRAYS AND MICROFLUIDIC CELL CULTURE PLATFORMS

7.1 Integration technologies

The nanoplasmonic optical sensor arrays on glass allow for effective integration with microfluidic cell culture systems. Since the PDMS-based microfluidic cell culture platforms are usually bonded to the glass support, integration of nanofabricated plasmonic sensor arrays on glass substrate with PDMS microfludics is a logical step to develop label-free bioassay systems. However, there are several issues to overcome during the integration process.

The first critical issue is the interface between noble metal nanoplasmonic sensor arrays under and PDMS-based microfluidic devices. The plasmonic material such as gold cannot form permanent bonding with PDMS after standard oxygen plasma treatment. If we pattern the whole glass substrate with the nanoplasmonic structure, the bonding is relatively weak compared to pure glass-PDMS bonding. In this case, the microfluidic device can only be operated under liquid drag mode from the outlet or a low pressure perfusion mode. By patterning the nanoplasmonic probes only in the microfluidic channel/chamber area, where there is no direct contact with the surface of PDMS, we can avoid the direct bonding problem of Au and PDMS. In the following content, I will demonstrate plasmonic optical sensor arrays patterning for better integration with microfluidic devices.

The second issue that needs to be considered is the cell-substrate interface. Usually in the microfluidic cell culture system, the cells are cultured on top of the glass surface, while in the nanoplasmonic cell culture systems, the cells are cultured on top of the surfaces covered with gold nanostructures. Different cell lines may have different preferences to adhere to the nanoplasmonic surface and the growth of cultured cells on top of the nanoplasmonic substrates need to be carefully checked and characterized. Proper surface chemistry functionalization is needed for some cell lines that are not prone to adhering to gold surfaces.

Finally, for the functionalization of antibodies or other grabbing molecules for bio-molecular detection, the process of surface chemistry needs to be done on-chip, and this again needs certain modifications of the process and final characterization to make sure the surface functionalization is as complete as off-chip conditions.

7.1.1 Patterning nanoplasmonic probes to specific testing area

To precisely pattern the nanoplasmonic probes to the specific testing area, a lift-off process on photolithography patterned glassed is adopted. Figure 7.1 shows an example of the testing area patterning. The cell culture chip in this case has cell culture chamber aligned in parallel. In Figure 7.1 (a) – (c), the nanoplasmonic probes are patterned on the whole cell culture chamber area. In this case, each culture chamber as shown in Figure 1(g) is overlapping with the nanoplasmonic area, the bonding between the PDMs and substrate is weaker, but on the other

hand, the testing point can be set anywhere in the microfluidic system, and it requires no efforts to align the PDMS device and bottom nanoplasmonic area.

Alternatively, the nanoplasmonic probes can be patterned everywhere except the area for PDMS-glass bonding. As shown in Figure 7.1 (d)-(f), the nanoplasmonic probes are patterned to match the cell culture chamber area (more detailed image shown in Figure 7.1 (h)). In this scheme, the cells are grown on top of the nanoplasmonic sensor arrays, and the protein composition in the proximity of the cells is able to be read out. The detection can also be done on the testing spots away from the cell culture region. To well align the PDMS devices with the patterned nanoprobes, after oxygen plasma treatment on both PDMS and substrate, a thin layer of ethanol is sandwiched at PDMS/glass interface. The alignment is done by sliding the PDMS chip to specific position under microscope, after which the permanent bonding is formed after sandwiched ethanol layer dried.

Instead of overlapping the whole cell culture chamber with the nanoplasmonic probes, the nanoplasmonic probes can also be patterned in the specific testing area. Figure 7.1 (i) shows a bar with 150 micron width is patterned with nanoplasmonic probes aligned to the end of the cell trap in each culture chamber. In this case, the probes are placed close to the cell culture area without overlapping with it. The cells are growing on the probe-free area and their secretion molecules were flowed through the 2 um channel downstream for the detection.

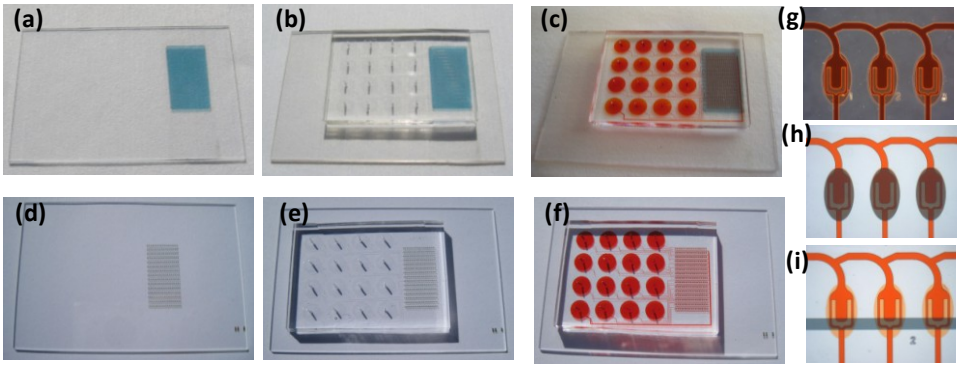

Figure 7.1 Patterning of nanoplasmonic probes. (a)-(c), (g): nanoprobes patterned on the whole cell culture chamber array area. (d)-(f), (h): the nanoprobe pattern is match to cell culture chamber area. (i) nanoprobes patterned to specific testing area aligned to the cell culture device.

7.1.2 Cell growth on top of nanoplasmonic substratesg

Different cell lines may have different preference to adhering to the nanoplalsmonic surface. Based on the cell line chosen for specific experimental purpose, the cell growth must be characterized in advance. Figure 7.2 listed the results of 4 different cell lines grown on plain gold and 11-mercaptoundecanoic acid (11-MUA) functionalized gold surface. The growth of CHO and NIH3T3 cells are similar on plain and 11MUA-functionalized surfaces, while MCF-7 and HeLa cells spread better on 11-MUA functionalized cell surface.

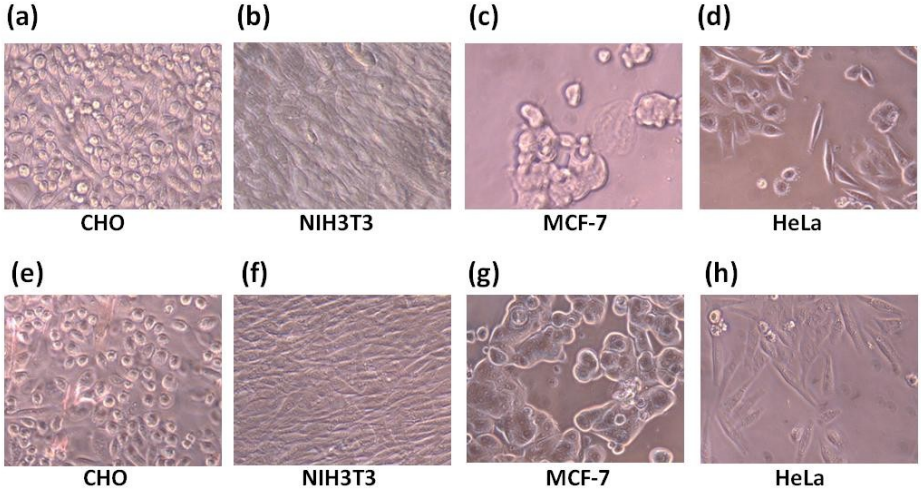

Figure 7.2 Culturing different cell lines on top of crescent-shaped nanohole substrates. (a)-(d) cell culture on plain gold surface. (e)-(h) cell culture on 11-MUA functionalized gold surface.

7.2 An example: quantification of Amyloid-β in microfluidic cell culture arrays integrated with plasmonic nanosensors

Alzheimer's disease is a debilitating neurodegenerative disorder in the elderly affecting more than 26 million people worldwide. One major pathological marker of the disease is the extra-cellular deposits that consist of Amyloid-β (Aβ) protein aggregates. If we zoom in on a neuron cell as illustrated in Figure 7.3, Aβ is the middle segment of a larger trans-membrane protein called APP.[1] Two sequential enzymatic cleavages release Aβ from the surface and the resulting higher concentration causes formation of oligomers or plaques that are neurotoxic. One of the most pursued therapeutic strategies for Alzheimer's disease is to inhibit these two enzyme systems, so a good tool for high throughput drug screening to find the effective inhibitors is necessary.

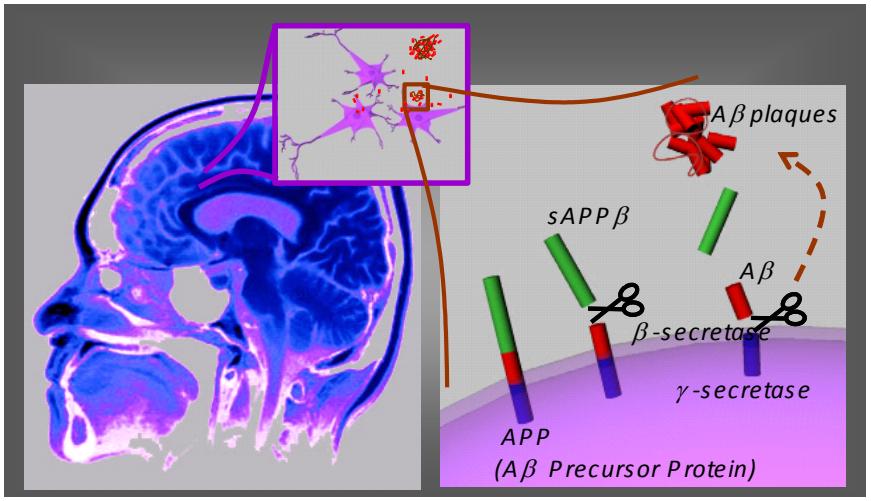

Figure 7.3 Amyloid-β protein produced at the surface of a neuronal cell. Two sequential enzymatic cleavages, β secretase and γ secretase, release Aβ from the surface and the resulting higher concentrationfo Aβ that causes formation of oligomers or plaques that are neurotoxic.

The current method for Aβ secretion quantification is to culture the cells in a petri-dish, give them different testing conditions, take out the cell supernatant and do an ELISA test.[2,3] The commercial Amyloid beta ELISA kits are reported to test Aβ concentration down to picomolar range.[4] However, there are several issues with this. First, the process is slow since it includes several washing steps. It is impossible for real-time monitoring of secretion activity from the cells. There is no spatial resolution and it needs large amounts of reagents. There were several techniques proposed for high-throughput screening for cell-based Aβ concentration assay by using homogeneous time-resolved fluorescence (HTRF) assay.[5,6] The detection of limit of this FRET based technology for Aβ is about 1 nM, which is sufficient for the Aβ presented in the cell supernatant (~ tens of nM)[3] from standard 96 or 384 well cell culture set up. But this technique can only report the Aβ concentration of the cell supernatant at a specific time point, no time-lapsed information about cell secretion can be accomplished and also only the Aβ from bulk

cells were collected and quantified without other information such as cell proliferation and morphology.

We can overcome the limitations of existing Aβ setection technologies by culturing the cells in a microfluidic system with a plasmonic substrate integrated at the bottom of the cell culture chambers (Figure 7.4). A microfluidic system provides an easier platform for cell handling and reduced reagent usage. Each gold nanostructure on the substrate serves as an individual biosensor that allows us to detect Aβ real time at a nanometer scale spatial resolution. The goal we have set is to detect secretion of Aβ on-chip directly by optimizing the cell culture platform and subsequent plasmonic based Aβ detection. Furthermore, we hope to apply the system for drug screening of Aβ inhibitors.

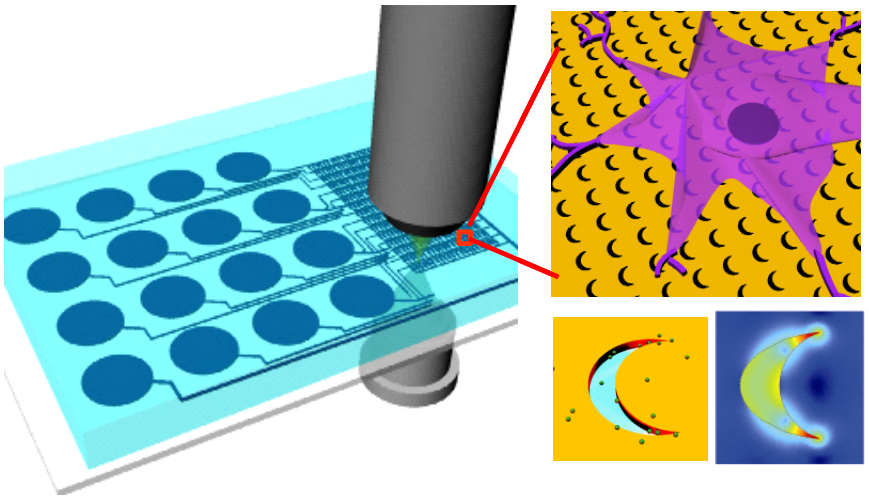

Figure 7.4 Schematic of the microfluidic Aβ detection system. Each gold nanostructure on the substrate serves as an individual biosensor that allows label-free real-time detection of Aβ.

7.2.1 Methods

There are two major parts to be integrated for the cell secretion detection platform. For the microfluidic cell culture platform in this experiment, we use the same hydrodynamic cell trapping technology as described in Chapter 5 and Chapter 6 while modified the trap size for 200 cells per trap. Based on the specific purpose for the cell secretion research, the single cell (Chapter 5) and tumor spheroid (Chapter 6) culture platform can also be integrated with the plasmonic probe by the same method.

Both crescent-shaped nanohole substrates were adopted in the integrated Aβ secretion detection system. The cell culture chamber area on the PDMS side was aligned the nanoplasmonic patterned glass slide following the methods described in Chapter 7.1.1.

The SERS measurement was done by focusing a 5 mW 785 nm laser beam on crescent-shaped substrate immersed in known concentration of Aβ solutions by a 20X microscopy objective lens (NA = 0.4). The back scattered Raman signals were then collected by the same objective lens and analyzed by a spectroscopy. The measurement area was 3 μm by 1 μm, defined by the focused laser spot and the slit in front of the spectrometer.

7.2.2 Results and discussion

The microfluidic Aβ real-time detection system is shown in Figure 7.5 (a)-(b). There are 15 independent inlets that allow for 15 testing conditions, with 25 parallel chambers for data acquisition each. The cells we used in this project were APP transfected CHO cells provided by Professor Xia from Harvard Medical University. As we mentioned earlier in this chapter, APP is the larger transmembrane protein where Aβ is from. So the cells can secrete 15 times more Aβ than normal neuron cells and are therefore ideal for Aβ inhibition assays. Based on published data on the cells, we estimated that the daily secretion from the cells can result in around tens of nM in the device in average and the local concentration near the cells might be even higher. The figure shows the cells proliferate during the 36 hour culture. Our next step is to culture the cells on top of the nanostructure substrate and read out the Aβ secretion from these sensors.

Figure 7.5(c) shows the cells proliferate during the 36 hours culture. The APP transfected CHP cells are growing well on untreated plasmonic substrates. At 36 hours after cell loading we can clearly observed the cell attachment and proliferation. Our next step is to read out the Aβ secretion from the plasmonic nanosensors at the bottom.

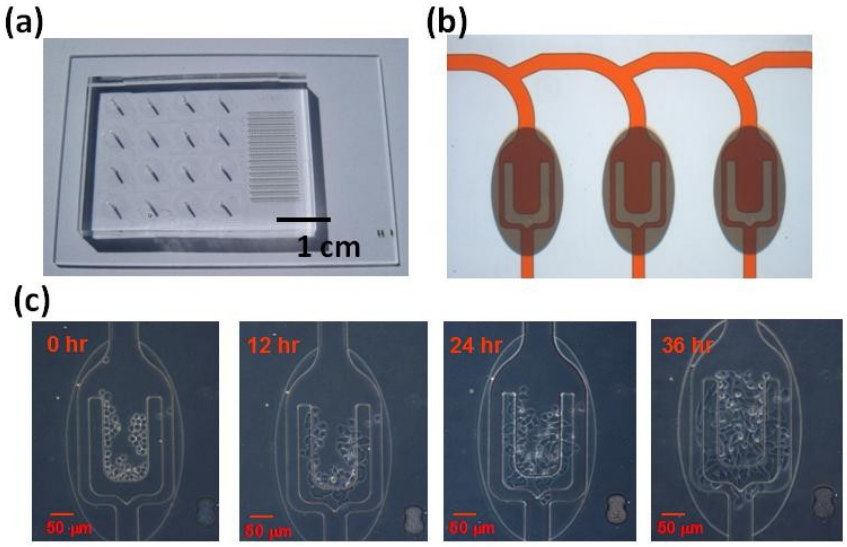

Figure 7.5 Microfluidic cell culture for Aβ secretion analysis (a) The image of the plasmonic and cell culture integrated device (b) Each cell loading chamber is design to contain 200 cells. (c) Culturing results of APO transfected CHO cells. Cell attachment and proliferation is clearly observed 36 hours after cell loading.

Based on the data published previously in literature, the SERS limit of detection of two water soluble protein, albumin and lysozyme, are reported to be 10^{-6} M (10^{2}-10^{3} times lower than the minimum necessary for recording Raman Scattering spectra in solution.)[8] Protein is comprised of amino acids, and there are several amino acids that have larger Raman scattering cross sections and dominate the composite SERS signal from the protein. Aromatic amino acids

[phenylalanine (Phe), tryptophan (Trp) and tyrosine (Tyr)] and aliphatic amino acids [leucine (Leu), valine (Val) and glycine (Gly)] are the major source of the Raman scattering from protein samples, other secondary structures like β sheet structures also contribute to the protein Raman spectrum fingerprint. Different proteins are composed of 14 basic amino-acids. The major peaks of different proteins are positioned closely with slight modification due to the overall protein structure. Compared to other Aβ detection methods relying on fluorescence or other labeling methods, SERS doesn't need any surface functionalization and a labeling process.

For the Aβ SERS measurement conducted on the crescent-shaped nanoholes substrates, we haven't been able to get a very reproducible data at a 1 nM concentration, which is required for on-chip Aβ secretion detection. How to push the sensitivity into useful detection ranges is a challenging task that needs to be finished in the future. The on-chip measurement of Aβ secretion from the cultured APP transfected CHO cells hasn't been finished, however, these pioneer works pave the way for an integrated microfluidic system for SERS-based detection of Amyloid beta secretion in real time.

7.3 Wafer scale integration of nanoplasmonic sensor arrays and microfluidic platforms

The combination of two important tools, label-free nanoplasmonic sensor arrays and microfluidic bioassay platform, can impact new drug discovery, drug screening, and evaluation of therapeutic methods. Moving toward the goal of real product applications, a reproducible and efficient fabrication technology for integrated optical microfluidic platform with nanoplasmonic sensor arrays is in critical demand. The fabrication technology of microfluidic devices with glass or polymeric materials is well established. However, uniform wafer-scale nanofabrication of plasmonic probes is challenging problem to solve first before we integrate polymeric substrate for microfluidics and glass substrate for nanoplasmonics.

The fabrication method of the nanoplasmonic substrates reported in Chapters 3 & 4 is based on nanosphere templates. As discussed in Chapter 2.1, nanosphere lithography faces the challenge of making a uniform large area nanostructure array. A great amount of the efforts have been made for generating wafer-scale nanosphere array,[9-12] and the spin-coating of silica nanospheres suspended in monomer liquid followed by photon-induced polymerization of the monomer proposed by Jiang et al. is the most effective and efficiency method. Although the uniform monolayer of the nanosphere close-packed array is able to be made on 4 inch wafer, the local defects on the array are unavoidable. While putting the wafer-scale nanosphere array template fabrication in future works, here I propose a nanoplasmonic probes array with micron-scale pitch fabricated by photolithography methods.

Since we need to accomplish reliable and reproducible large area plasmonic susbstrate, a top-down fabrication method such as photolithography is a logical step in creating the predetermined pattern on Si or glass wafers. It is still challenging to form nanopatterned structures with spatial pitch under 200 nm by photolithography. However, for the application of mapping of membrane proteins, the inter-nanostructure distance of 1~2 μm is appropriate for a label-free optical detection from each "pixel" of the nanoplasmonic sensor array.

Here, a wafer-scale nanoplasmonic sensor array by using a photolithographic method is presented. The photoresist pillar array with 0.8 μm diameter and 1.6 μm pitch was made on whole 4" glass wafer coated with a thin layer of gold film. Followed by dry etching, the size of photoresist pillar etching mask is tailored while the gold disk underneath the photoresist mask is formed. A 4" wafer PDMS microfluidic device was then bond to the nanoplasmonic array patterned glass wafer for the integration of single cell culture system with nanoplsmonic biosensor functionality.

7.3.1 Method

The fabrication of a wafer-scale nanoplasmonic sensor array starts with gold coating on the 4" Borofloat glass wafer. The glass wafer is first cleaned by piranha solution for 10 minutes and then 50 nm of gold film is thermal evaporated onto the glass wafer (Edwards EB3 Electron Beam Evaporator). A 1.2 μm thick positive photoresist (Hitachi OCG OiR 700-10) is then spin coated on to the substrates. The photoresist pillar array with 0.8-1.4 μm diameter and 1.6-2.8 μm pitch is patterned by GCA 6200 wafer stepper. The wafer with patterned photoresist pillar etching mask is then loaded into the ion-milling system for dry etching with a specific etching time. The photoresist mask pillars shrink in size during ion milling and the gold disk array with smaller than 200 nm in diameter was thus formed and will be used as a nanoplasmonic sensor.

The microfluidic devices were fabricated by standard SU-8 photoreisist molding methods described in previous chapters. The microfluidic cell culture chamber is laid out to match the

stepping distance of the nanoplasmonic probe pattern. After aligning and bonding the microfluidic cell culture PDMS device onto the 4" glass wafer with nanoplasmonic probes array, the wafer-scale integration of nanoplasmonic and microfluidic platform is then completed.

7.3.2 Results and Discussion

The nanoplasmonic probes array patterned wafer is shown in Figure 7.6 (a). The rainbow color shown on the wafer resulted from the grating diffraction of the ambient light. The SEM figures of photoresist pillar array on top of gold film are shown in Figure 7.6(b), and the pattern is uniform among the whole wafer. In Figure 7.7 the gradual formation of the nanodisk is shown. The heat generated during the ion milling process makes photoresist reflow to hemisphere shape. The shape is gradually transferred to the underlying glass substrate during directional ion-milling process. After etching for 20 mins, we can see a lens like glass basis with smaller photoresist hemisphere remained on top of it, and a 50 nm thick gold nanodisk is formed underneath the photoresist hemisphere. Further fine-tuning of the nanodisk size is made by incremental adding of the ion milling etching time. After removal of the ptotoresist, the nanoplasmonic sensor array is finished.

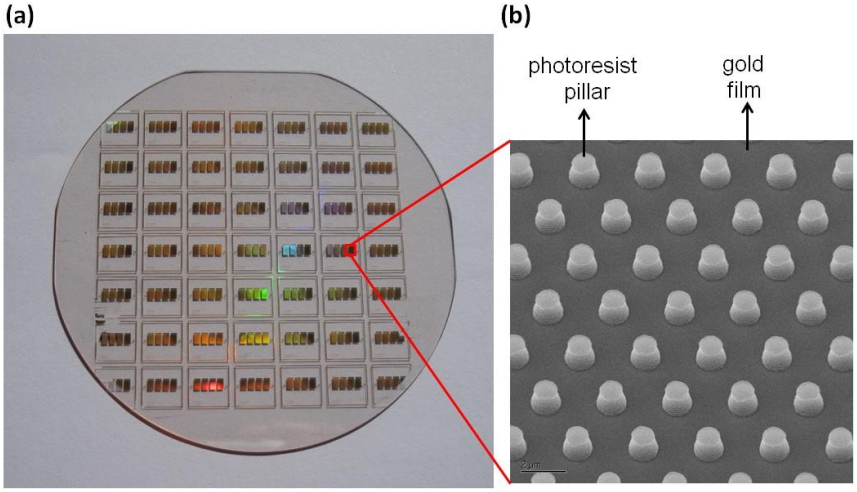

Figure 7.6 Wafer-scale nanoplasmnic probes fabrication on a glass wafer. (a) The nanoplasmonic probes array patterned on the whole 4" glass wafer. The rainbow color shown on the wafer is resulted from the grating diffraction of the ambient light. (b)The SEM figures of photoresist pillar array on top of gold film are shown.

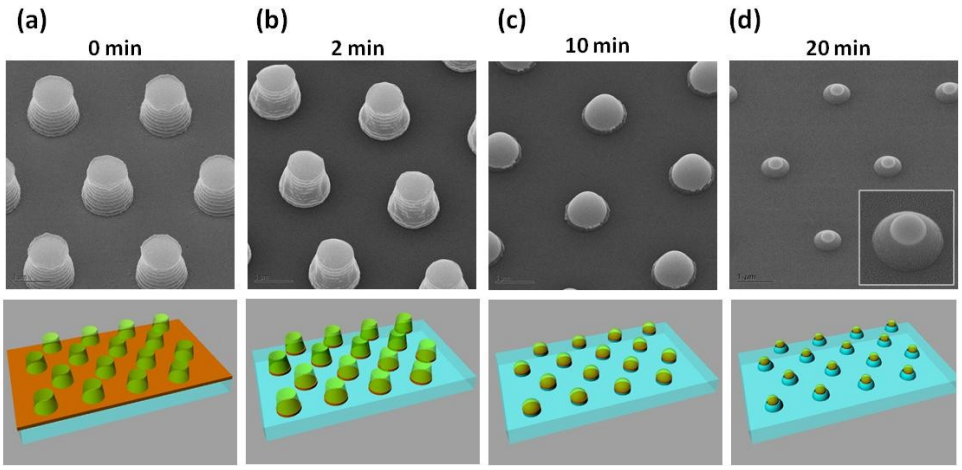

Figure 7.7 Gradual formation of nanoplasmonic probes by controlled ion-milling time. The heat generated during the ion milling process makes photoresist reflow to hemisphere shape. The shape is gradually transferred to the underlying glass substrate during directional ion-milling process. After etching for 20 mins, we can see a lens like glass basis with smaller photoresist hemisphere remained on top of it, and a 50 nm thick gold nanodisk is formed underneath the photoresist hemisphere.

The microfluoidic devices is shown in Figure 7.8 and Figure 7.9. The 7x7 array of the single cell culture devices are arranged to match the stepping pattern on the nanoplasmonic glass substrates. CGA 8200 wafer stepper was first tried to pattern the SU-8 mold of the PDMS device. However, the g-line light source (436 nm) of the stepper is not able to cross-link the SU8 polymer (whose photo-reacting range is 350~400 nm). A separate 1X mask for contact aligner (Karl Suss MA6 wafer aligner) is thus made and the resulted SU-8 wafer. The fabrication steps of 4" PDMS device is shown in Figure 7.8. After aligning and bonding the PDMS device onto the nanoplasmonic wafer, the final integration system is shown in Figure 7.9. Each microfluidic single cell culture device is well fabricated. The integration system can be a potential tool for improvement in efficiency of new drug and therapeutic method evaluation.

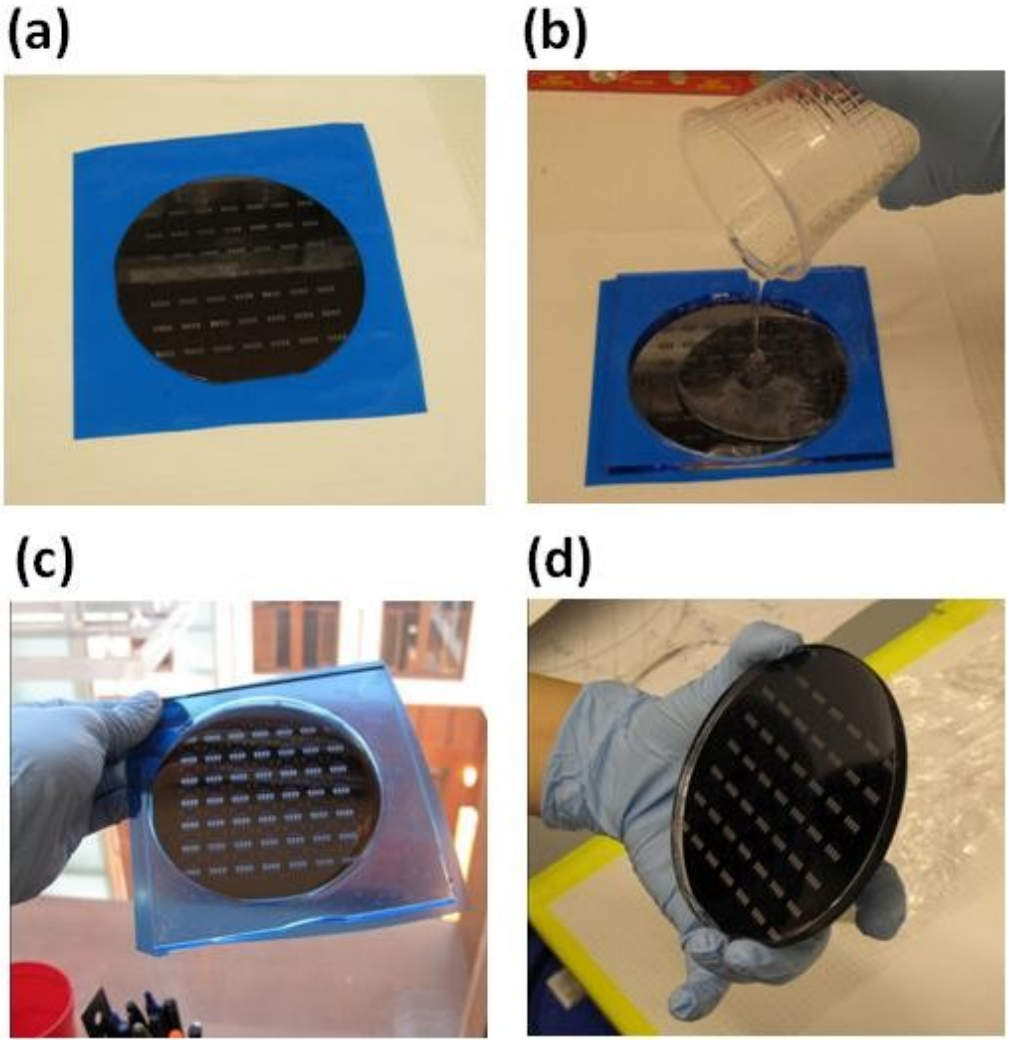

Figure 7.8 Fabrication of wafer-sized PDMS device[13]: (a) The SU8 patterned 4" silicon wafer is first attached to the wafer-dicing blue tape (b) a homemade acrylic plate with 4" hole is aligned to the 4" SU8 patterned silicon and fixed by the blue tape at the bottom and a PDMS mixture is then poured onto the Si wafer. (c) After curing PDMS, a 4" microfluidic with clean edge is then finished. (d) Carefully peel of the blue tape and the acrylic plate, the 4" PDMS device can be easily peeled off from the Si wafer for further processing steps.

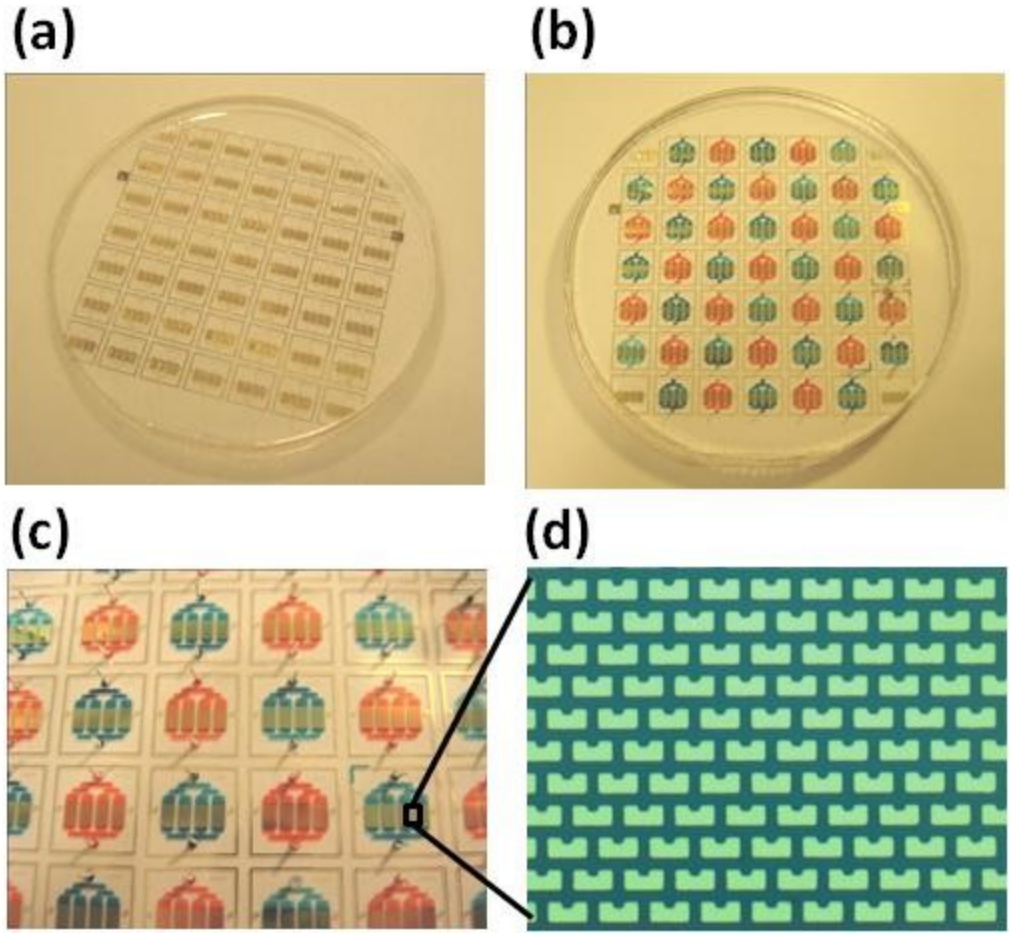

Figure 7.9 Wafer-scale integration of nanoplasmonic sensor array with microfluidic platform for single cell analysis. (a) The PDMS device is aligned and bonded to the nanoplasmonic patterned substrate. (b) Food dye injection to the microfluidic channel to clearly present the single cell culture system (c)(d) zoom in figures for single devices and the single cell traps.

References:

(1) Mattson, M. P. *Nature* **2004**, 430, 631-638
(2) Skovronsky, D. M.; Moore, D. B.; Milla, M. E.; Doms, R. W.; Lee. V. M. *The journal of biological chemistry* **2000**, 275, 2568-2575
(3) Olivieri, G.; Brack, Ch.; Muller-Spahn, F.; Stahelin, H. B.; Herrmann, M.; Renard, P.; Brockhaus, M.; Hock, C. J. *Neurochem*., **2000**, 74, 231-236
(4) Haugabook, S.J.; Yager, D.M.; Eckman, E.A.; Golde, T.E.; Younkin, S.G.; Eckman, C.B. *J. Neurosci. Methods*, **2001**, 108, 171-179.
(5) Albrecht, H.; Zbinden, P.; Rizzi, A.; Villetti, G.; Riccardi, B.; Puccini, P.; Catinella, S.; Imbimbo, B. P. *Combinatorial Chemistry & High Throughput Screening*, **2004**, 7, 745-756

(6) Clarke, E. E.; Shearman, M. S. *Journal of Neuroscience Methods*, **2000**, 102, 61-68
(7) Lyon, A.; Musick, M. D.; Natan, M. J. *Anal. Chem*.**1998**, 70,5177-5183
(8) Chumanov, G. D.; Efremov, R. G.; Nabiev, I. R. *Journal of Raman spectroscopy*, **1990**, 21, 4-8
(9) Hsu, C. M.; Connor, S. T.; Tang M. X.; Cui, Y. *Appl. Phys. Lett*. **2008**, 93, 133109-1-3
(10) Jiang, P.; Prasad, T.; McFarland, M. J.; Colvin V. L. *Appl. Phys. Lett*. **2006**,89, 011908-1-3
(11) Jiang, P.; McFarland, M. J. *J. Am. Chem. Soc*., **2005**, 127 (11), pp 3710–3711
(12) Jiang, P.; McFarland, M. J.; *J. Am. Chem. Soc.* **2004**, 126, 13778-13786
(13) Li, G.; Chen, Q.; Zhao, J. *Lab Chip- chips and tips* **2009**

CHAPTER 8:
FUTURE WORK AND CONCLUSIONS

8.1 Future work: enhance the sensitivity of nanoplasmonic probes

8.1.1 Enhance the sensitivity of crescent-shaped nanohole substrates

By fine tuning the LSPR peak position to match the molecular detection system, the higher sensitivity of sensing based on either LSPR peak shift or SERS is expected. For crescent-shaped nanohole substrates, by changing two key geometric parameters, size and thickness, the LSPR peaks can be easily tuned to match the detection system. Another potential method of manipulating the detection sensitivity of the crescent-shaped nanohole substrate is by using the positive nanocrescent tip-to-tip self-assembled with the crescent-shaped nanohole due to the nature of the fabrication process. This approach will be finished in the near future for further enhancement of the sensitivity of crescent-shaped nanohle array substrates.

In the SEM image of Figure 8.1(a), it is clearly seen that the positive nanocrescent top-to-tip aligned with crescent-shaped nanoholes. The positive nanocrescent is formed at the 2^{nd} gold deposition when the gold flux enters the region below the nanoshpere and deposits onto the nanodisk under the nanosphere. In this scheme, since the nanocrescent is connected to the continuous of the gold film, no LSPR resonance signal from the nanocrescent structure is expected. However, by adding a thin insulator layer such as SiO_2 before second Au deposition (Figure 8.1 (c)), a SiO_2 spacer thus forms between the nanodisk and positive nanocrescent and the LSPR resonance at the tip of the independent nanocrescent is expected.

More importantly, the coupling field at the tip region of both positive and negative nanocrescent could generate the enhancement of the signal in detection. The optical absorption spectra of the substrate with and without the SiO_2 spacer layer is shown in Figure 8.1(b) and a huge difference between the LSPR spectra is observed. The two substrates have exactly the same gold film thickness and are made by the same size nanosphere template. The sample with no SiO_2 layer has one LSPR around 910 nm, while the one with a 10 nm SiO_2 layer shows two peaks around 840 nm and 980 nm. The physics behind the optical properties after adding a thin insulator needs to be further investigated. How the thickness of this insulator layer affects the LSPR peak positions and the strength of enhanced electric field at the tip coupling region is another topic to be discussed.

Further tuning of the tip-to-tip self-assembled crescent-shaped nanohole substrates to match the peak position to the detection system is expected to enhance the sensing performance from the crescent-shaped nanohole substrates.

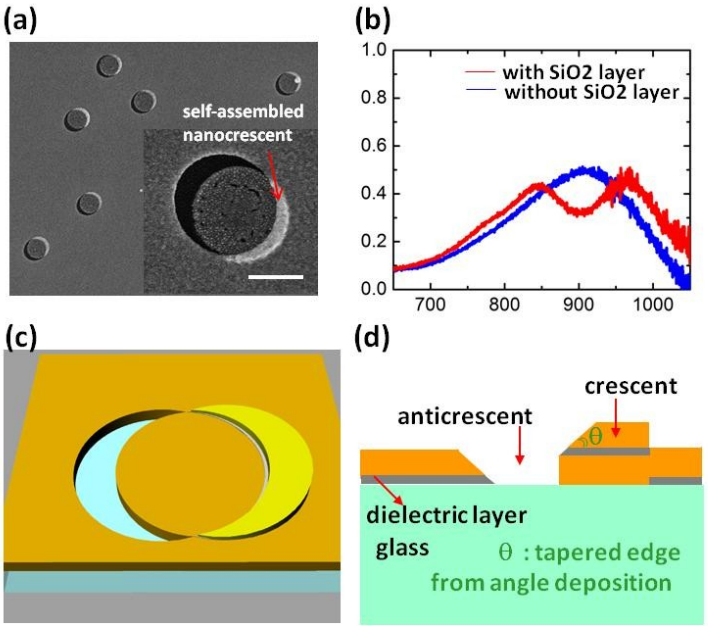

Figure 8.1 Enhance the sensitivity of the crescent-shaped hole by using the positive nanocrescent self-aligned to the crescent-shaped nanoholes. (a) A positive nanocrescent is clearly seen in the SEM image. (b) The adsorption spectra change abruptly after deposition of a 5 nm SiO_2 layer before the 2nd gold deposition. (c)-(d) An illustration of making nanocrescents insulated from the gold film by adding a thin dielectric film.

8.1.2 Enhance the sensitivity of nanocoral substrates

The work regarding nanocoral substrates presented in this dissertation is a new approach for creating stand-alone multifunctional nanosensors. Further tuning of the geometric parameters such as PS template size, etching time and gold thickness can help increase both ttthe contribution from the nanogap and LSPR field enhancement. I leave this part for future work and will continue to improve the performance of the nanocoral biosensor.

8.1.3 Other potential substrates for biomolecular sensing

During the research process to find potential nanoplasmonic structures for biomolecular sensing, several other substrates have been developed based on similar nanosphere templates and shadowing effects of etching or thin-film deposition. The substrates are listed here and I will leave the optimization and application of these substrates as future work.

In Figure 8.2 (a), the 3D double crescent array is the extension of the 3D nanocresent previously developed in our lab. Starting with the arrayed polystyrene nanospheres on the glass substrates, followed by oxygen plasma etching at low power, the nanospheres maintain their surface smoothness and spherical shape while the size shrinks. After gold coating, the 3D nanocrescent array is printed onto a transparent substrate such as PDMS membrane or clear tape with the PS side on top. The second oxygen plasma treatment can tailor the size of the PS core and the 3D double nanocrescent is formed after another gold layer deposition. The rim-to-rim intra-particle hot spots are expected to have high sensitivity for molecular detection.

One technological difficulty in fabricating the substrates is the printing step. When a soft material such as PDMS or tape is adhered to the nanocrescent array, a part of the nanocresent is buried into the matrix. This is a factor that can't be well controlled yet. Using MPTMS functionalized glass slides was attempted but the printing result was poor due to the lack of conformal contact between two glass substrates. Further improvement of the fabrication is left as future work.

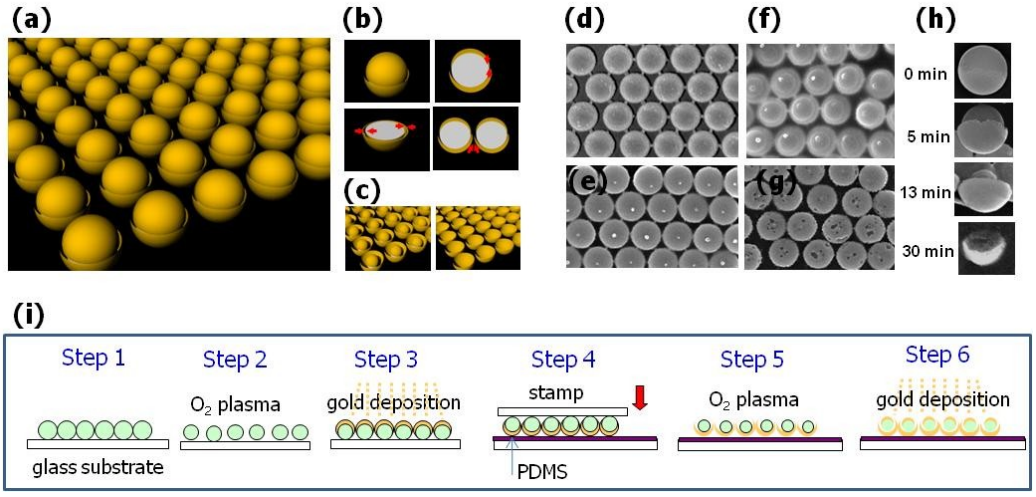

Figure 8.2 Three-dimensional double nanocrescent array. (a) A schematic diagram of the double nanocrescent array. (b) Different plasmonic coupling modes in the nanocrescent array. (c) The inner shell radius, r, can be tailored by different polystyrene core etching time. (d)-(h) SEM images of substrate fabrication after different steps: (d) gold coating on polystyrene beads array on a glass substrate (e) printing the gold coated beads onto PDMS membrane (f) before etching the inner core (g) 5 mins etching of the core by oxygen plasma (scale bar = 500nm) (h) 13 mins etching of the core by oxygen plasma (i) fabrication process

Another novel substrate developed is the football-shaped nanohole array as shown in Figure 8.3(a). The substrate is made by using the shadow effect during two separate angled directional gold depositions with nanosphere templates. The angle decided the aspect ratio of the football. The tips at the end of each football-shaped nanohole are expected hot-spots for biomolecular detection. The 2D double nanocrescent array shown in Figure 8.3(b) is made by adding one step to the fabrication process of the football-shaped nanohole array. An ion-milling step is added after two angled gold depositions and before the removal of polystyrene template. The fabrication process of these two substrates was listed in Figure 8.3(c). Better optical characterization and design for sensing application are again left for future work.

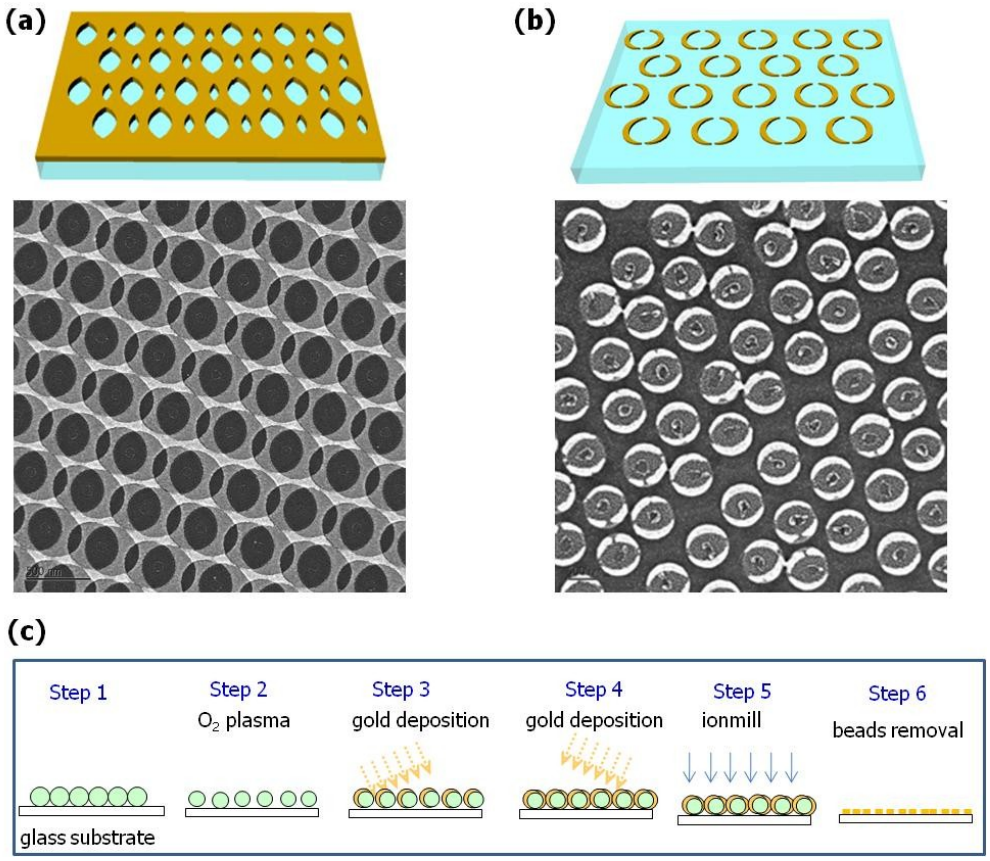

Figure 8.3 Football-shaped nanohole array and 2D double nanocrescent substrate fabricated by modified angled deposition and etching processes. (a) Football shaped nanohole substrates (b) 2D double nanocrescent array substrates. (c) The fabrication process of 2D double nanocrescent. The football-shaped nanoholes were made by PS template removal after Step 5 in the illustration.

8.2 Future work: wafer-scale crescent-shaped nanohole and nanocoral substrates

To get to the point of real application of drug assay or diagnosis, large area patterning of the uniformly arrayed nanoplasmonic probes is an important goal that needs to be realized. For the random PS nanosphere array template, wafer scale fabrication has already been demonstrated in this work. To get a 2D crystal of the hexagonal arrayed nanosphere pattern on the whole wafer scale, engineering efforts needed to be invested. There are wafer scale 2D nanosphere arrays assembled on Si wafers reported by using the Lagmuir-Blodgetting Method and a modified spin coating technology by suspending the silica nanospheres in the photocuring monomers. I believe these technological efforts will bring "nanosphere lithography" to the product level in the near future.

Wafer-scale nanoplasmonic probes with micro-scale pitch patterned by photolithography were demonstrated in Chapter 7.3. The photoresist pillar array with 0.8-1.4 μm diameter and 1.6-2.8 μm pitch can also be used as the template for fabricating the two nanoplasmonic substrates presented in this thesis: crescent-shaped nanoholes and nanocorals in Chapters 3 & 4, respectively. The smaller nanostructures can be made by tailoring the photoresist pillar templates with oxygen plasma. Further decreasing the dimensions of the nanostructures and optical characterization of the wafer-scale crescent-shaped nanohole arrays and nanocoral arrays are left as future work.

When using photoresist pillars as the mask for angled gold deposition, a uniform crescent-shaped nanoholes array covering an entire 4" wafer can be made(see Figure 8.4).

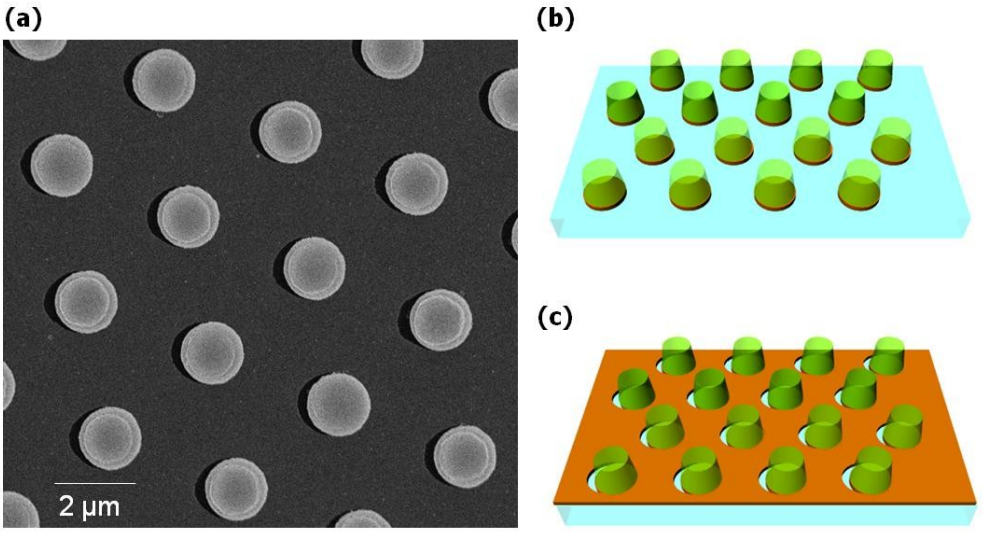

Figure 8.4 Wafer-scale crescent-shaped nanohole substrate made by a photoresist pillar array. (a) SEM images of crescent-shaped nanohole array before removal of the photoresist template. (b) An illustration of the process after vertical ion milling of the photoresist patterned gold coated glass substrate. (c) The crescent-shaped nanoholes were formed after angled gold deposition on substrate shown in (b).

As reported in Chapter 7.3, the heat generated during the ion milling process causes the reflow of the photoresist pillars and reshapes them into hemispheres. Interestingly, after reactive ion etching (95% CHF_3 + 5% O_2), we found the roughened surface on the photoresist hemisphere is similar to that of the nanocorals. After coated with a thin gold layer, the substrates are ready for SERS measurements. The SEM images of the wafer-scale nanocoral array made by a reflowed photoresist hemisphere template are shown in Figure 8.5. Further optimization of the geometric parameters of photoresist nanocorals and the characterization optical properties and sensing capabilities are left as future work.

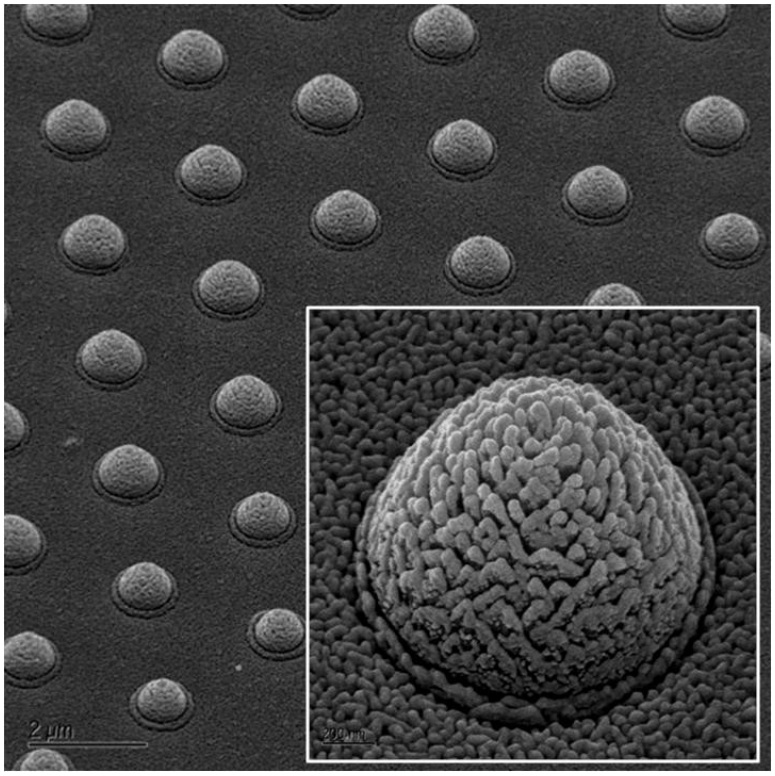

Figure 8.5 Wafer-scale nanocoral substrate made by a photoresist pillar array. The heat generated during the ion milling process causes reflow of the photoresist pillars and reshapes them into hemispheres. The following reactive ion etching resulted in the roughened surface for SERS application.

8.3 Conclusions

In this dissertation, the key components of integrated real-time label-free nanoplasmonic detection with high-throughput microfluidic cell culture platform were developed. Several novel nanoplasmonic geometries that provide sensitive, robust and low-cost solutions were proposed. Robust cell culture platforms that facilitate monitoring arrayed cells with precise micro-environmental control were reported. Beyond traditional cell monitoring, this analytical tool readily lends itself to integration with nanoplasmonic substrates. Such integrated platforms provide high-resolution dynamic information on large array of precisely controlled cell populations. To meet the goal of future real product application, wafer-scale integration of the nanoplasmonic and microfluidic platforms was also demonstrated.

As reported in Chapter 3, crescent-shaped nanoholes have sub-10 nm tips, are sharper than the positive nanocrescents and their LSPR peaks have a wide tunable range over visible and near IR ranges. The LSPR peak shift is characterized to be 300 nm/RIU and limit of detection of R6G molecules is found to be 10 nM.

I have also demonstrated that nanocorals can function as simple and cost-effective SERS nanoprobes. The highly roughened gold region of the nanocoral can adsorb more R6G than a flat gold surface, and has a SERS limit of detection of 10 nM R6G with high reproducibility. Moreover, after release from the substrate and functionalization of the PS region with antibodies, nanocorals attach specifically to breast cancer cells.

Three microfluidic platforms for long-term culture of arrayed cells were developed. By using the hydrodynamic cell trapping technology developed earlier in our group, I demonstrated the single cell array and tumor spheroid (composed of ~10 cells each) array. The physiologically-similar perfusion system continuously provides the cells with fresh media and removes metabolism waste products. Drug can be dosed in in-vivo-like to obtain a temporal profile, and a large amount of data can be acquired by recording the response of arrayed single cells or tumor spheroids. By assembling these cell culture array systems with the nanoplasmonic probes, we hope to provide a potential tool for future cell-based drug analysis.

The integration of the nanoplasmonic and microfluidic cell culture platform is demonstrated by a real-time Amyloid beta secretion system. APP transfected CHO cells were successfully cultured in a cell culture chamber with a 200-cell capacity, which was aligned and bonded on top of the nanoplasmonic substrates. The crescent-shaped nanoholes can detect the Aβ solution down to 1 nM and the real-time detection of the Aβ from the CHO cells culture upstream is left as future work. To extend the integration platform to the wafer-scale, we patterned the 4” glass wafer with a gold nanodisk array and bonded the 4” wafer-sized PDMS single cell culture array device. This was an attempt to extend the integration platform to a mass-producible scheme.